

# Scattering-Theory-Based Methodology for Electromagnetic Transient Analysis of Nonuniform Frequency-Dependent Transmission Line Structures

by

Manuja Shamith Gunawardana Sooriyaarachchige Don

A thesis submitted to the Faculty of Graduate Studies of  
The University of Manitoba  
in partial fulfilment of the requirements of the degree of

Doctor of Philosophy

Department of Electrical and Computer Engineering  
University of Manitoba  
Winnipeg, Canada

Copyright © 2022 Manuja Shamith Gunawardana Sooriyaarachchige Don

# Examining Committee

This thesis was examined and approved by the following examining committee on July 7, 2022:

- **Prof. Behzad Kordi** (advisor)  
Department of Electrical & Computer Engineering  
University of Manitoba
- **Prof. Athula Rajapakshe**  
Department of Electrical & Computer Engineering  
University of Manitoba
- **Dr. Dharshana Muthumuni**  
Department of Electrical & Computer Engineering  
University of Manitoba
- **Prof. Keyhan Sheshyekani**  
Department of Electrical Engineering  
Polytechnique Montreal

The Ph.D. oral examination was chaired by:

- **Prof. Qiang Zhang**  
Department of Biosystems Engineering  
University of Manitoba

# Abstract

Overhead transmission lines are a vital component in electrical power networks. Overvoltage transients that originate in transmission lines due to disturbances such as lightning or switching can reach other components in a power system and create electrical insulation breakdown and equipment failure if countermeasures are not sufficiently taken. Therefore, accurate electromagnetic transient (EMT) modelling of the transmission line network is an essential requirement in designing and analyzing a power system.

The increasing demand for electrical power and limited availability of land has caused overhead power transmission lines to be constructed in close proximity to each other. These close encounters such as nonparallel lines in close proximity, ultra-high voltage (UHV) lines crossing above lower voltage lines, communication lines or buried pipelines, and discontinuities such as lines undergoing sharp bends are generally nonuniform in nature. Several researchers have shown that the transient behaviour of transmission lines with such nonuniformities is far from what is predicted using conventional transmission line models that assume a uniform cross-sectional structure. Although three dimensional full-wave techniques can be used to accurately analyze these non-uniform structures, they are often associated with high computational costs and typically require iterative methods to obtain solutions. This makes them hardly suitable for circuit-type time-domain simulations.

---

This research is focused on developing computationally efficient and EMT-simulator compatible time-domain models to analyze the transient behavior of nonuniform transmission problems involving nonparallel conductors. Transient models for both overhead and buried nonuniform structures have been derived and successfully implemented on an EMT simulator (PSCAD/EMTDC). Higher computational efficiency has been achieved by developing closed-form mathematical models which can be solved using lesser number of computations than full-wave models as well as by using parallel computing techniques. Results have been compared with those obtained using full-wave solvers and field measurement obtained by other researchers available in the literature.

# Acknowledgements

First and foremost, I would like to express my appreciation to my advisor, Dr. Behzad Kordi, for his great support and supervision during this research. I deeply appreciate all his valuable comments and guidance.

Many thanks to my thesis committee, Dr. Athula Rajapakse and Dr. Dharshana Muthumuni for their valuable comments and suggestions to enhance this thesis.

Financial support from University of Manitoba, Faculty of Graduate Studies and Natural Sciences and Engineering Research Council of Canada (NSERC) is gratefully acknowledged. I would also like to express my gratitude to the Government of Manitoba for the financial support received in the form of Graduate Scholarship.

Last but not least, I would like to thank my family and friends. Sincere thanks to my family for their kindness and support while I was pursuing my studies away from them. Many thanks to my friends in Winnipeg, who have been immensely supportive through my ups and downs.

# Dedications

*To my loving family.*

# Table of Contents

Examining Committee . . . . .	ii
Abstract . . . . .	iii
Acknowledgements . . . . .	v
Dedications . . . . .	vi
List of Figures . . . . .	xi
List of Tables . . . . .	xvii
Nomenclature . . . . .	xviii
<b>1 Introduction</b>	<b>1</b>
1.1 Background and Motivation . . . . .	1
1.2 Problem Definition and Conventional Solutions . . . . .	2
1.3 Research Objectives and Contributions . . . . .	3
1.3.1 Objectives . . . . .	3
1.3.2 Contributions . . . . .	4
1.4 List of Publications . . . . .	6
1.5 Thesis Outline . . . . .	8
<b>2 Literature Review</b>	<b>10</b>

---

2.1	Modelling Non-Uniform Transmission Line Structures . . . . .	12
2.2	Inclusion of Frequency-Dependent Losses . . . . .	18
2.2.1	Overhead wires above lossy ground . . . . .	19
2.2.2	Buried wires in lossy ground . . . . .	21
2.3	Time-Domain Implementation of Non-Uniform Transmission Lines . . . . .	25
2.4	External Field Coupling to Non-Uniform Transmission Lines . . . . .	29
2.5	Parallel Implementation of FDTD Algorithms . . . . .	36
<b>3</b>	<b>Time-Domain Modelling of Nonuniform Overhead Lines</b>	<b>40</b>
3.1	Dispersive Scattered Field Transmission Line Model . . . . .	41
3.2	Time-Domain Implementation . . . . .	48
3.3	Implementation of DSFTL on PSCAD/EMTDC . . . . .	49
3.4	Results and Discussion . . . . .	51
3.4.1	Verification of the DSFTL model using a full-wave solver . . . . .	51
3.4.2	Verification of the DSFTL model using power frequency measurements	52
3.4.3	Case study on the effect of faults on nearby lines . . . . .	56
3.4.4	DSFTL for modelling bent conductors . . . . .	60
3.5	Summary . . . . .	63
<b>4</b>	<b>External Field Coupling to Nonuniform Overhead Lines</b>	<b>65</b>
4.1	Inclusion of External Fields Over PEC Ground . . . . .	66
4.2	Inclusion of External Fields Over Lossy Ground . . . . .	69
4.3	Results and Discussion . . . . .	72
4.3.1	Comparison with full-wave results . . . . .	74
4.3.2	Comparison of results in the presence of frequency-dependent ground	74

---

---

4.3.3	Lightning near crossing conductors above perfectly conducting ground	76
4.3.4	Lightning near crossing conductors above finitely-conducting ground .	81
4.4	Summary . . . . .	86
<b>5</b>	<b>Nonparallel Overhead and Buried Conductors</b>	<b>88</b>
5.1	DSFTL Model for Overhead and Buried Conductors . . . . .	89
5.2	Time-Domain Implementation . . . . .	96
5.3	Results and Discussion . . . . .	100
5.3.1	Effect of the crossing angle . . . . .	106
5.3.2	Effect of the ground conductivity . . . . .	106
5.3.3	Effect of the radius of the buried conductor . . . . .	109
5.3.4	Effect of the burial depth . . . . .	110
5.3.5	Case study of lightning induced voltages . . . . .	111
5.4	Summary . . . . .	112
<b>6</b>	<b>Parallel Finite-Difference Time-Domain Method</b>	<b>114</b>
6.1	Parallel MFDTD Using multicore CPU . . . . .	114
6.2	Parallel MFDTD Using GPU . . . . .	116
6.3	Results and Discussion . . . . .	118
6.3.1	Performance of the parallel CPU algorithm . . . . .	118
6.3.2	Performance of the parellel GPU algorithm . . . . .	119
6.4	Summary . . . . .	124
<b>7</b>	<b>Conclusions and Future Work</b>	<b>125</b>
7.1	Conclusions . . . . .	125
7.2	Future Work . . . . .	127

References	130
------------	-----

# List of Figures

1.1	A graphical illustration of the contributions of this thesis. . . . .	5
2.1	Bergeron's model for a lossy single-conductor transmission line. . . . .	11
2.2	Illustration of the space variable ( $R$ ) in the Green's function under thin-wire approximation. . . . .	14
2.3	Illustration of complex image theory: (a) Overhead lines above lossy ground. (b) Lossy ground replaced with a PEC ground at a complex depth. (c) PEC ground replaced with image conductors. . . . .	21
2.4	Illustration of the calculation of voltage and current of space segment $k$ at time-step $n$ in the MFDTD algorithm. . . . .	27
2.5	Radiated electromagnetic fields by an infinitesimal current element of a monopole antenna. . . . .	30
2.6	Equivalent circuit of the Taylor model [75] for external field coupling. . . . .	33
2.7	Equivalent circuit of the Agrawal model [76] for external field coupling. . . . .	34
2.8	Equivalent circuit of the Rachidi model [77] for external field coupling. . . . .	35
2.9	Illustration of speedup limit according to Amdhal's law as a function of number of parallel processors ( $p$ ) for different values of parallel portions ( $f$ ). . . . .	39

---

3.1	Single-conductor transmission lines crossing each other above (a) finitely-conducting ground and (b) complex image representation of conductors above ground. . . . .	42
3.2	(a) Magnitude and (b) phase of $g(z_i, z'_i)$ vs frequency. . . . .	44
3.3	Illustration of the implementation of DSFTL model on PSCAD/EMTDC. . .	50
3.4	Derivative of a Gaussian waveform applied on conductor $i$ . . . . .	52
3.5	Current generated at the sending end in the excited conductor. . . . .	53
3.6	Sending end current on the victim conductor for crossing angles of (a) $30^\circ$ (b) $60^\circ$ and (c) $90^\circ$ . . . . .	54
3.7	Conductor arrangements of (a) 1000 kV UHVAC line and (b) 110 kV HVAC line [12]. . . . .	56
3.8	Voltage waveforms at the crossing points of (a) energized 1000 kV line (b) 110 kV line with ungrounded ends and (c) 110 kV line with grounded ends obtained using DSFTL model on PSCAD/EMTDC. . . . .	57
3.9	Schematic of double circuit 1000 kV and 110 kV transmission lines along with locations where faults were applied. . . . .	58
3.10	Voltage waveforms at the point of crossing on (a) energized 1000 kV line having a 3-phase fault and (b) energized 110 kV line obtained using DSFTL model on PSCAD/EMTDC. . . . .	59
3.11	Voltage waveforms at the crossing point of the grounded 110 kV line when the 1000 kV line undergoes a (a) L-G fault at load end (location ①) cleared by breaker B2, (b) L-G fault at location ② cleared by breaker B1, and (c) L-L-L fault at load end cleared by breaker B2 obtained using DSFTL model incorporated in PSCAD/EMTDC. . . . .	61

---

---

3.12	A transmission line bend near Riel converter station, Winnipeg, Manitoba, Canada. . . . .	62
3.13	Sending end voltages (normalized to the excited conductor) of the (a) excited conductor and (b) and (c) victim conductors for an excitation of a standard 1.2/50 $\mu$ s lightning impulse chopped after 5 $\mu$ s with a chopping time of 0.1 $\mu$ s obtained using SFTL model and classical MTL theory. . . . .	64
4.1	A schematic of a lightning return stroke channel nearby two transmission lines crossing at an angle of $\alpha$ . . . . .	66
4.2	A schematic a lightning strike in the vicinity of two crossed transmission lines.	73
4.3	20 kA 1.2/50 $\mu$ s base current of the lightning channel generated using Heidler formulation for the first stroke. . . . .	73
4.4	Terminal current at the far end of the crossing on the carrier line when terminations of each line are matched to its corresponding characteristic impedance.	74
4.5	Terminal current at the far end of the crossing on the victim line for crossing angles of (b) 30°, (c) 60°, and (d) 90°, when terminations of each line are matched to its corresponding characteristic impedance. . . . .	75
4.6	Voltage induced at a terminal of a 1 km long line due to a lightning strike at a lateral distance of 50 m from its midpoint obtained using the proposed DSFTL model compared with results found in [78]. . . . .	76
4.7	Voltage at the point of crossing on the carrier line when terminations of each line are matched to its corresponding characteristic impedance. . . . .	77
4.8	Voltage at the point of crossing on the victim line for crossing angles of (a) 30°, (b) 60°, and (c) 90°, when terminations of each line are matched to its corresponding characteristic impedance. . . . .	78

---

---

4.9	Voltage at the point of crossing on the carrier line when the carrier line has matched ends and the victim line is grounded. . . . .	79
4.10	Voltage at the point of crossing on the victim line for crossing angles of (a) 30°, (b) 60°, and (c) 90°, when the carrier line has matched ends and the victim line is grounded. . . . .	80
4.11	Voltage at the point of crossing on the carrier line when both lines are grounded.	81
4.12	Voltage at the point of crossing on the victim line for crossing angles of (b) 30°, (c) 60°, and (d) 90°, when both lines are grounded. . . . .	82
4.13	Terminal current at the far end of the crossing on the victim line for a crossing angles of 60° and ground conductivity of (a) 0.1 S/m, (b) 0.01 S/m and (c) 0.001 S/m when terminations of each line are matched to its corresponding characteristic impedance. . . . .	83
4.14	Voltage at the point of crossing on the carrier line when terminations of each line are matched to their corresponding characteristic impedance. . . . .	84
4.15	Voltage at the point of crossing on the victim line for crossing angles of (a) 30°, (b) 90°, and (c) 150°, when terminations of each line are matched to their corresponding characteristic impedance. . . . .	85
4.16	Voltage at the point of crossing on the carrier line when terminals of both line are grounded . . . . .	86
4.17	Voltage at the point of crossing on the victim line for crossing angles of (a) 30°, (b) 90°, and (c) 150°, when terminals of both line are grounded . . . . .	87
5.1	Single-conductor over head transmission line crossing above a bare conductor buried in finitely-conducting ground. . . . .	89

---

---

5.2	Illustration of the space-time discretization and the update procedure of voltage and current vectors of space segment $k$ at time-step $n$ in the MFDTD algorithm. . . . .	98
5.3	Derivative of a Gaussian waveform applied on the overhead conductor. . . .	101
5.4	Elements of PUL (a) impedance and (b) admittance matrices of the wire structure. . . . .	102
5.5	Sending end currents of (a) the overhead conductor and (b) the buried conductor obtained using MFDTD method and a thin-wire full-wave solver. . . .	103
5.6	A wire model of the geometry implemented in the fullwave solver (NEC4) used to validate the proposed DSFTL model. The buried conductor is modeled as 8 straight, parallel wires that allow simulating a conductor with an arbitrary diameter. . . . .	105
5.7	Current at the point of crossing in the overhead wire. . . . .	105
5.8	Current at (a) $z = \frac{dz}{2}$ , (b) $z = c$ and (c) $z = \ell - \frac{dz}{2}$ in the buried conductor. . . .	107
5.9	Current at the point of crossing in the buried conductor for crossing angles of (a) $60^\circ$ (b) $90^\circ$ . . . . .	108
5.10	Current at the point of crossing in the buried conductor for ground conductivity values of (a) 0.01 S/m and (b) 0.0001 S/m. . . . .	109
5.11	Current at the point of crossing in the buried conductor for conductor radii of (a) 0.5 m and (b) 0.99 m. . . . .	110
5.12	Current at the point of crossing in the buried conductor for burial depths of (a) 5 m and (b) 10 m. . . . .	111

---

---

5.13	Voltage at the crossing in the overhead line and buried conductor when the overhead line is excited with (a) a standard $1.2/50 \mu\text{s}$ lightning impulse and (b) a standard $1.2/50 \mu\text{s}$ lightning impulse chopped after $5 \mu\text{s}$ with a chopping time of $0.5 \mu\text{s}$ . . . . .	113
6.1	Proposed parallel algorithm for MFDTD using multicore CPU architecture. . . . .	116
6.2	Proposed parallel algorithm for MFDTD using GPU architecture. . . . .	117
6.3	Sending end currents of (a) the overhead conductor and (b) the buried conductor obtained by distributing the computations among different number of processors. . . . .	120
6.4	Speed up factor obtained using algorithm Vs. the number of processors in CPU for varying number of time-steps. . . . .	121
6.5	Sending end currents of the overhead wire obtained using a serial program and the proposed parallel algorithm for simulations of (a) 138 space-steps and 1001 time-steps and (b) 255 space-steps and 10001 time-steps. . . . .	122
6.6	Speed up factor obtained using the GPU algorithm Vs. the number of Space-segments for varying number of time-steps. . . . .	123

# List of Tables

3.1	Measurement data from [12] and simulated results using DSFTL model of induced voltages (peak) on the ungrounded LV line when the HV line is energized with a 50 Hz voltage of 816.5 kV (peak). . . . .	55
3.2	Measurement data from [12] and simulated results using DSFTL model of induced voltages (peak) on the grounded LV line when the HV line is energized with a 50 Hz voltage of 816.5 kV (peak). . . . .	55
6.1	Execution time of the MFDTD algorithm using different number of processors.	119
6.2	Comparison of the execution time of the MFDTD algorithm using serial programming and GPU programming. . . . .	123

# Nomenclature

<b>CPU</b>	Central Processing Unit
<b>CR</b>	Cooray-Rubinstien
<b>CUDA</b>	Compute Unified Device Architecture
<b>DSFTL</b>	Dispersive Scattered Field Transmission Line
<b>EMT</b>	Electromagnetic Transient
<b>FDTD</b>	Finite Difference Time Domain
<b>FEM</b>	Finite Element Method
<b>FFT</b>	Fast Fourier Transform
<b>FWHM</b>	Full Width at Half Maximum
<b>GPU</b>	Graphical Processing Unit
<b>HED</b>	Horizontl Electric Dipole
<b>IFFT</b>	Inverse Fast Fourier Transform
<b>MFDTD</b>	Modified Finite Difference Time Domain
<b>MPI</b>	Message Passing Interface
<b>MTL</b>	Multiconductor Transmission Line
<b>MTLE</b>	Modified Transmission Line Exponential
<b>MTLL</b>	Modified Transmission Line Linear

<b>NEC</b>	Numerical Electromagnetic Code
<b>PEC</b>	Perfect Electric Conductor
<b>PUL</b>	Per Unit Length
<b>SFTL</b>	Scattered Field Transmission Line
<b>TEM</b>	Transverse Electromagnetic Mode
<b>UHV</b>	Ultra High Voltage

---

# Chapter 1

## Introduction

### 1.1 Background and Motivation

Overhead transmission lines serve as the primary method for transmitting electrical energy over large distances. Overvoltage transients may originate in transmission lines due to disturbances such as lightning or switching and reach other components in a power system [1–3]. Consequently, electrical insulation breakdown and equipment failure may occur if countermeasures are not sufficiently taken. Therefore, accurate electromagnetic transient (EMT) modelling of transmission lines is an essential requirement in designing and analysing power systems.

With the expansion of power networks and due to spacial constraints, transmission lines that come into close proximity of each other have become an inevitable occurrence. Furthermore, lines of higher operating voltages are added to power networks often sharing same transmission corridors with other lower voltage lines [4, 5]. This has resulted in non-uniformities such as non-parallel lines in close proximity, ultra high voltage (UHV)

lines crossing above lower voltage lines or communication lines, lines crossing above buried pipelines and lines undergoing sharp bends to be increasingly prevalent in transmission line networks [6–8]. During these close encounters over-voltage transients on one line have the possibility to create induced interference on other nearby lines [9–11]. Induced power frequency voltage on high voltage (HV) lines caused by UHV lines crossing above has also become a growing concern with regard to safety of maintenance workers [12–14]. In the case of pipelines, this arises the danger of electric shock while induced currents also may affect corrosion protection mechanisms in the pipeline [6, 15].

## 1.2 Problem Definition and Conventional Solutions

Conventional transmission line components in electromagnetic transient (EMT) simulators, which are used to analyze the transient behavior of power networks are based on multi-conductor transmission line (MTL) theory under the assumption of transverse electromagnetic (TEM) mode of propagation [16–18]. Frequency dependent ground losses are typically incorporated into these models using Carson-Pollaczek formula [19, 20]. However, these conditions are only applicable to infinitely long uniform transmission lines, which is typically not fulfilled in physical implementation [16]. Method of moments with surface impedance operator (MoM-SO) [21] based models have been incorporated into EMT simulators to simulate non-TEM mode wave propagation in transmission lines in [22, 23]. However, since MOM-SO is based on the circuit theory it cannot be used for finite-length or nonuniform conductors [24]. In addition, conventional terminal-based uniform transmission line models used in EMT simulators are not capable of modelling non-uniform soil parameters, line sag and proximity effects. Therefore, there is a need to incorporate the effects of non-uniformities of

finite length transmission lines in EMT simulators in-order to accurately model the transient behavior of current transmission networks [25, 26].

FDTD algorithms discretize the structure into a finite number of space segments and calculate the voltage and current of each space segment at each time-step field-to-line coupling [16, 27, 28]. Therefore, modelling transmission lines with non-uniform line parameters [29] and non-uniform external field excitation [27] is straightforward in FDTD algorithms. A disadvantage in FDTD models compared to conventional terminal based models used for uniform lines is that they require more computations per time-step. Therefore, a study on efficient parallel computing algorithms suitable for FDTD models will be beneficial for analysing non-uniform lines.

## 1.3 Research Objectives and Contributions

### 1.3.1 Objectives

Objectives of this research are

- To develop a method to simulate non-uniform fields acting upon multi-conductor power transmission line structures consisting of both overhead and buried conductors in an EMT simulator.
- To analyze the behaviour of non-uniform transmission line structures during fast power system transients such as switching and lightning with the presence of other power system components.
- To develop efficient parallel computing methods suitable for FDTD models which are used to solve nonuniform transmission line problems.

### 1.3.2 Contributions

- A novel analytical formula for the impedance of non-parallel and bent overhead conductors above frequency-dependent finitely-conducting ground.
- A novel analytical formula for the mutual impedance between non-parallel overhead and buried conductors in the presence of frequency-dependent finitely-conducting ground.
- A dispersive (frequency-dependent) non-uniform transmission line model, namely dispersive scattered field transmission line (DSFTL) model which is suitable for EMT-type simulators to model multi-conductor nonuniform transmission lines.
- Computationally efficient parallel algorithms for Modified FDTD (MFDTD) based transmission line models. Parallel implementations using both conventional central processing units (CPU) as well as graphical processing units (GPU) have been developed which would be equally beneficial for the analysis of non-uniform lines as well as uniform lines under non-uniform field-to-line coupling.

Contributions of this work are illustrated graphically in Fig. 1.1.

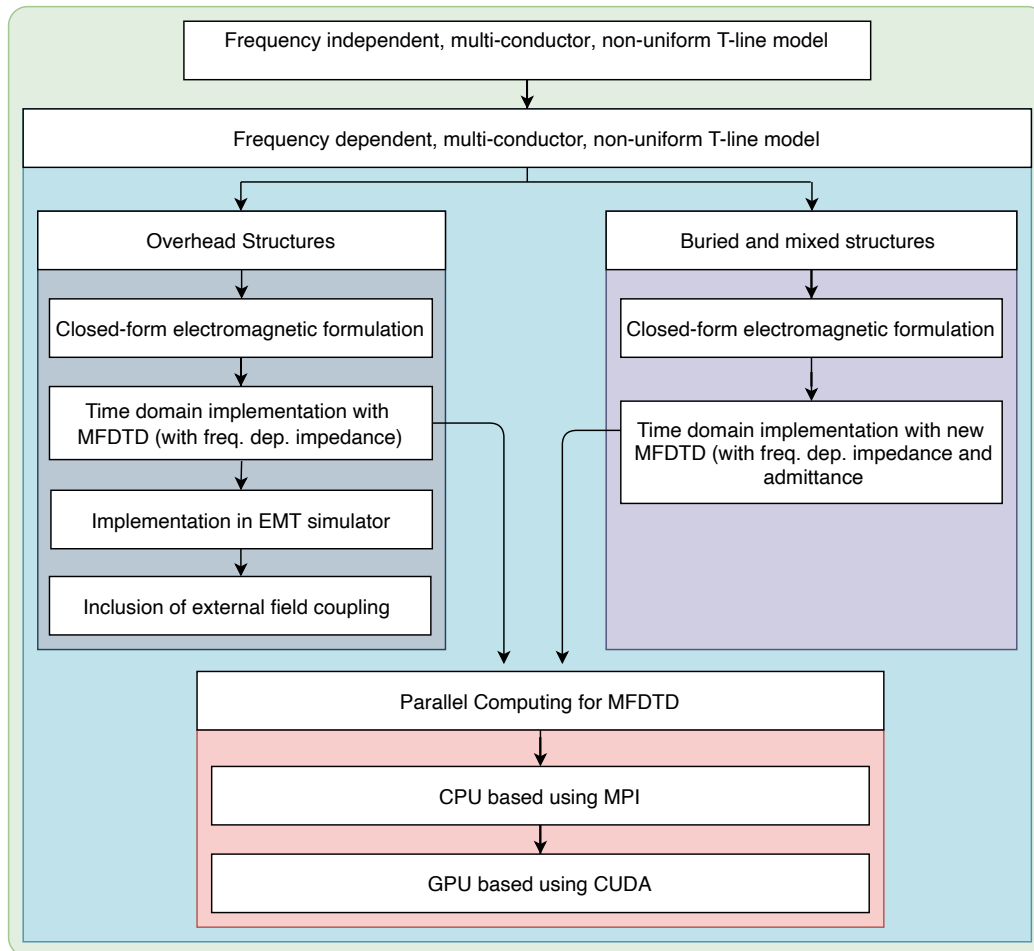


**Fig. 1.1:** A graphical illustration of the contributions of this thesis.

## 1.4 List of Publications

1. **M. Gunawardana** and B. Kordi, “Coupling Model for Time-Domain Analysis of Nonparallel Overhead Wires and Buried Conductors in the Presence of Lossy Ground,” under review in *Electric Power Systems Research*, 2022.

This paper proposed an EMT compatible time-domain model for nonparallel overhead and buried conductors in the presence of finitely-conducting frequency-dependent ground. Closed-form expressions were derived for the per unit length (PUL) impedance and admittance matrices based on thin-wire electromagnetic scattering theory.

2. **M. Gunawardana** S. Fu and B. Kordi, “Transient Response of Nonparallel Frequency-Dependent Transmission Lines Due to Nearby Lightning Strikes in the Presence of Finitely-Conducting Ground,” Special Issue devoted for ICLP-SIPDA 2021, *Electric Power Systems Research*, (Early Access) 2022.

In this article a nonuniform frequency-dependent transmission line model with external field coupling generated by a nearby lightning channel was used to analyze the effect of such a strike on the transient behaviour of two crossing conductors.

3. **M. Gunawardana** and B. Kordi, “GPU and CPU Based Parallel FDTD Methods for Frequency-Dependent Transmission Line Models,” *Letters on Electromagnetic Practice and Applications*, (Early access) 2022.

In this article, parallel algorithms to increase the computational efficiency of the FDTD-based models for frequency-dependent transmission lines are proposed and implemented using conventional multi-core CPU and GPU architectures.

4. **M. Gunawardana**, A. Ng and B. Kordi, “Time-Domain Coupling Model for Nonpar-

allel Frequency-Dependent Overhead Multiconductor Transmission Lines Above Lossy Ground,” IEEE Transactions on Power Delivery (Early Access), 2021.

In this paper, a dispersive, frequency-dependent, nonuniform multiconductor transmission line model based on electromagnetic scattering theory was proposed. A novel analytical formulation was proposed for PUL parameters of nonparallel overhead lines. The proposed model was also implemented of a electromagnetic transient simulator (PSCAD/EMTDC).

5. **M. Gunawardana** and B. Kordi, “Modelling Transient Response of Nonuniform Transmission Lines Due to Nearby Lightning Strikes,” 35th International Conference on Lightning Protection, Virtual Conference, 2021

In this paper a nonuniform lossless transmission line model with external field coupling generated by a nearby lightning channel was used to analyze the effect of such a strike on the transient behaviour of two crossing conductors.

- This paper was recognized with the “Young Scientist Award” at the 35th International Conference on Lightning Protection, 2021.

6. A. Ng, **M. Gunawardana** and B. Kordi, “Simulation of Transmission Line Bend Using a Non-Uniform Transmission Line Model Based on Scattering Theory,” IEEE Power & Energy Society General Meeting (PESGM), Virtual Conference, 2020

This paper proposed a time-domain model for multi-conductor transmission lines with a bend nonuniformity. A real world scenario of two 90° transmission line bends in close proximity to Riel converter station, Winnipeg, Manitoba, Canada was analysed under lightning transients.

## 1.5 Thesis Outline

This thesis is divided in to 7 chapters as defined below:

### **Chapter 1: Introduction**

This chapter includes background information, problem definition and existing solutions, motivation, objectives, and contributions.

### **Chapter 2: Literature Review**

This chapter provides an overview of classical uniform MTL models in the presence of finitely conducting ground and their limitations in modelling non-uniform field coupling, currently available methods in modelling non-uniform structures and their adaptability in EMT modelling.

### **Chapter 3: Time-Domain Modelling of Nonuniform Overhead Lines**

In this chapter a closed-form transmission line model, namely the DSFTL model, based on electromagnetic scattering theory is proposed for a lossy, frequency-dependent, nonuniform wire structure over finitely-conducting ground. Implementation of the proposed model in an EMT simulator is also discussed.

### **Chapter 4: External Field Coupling to Nonuniform Overhead Lines**

In this chapter the DSFTL model is modified to accommodate the external field coupling generated a by nearby lightning channel and used to analyze the effect of such a strike on the transient behaviour of two crossing conductors. A case study is also performed to investigate the transient behaviour of an overhead wire above lossy ground with and without the presence of a nearby nonparallel wire.

### **Chapter 5: Nonparallel Overhead and Buried Conductors**

This chapter extends the DSFTL model to include the field coupling between nonparallel overhead and buried conductors using existing coupling methods. A formulation for the

mutual coupling between overhead and buried conductors in the infinite integral format is first obtained using the Hertzian vector for the field coupling between two media. The resulting formulation is then simplified to a closed-form expression to facilitate efficient computation. A case study is also performed on induced voltages in buried conductors during direct lightning strikes to the overhead line.

**Chapter 6: Parallel Computing Methods for Finite-Difference Time-Domain**

This chapter proposes parallel algorithms to increase the computational efficiency of the DSFTL model based on multi-core CPU and GPU architectures. Accuracy and performance of each algorithm are analyzed and discussed.

**Chapter 7: Conclusions and Future Work**

This chapter provides the conclusion of the thesis drawn from the results and suggested extensions.

---

## Chapter 2

### Literature Review

Classical Telegrapher's equations used to model multi-conductor transmission lines are given in the frequency domain by [16]

$$\frac{\partial}{\partial z} \mathbf{V}(z, j\omega) + \mathbf{Z}(j\omega) \mathbf{I}(z, j\omega) = \mathbf{0} \quad (2.1a)$$

and

$$\frac{\partial}{\partial z} \mathbf{I}(z, j\omega) + \mathbf{Y}(j\omega) \mathbf{V}(z, j\omega) = \mathbf{0} \quad (2.1b)$$

where,  $\mathbf{V}$  and  $\mathbf{I}$  are the voltage and current vectors at any location  $z$  while  $\mathbf{Z}$  and  $\mathbf{Y}$  are the per-unit-length (PUL) impedance and admittance matrices. For frequency independent lossless lines (*i.e.* when  $\mathbf{Z} = j\omega\mathbf{L}$  and  $\mathbf{Y} = j\omega\mathbf{C}$  where  $\mathbf{L}$  and  $\mathbf{C}$  are PUL inductance and capacitance matrices) (2.1) has an analytical solution in the time-domain [16]. Based on this solution a circuit model, namely Bergeron's model has been developed which is commonly used in EMT simulators [17,18] to represent multi-conductor transmission lines. Bergeron's model for a single conductor transmission line is shown in Fig. 2.1 where,  $m$

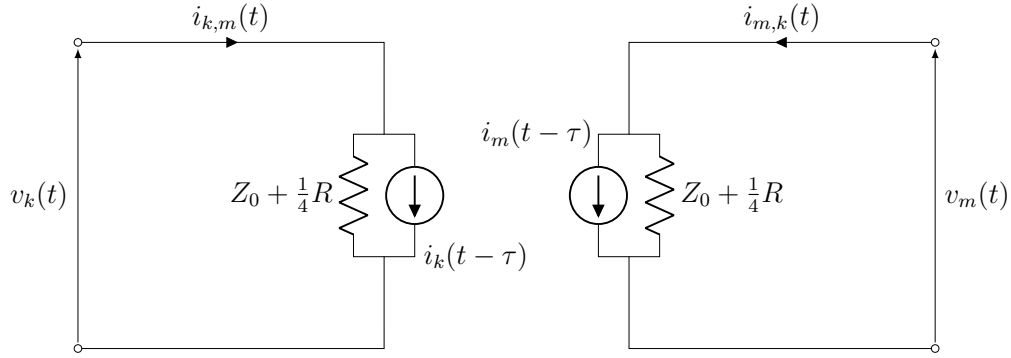


**Fig. 2.1:** Bergeron's model for a lossy single-conductor transmission line.

and  $k$  refer to the two ends, and  $Z_0 = \sqrt{L/C}$  to the characteristic impedance of the line. Also, conductor losses are generally added to these models using a lumped resistance  $R$ . In order to model multi-conductor transmission lines, the system of equations in (2.1) is first decoupled using similarity transformations [16] and individual circuit models for each decoupled mode is solved simultaneously to calculate mode voltages and currents. The mode voltages and currents are then converted back into phase voltages and currents. In order to model frequency-dependent transmission lines the ground return impedance is typically included using Carson's formula [19]. When the PUL parameters are frequency-dependent the multiplication between frequency-dependent terms in the frequency-domain convert into convolutions in the time-domain. This convolution can be performed efficiently using recursive calculations by fitting the propagation constant and the characteristic admittance parameters into a rational function [30–32]. Most EMT solvers use the universal line model (ULM) [30] for uniform transmission lines derived using this principle [17, 18].

In these models the terminal voltage and current at one end of the line at a particular time ( $t$ ) can be computed using the terminal voltage and current of the other end of the line and thus are referred to as two-port models [16]. It is evident that two port models are

derived on the basis that the structure in-between the two ends has uniform PUL parameters. Therefore they are incapable of simulating any of the nonuniform structures mentioned in Section 1 whose cross-section is not constant over their span.

## 2.1 Modelling Non-Uniform Transmission Line Structures

A transmission line approach can be developed for non-uniform structures in the frequency domain as [16]

$$\frac{d}{dz}\mathbf{V}(z, j\omega) + \mathbf{Z}(z, j\omega)\mathbf{I}(z, j\omega) = \mathbf{0} \quad (2.2a)$$

and

$$\frac{d}{dz}\mathbf{I}(z, j\omega) + \mathbf{Y}(z, j\omega)\mathbf{V}(z, j\omega) = \mathbf{0}. \quad (2.2b)$$

Solving nonconstant-coefficient ordinary differential equations as these is considered to be very difficult and a common way of handling such cases is to divide the structure into cascaded uniform sections [16]. Such models have been developed for non-parallel conductors in [33,34]. However, segmenting the inclined wire is known to change its length and affect its traveling time if not addressed as a forced delay [33]. Also, since these models are formulated assuming the currents are parallel at every cross section, they are valid for only small angles of inclination [34]. Formulas for the mutual impedance between nonparallel overhead and buried conductors have been obtained in [35]. However, the formula derived in [35] contains an integral, which does not have an analytical solution. Therefore a numerical integration algorithm has been suggested.

On the other hand, full-wave models have the capability of modelling nonuniform struc-

tures accurately. These models represent the structure to be solved using Maxwell's equations [36] which are more electromagnetically detailed than transmission line theory. However these models are often associated with high computational costs and typically requires iterative methods to obtain solutions [26, 37, 38]. This makes them not very suitable for circuit-based time-domain simulations. Efforts in combining method of moments (MoM)

Thin-wire scattering equations are a simplified version of Maxwell's equations which define the electric field (referred to as the scattered electric field) generated by a current flowing through a thin-wire (a wire whose cross-sectional dimensions are much smaller than the minimum wavelength of interest). The scattered electric field produced by a thin-wire of length  $\ell$  placed along the  $z$  axis in free-space can be expressed in terms of vector and scalar potentials as [39],

$$\mathbf{E}^s = -j\omega\mathbf{A} - \nabla\Phi \quad (2.3)$$

with

$$\mathbf{A}(\mathbf{r}) = \frac{\mu}{4\pi} \int_0^\ell I(z')\hat{a}_z g(\mathbf{r}, \mathbf{r}') dz'$$

and,

$$\Phi(\mathbf{r}) = \frac{1}{4\pi\epsilon} \int_0^\ell \rho(z')g(\mathbf{r}, \mathbf{r}') dz'$$

where  $z'$  is the length variable along the axis of wire,  $\mathbf{r} = x\hat{a}_x + y\hat{a}_y + z\hat{a}_z$  is the position vector of the observation point and  $\mathbf{r}'$  is the position vector of the source.  $I(z')$  and  $\rho(z')$  are the current and charge density along the wire.  $g(\mathbf{r}, \mathbf{r}')$  is the scalar Green's function given by [39]

$$g(\mathbf{r}, \mathbf{r}') = \frac{e^{-j\beta|\mathbf{r}-\mathbf{r}'|}}{|\mathbf{r}-\mathbf{r}'|} \quad (2.4)$$

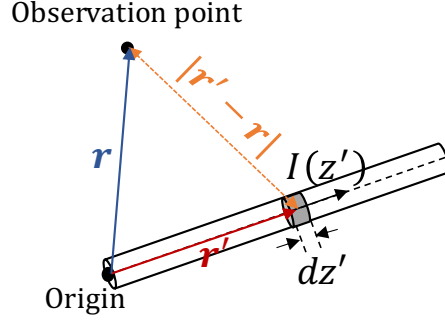


**Fig. 2.2:** Illustration of the space variable ( $R$ ) in the Green's function under thin-wire approximation.

where  $\beta = \omega\sqrt{\mu_0\epsilon_0}$  is the phase constant. The space variable  $|\mathbf{r} - \mathbf{r}'|$  in the Green's function is illustrated graphically in Fig. 2.2. In order to avoid singularity in the Green's function observation points ( $\mathbf{r}$ ) are always selected to be on the wire surface or further. Scattering equations are not uniform in space as Telegrapher's equations, which makes them applicable for more general cases that involve non-parallel currents. They are also simpler and less detailed than Maxwell's equations which makes them easier to solve compared to full-wave models.

Tkachenko *et al.* have used thin-wire scattering equations to model single-conductor transmission lines of finite length and single-conductor bent lines above perfectly conducting (PEC) ground in the frequency-domain in [40] and [41] respectively. In these models, transmission-line-like equations have been obtained based on the assumption that the scattered electric field lies only on the transverse plane to the conductor which can be written as,

$$\hat{a}_z \cdot \mathbf{E}^s = 0 \quad (2.5)$$

where  $\hat{a}_z$  the unit vector in  $z$  direction (direction of propagation), and  $\mathbf{E}^s$  is the scattered

electric field. Transmission-line-like equations for a finite length wire of length  $\ell$  has then been obtained as [40]

$$\frac{dV(z)}{dz} + j\omega \frac{\mu}{4\pi} \int_0^\ell g(z, z') I(z') dz' = E_z^e(h, z) \quad (2.6a)$$

$$\frac{d}{dz} \int_0^\ell g(z, z') I(z') dz' + j\omega 4\pi\epsilon V(z) = 0. \quad (2.6b)$$

In (2.6),  $E_z^e(h, z)$  is the incident electric field at the height of the wire  $h$ . When conductors are above PEC ground Green's function can be obtained using image theory by replacing the ground with an image conductor placed at a depth equal to the height of the original conductor. Green's function for this case is given by [39]

$$g(z, z') = \left( \frac{e^{-j\beta R_s}}{R_s} - \frac{e^{-j\beta R_i}}{R_i} \right) \quad (2.7)$$

where  $R_s$  and  $R_i$  are the distances to an observation point  $z$  from the current element and the image current element at a source point  $z'$ , respectively. Since the purpose of the research in [40] has been on analyzing field coupling at high frequencies, (2.6) has not been simplified from their original form. Since, the integral terms in (2.6) do not have a closed-form analytical solution, an iterative method based on the perturbation theory has been used to arrive at solutions in the frequency-domain.

In [29], an EMT-compatible simulation model for lossless, crossing single-conductor (*i.e.* nonuniform) overhead transmission lines of finite length has been proposed based on electromagnetic scattering theory. This model has been later extended to a lossless multiconductor structure over PEC ground in [42]. In both [29, 42], conductors and ground have been assumed to be lossless. The initial mathematical modelling has been developed using elec-

tromagnetic scattering equations. For a case of two single-conductor lines (say  $i$  and  $j$ ) crossing each other at an angle of  $\alpha$ , the vector and scalar potentials of the scattered electric field acting upon line  $i$  can be written as

$$A_{z_i}(z_i) = \frac{\mu}{4\pi} \int_0^{\ell_i} g(z_i, z'_i) I_i(z'_i) dz'_i + \cos \alpha \frac{\mu}{4\pi} \int_0^{\ell_j} g(z_i, z_j, \alpha) I_j(z_j) dz_j \quad (2.8a)$$

and,

$$\Phi(z_i) = \frac{1}{4\pi\epsilon} \int_0^{\ell_i} g(z_i, z'_i) \rho_i(z'_i) dz'_i + \frac{1}{4\pi\epsilon} \int_0^{\ell_j} g(z_i, z_j, \alpha) \rho_j(z_j) dz_j. \quad (2.8b)$$

In (2.8)  $\ell_i$  and  $\ell_j$  are the lengths of conductors  $i$  and  $j$ .  $I_i$  and  $I_j$  are the currents and  $\rho_i$  and  $\rho_j$  are the electric charge densities at a field point on the surface of the wires  $i$  and  $j$ , respectively. Then they have been simplified into a closed-form transmission-line-like form considering the geometrical characteristics and frequencies of interest in typical power transmission lines. For the case of power transmission lines where the maximum cross-sectional dimension of the structure  $h$  is very small compared to the minimum wavelength of interest (*i.e.*,  $h \ll \lambda$ ), the exponential terms in (2.7) can be approximated as unity [39] which simplifies the integral terms in (3.2) as [39]

$$\begin{aligned} \int g(z, z') I(z') dz' &= \int \left( \frac{e^{-j\beta R_s}}{R_s} - \frac{e^{-j\beta R_i}}{R_i} \right) I(z') dz' \\ &\simeq \int \left( \frac{1}{R_s} - \frac{1}{R_i} \right) dz' I(z). \end{aligned} \quad (2.9)$$

This simplification enables to derive closed form transmission line equations in the form of [29]

$$\frac{d}{dz} \begin{bmatrix} \mathbf{V}(z, j\omega) \\ \mathbf{I}(z, j\omega) \end{bmatrix} = -j\omega \begin{bmatrix} \mathbf{L}(z) & 0 \\ 0 & \mathbf{C}(z) \end{bmatrix} \begin{bmatrix} \mathbf{V}(z, j\omega) \\ \mathbf{I}(z, j\omega) \end{bmatrix} \quad (2.10)$$

where the space-dependent PUL inductance  $\mathbf{L}$  and capacitance  $\mathbf{C}$  matrices are given by

$$\mathbf{L}(z) = \frac{\mu}{4\pi} \begin{bmatrix} \xi_{ii}(z) & \cos \alpha \xi_{ij}(z) \\ \cos \alpha \xi_{ji}(z) & \xi_{jj}(z) \end{bmatrix} \quad (2.11a)$$

$$\mathbf{C}(z) = \frac{4\pi\epsilon}{\xi_{ii}(z)\xi_{jj}(z) - \xi_{ij}(z)\xi_{ji}(z)} \begin{bmatrix} \xi_{jj}(z) & -\xi_{ij}(z) \\ -\xi_{ji}(z) & \xi_{ii}(z) \end{bmatrix} \quad (2.11b)$$

The functions  $\xi_{ii}(z)$  and  $\xi_{ij}(z)$  used for the calculation of  $\mathbf{L}(z)$  and  $\mathbf{C}(z)$  in (2.11) are determined using [29]

$$\xi_{ii}(z) = \sinh^{-1} \left( \frac{\ell_i - z}{a_i} \right) - \sinh^{-1} \left( \frac{-z}{a_i} \right) - \sinh^{-1} \left( \frac{\ell_i - z}{2h_i} \right) + \sinh^{-1} \left( \frac{-z}{2h_i} \right) \quad (2.12a)$$

$$\begin{aligned} \xi_{ij}(z) = & \sinh^{-1} \left( \frac{\ell_j - c_j + (c_i - z) \cos \alpha}{\sqrt{((c_i - z) \sin(\alpha))^2 + (h_i - h_j)^2}} \right) \\ & - \sinh^{-1} \left( \frac{-c_j + (c_i - z) \cos \alpha}{\sqrt{((c_i - z) \sin(\alpha))^2 + (h_i - h_j)^2}} \right) \\ & - \sinh^{-1} \left( \frac{\ell_j - c_j + (c_i - z) \cos \alpha}{\sqrt{((c_i - z) \sin(\alpha))^2 + (h_i + h_j)^2}} \right) \\ & + \sinh^{-1} \left( \frac{-c_j + (c_i - z) \cos \alpha}{\sqrt{((c_i - z) \sin(\alpha))^2 + (h_i + h_j)^2}} \right) \end{aligned} \quad (2.12b)$$

Since lines are assumed to be frequency-independent, (2.10) can be conveniently converted into the time-domain as

$$\frac{\partial}{\partial z} \begin{bmatrix} \mathbf{V}(z, t) \\ \mathbf{I}(z, t) \end{bmatrix} = -\frac{\partial}{\partial t} \begin{bmatrix} \mathbf{L}(z) & 0 \\ 0 & \mathbf{C}(z) \end{bmatrix} \begin{bmatrix} \mathbf{V}(z, t) \\ \mathbf{I}(z, t) \end{bmatrix} \quad (2.13)$$

and solved using a single dimensional FDTD (1D-FDTD) algorithm [16].

## 2.2 Inclusion of Frequency-Dependent Losses

A real power transmission line inherits both frequency-dependent conductor and ground losses. The well-known formula for the frequency-dependent PUL conductor loss which accounts for the skin effect is given by [43],

$$Z_{\text{cond}} = \frac{\rho_{\text{cond}} \times m}{2\pi a} \coth(0.777 \times m \times a) + \frac{0.356\rho_{\text{cond}}}{\pi a^2} \quad (2.14a)$$

where,

$$m = \sqrt{\frac{j\omega\mu_o}{\rho_{\text{cond}}}} \quad (2.14b)$$

$\rho_{\text{cond}}$  is the resistivity of the conductor,  $\mu_o$  is the permittivity of free space and  $a$  is the radius of the conductor. The self-impedance of a conductor consists of  $Z_{\text{cond}}$  and the ground return impedance. Since the clearance between ground and other conductors is much larger than conductor radii in overhead lines, the current distribution inside a wire is not expected to change due to proximity effect. Therefore, eq. (2.14) can be assumed to be valid for non-uniform structures discussed in Section 1 as well.

### 2.2.1 Overhead wires above lossy ground

When the ground is lossy (finitely conducting) the transmission line structure is considered as a lossy half-space problem [19]. In a finitely conducting ground the electromagnetic fields generated by the conductor penetrates into the ground with a penetration depth that depends on the frequency. This in other words means that the PUL impedance and admittance (referred to as the earth return impedance and admittance) of the wire structure is now frequency-dependent. For overhead lines the frequency dependency of the earth return admittance does not play a significant role compared to the impedance and therefore is neglected [25]. The ground return impedance of uniform (*i.e.* parallel to each other and have constant radii) overhead wires placed at  $(x_i, y_i)$  and  $(x_j, y_j)$  on the transverse plane is calculated using the well-known Carson's formula [19] given by

$$Z_{ij} = \frac{j\omega\mu_0}{2\pi} \left[ \ln \left( \frac{D_{ij}}{d_{ij}} \right) + 2 \int_0^\infty \frac{e^{-\alpha \cos(\theta_{ij})} \cos(\alpha \sin(\theta_{ij}))}{\alpha + \sqrt{\alpha^2 + jr_{ij}^2}} d\alpha \right] \quad (2.15a)$$

where,

$$D_{ij} = \sqrt{(x_i - x_j)^2 + (y_i + y_j)^2}$$

$$d_{ij} = \sqrt{(x_i - x_j)^2 + (y_i - y_j)^2}$$

$$\theta_{ij} = \tan^{-1} \left( \frac{x_i - x_j}{y_i + y_j} \right)$$

$$r_{ij} = D_{ij} \sqrt{\omega\mu_0\sigma_g}$$

$\sigma_g$  is the conductivity of ground. For self impedance consider  $i = j$  and  $d_{ij} = a_i$ , where  $a_i$  is the radius of conductor  $i$ . The integral term in (2.15) does not have a analytical solution and therefore has to be calculated numerically. Deri *et al.* developed a method to approximate

this integral for low frequencies using so-called complex image theory where the finitely conducting ground is replaced with a PEC ground at a complex depth as shown in Fig. 2.3 [44]. With this representation a simplified closed-form formula is obtained as [44]

$$Z_{ij} = \frac{j\omega\mu_0}{2\pi} \ln \left( \frac{D'_{ij}}{d_{ij}} \right) \quad (2.16a)$$

where,

$$D'_{ij} = \sqrt{(y_i + y_j + 2p)^2 + (x_i - x_j)^2}$$

and

$$p = \frac{1}{\sqrt{j\omega\mu_0\sigma_g}}.$$

Complex image theory provides a simple graphical approach for modelling conductors over finitely conducting ground. As it was discussed in Section 2.1, when using scattering equations, Green's functions for nonuniform conductors above PEC ground is obtained using image theory. Similarly, complex image theory stands as a suitable candidate for obtaining Green's functions of nonuniform conductors above finitely conducting ground. In [45–47] Ametani *et al.* have calculated frequency-dependent ground return impedance and admittance for lines of finite length and demonstrated the difference with Carson's ground return impedance. In [34], the per-unit-length (PUL) parameters for lossy and nonuniform multiconductor transmission lines have been formulated assuming the currents are parallel at every cross section, and therefore, the model is valid for only small angles of inclination. Further research regarding PUL parameters of non-uniform frequency-dependent lines has been performed and presented in this thesis.

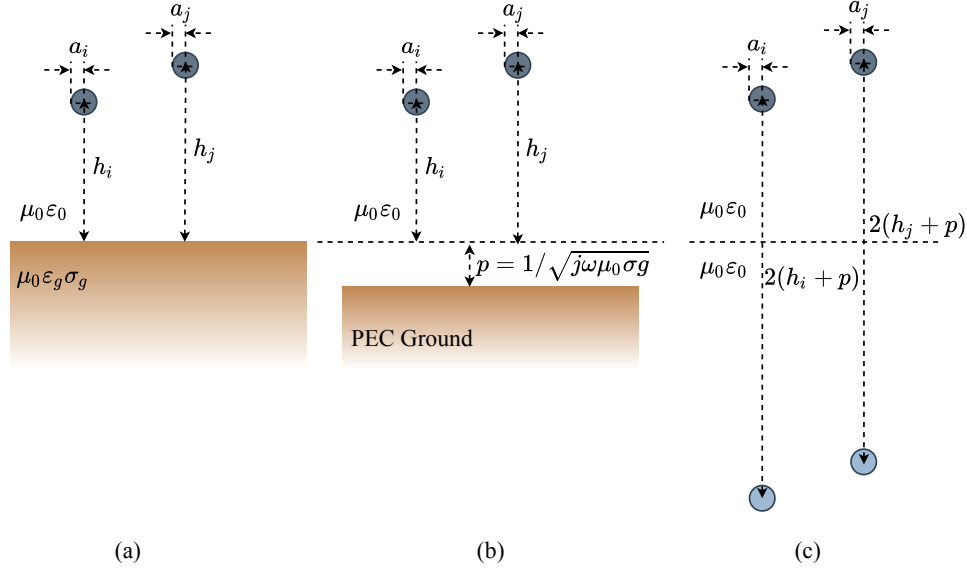


**Fig. 2.3:** Illustration of complex image theory: (a) Overhead lines above lossy ground. (b) Lossy ground replaced with a PEC ground at a complex depth. (c) PEC ground replaced with image conductors.

### 2.2.2 Buried wires in lossy ground

When a transmission line is built crossing a buried pipeline transients and power-frequency voltages can be induced on the pipeline [14]. In contrast to overhead conductors, buried conductors creates a more complex electromagnetic problem since the wires are now placed inside the lossy half-space, The mutual earth return impedance of two uniform conductors buried in lossy ground at  $(x_i, d_i)$  and  $(x_j, d_j)$  on the transverse plane ( $d_i$  and  $d_j$  are burial epths) is calculated using Pollaczek's formula [20] given by

$$Z_{\text{buried},ij} = \frac{j\omega\mu_0}{2\pi} \left[ K_0(kr) - K_0(kR) + 2 \int_0^\infty \frac{e^{-D\sqrt{\lambda^2+k^2}} \cos(\lambda x)}{\lambda + \sqrt{\lambda^2 + k^2}} d\lambda \right] \quad (2.17a)$$

where,

$$x = |x_i - x_j|$$

$$D = (d_i + d_j)$$

$$r = \sqrt{(x_i - x_j)^2 + (d_i - d_j)^2}$$

$$R = \sqrt{(x_i - x_j)^2 + (d_i + d_j)^2}$$

$$k = \sqrt{j\omega\mu_0\sigma_g}$$

$K_0$  denotes the modified Bessel function of zeroth order [20]. Similar to Carson's impedance, Pollaczek's impedance formula is ill-conditioned (does not possess an analytical solution) and has to be calculated numerically. Closed-form approximations of Pollaczek's impedance for bare and shielded conductors have been derived by many researchers as listed in [28]. Once the ground return impedance of buried wires is calculated, the ground return admittance is obtained using [28]

$$Y_{\text{buried}} = \frac{\gamma_g^2}{Z_{\text{buried}}} \quad (2.18)$$

where  $\gamma_g = \sqrt{j\omega\mu_0(\sigma_g + j\omega\varepsilon_g)}$  is the propagation constant in the ground. Unlike in overhead wires the admittance of underground wires tend to be highly frequency-dependent [25] and has to be considered when formulating the transmission line problem.

Image models for buried wires and their validity are discussed in [48–50]. In contrast to complex image theory for overhead wires where the earth half-space is replaced with air and image conductors are placed at complex a depth, here the air half-space is replaced with earth and image conductors are seen to be placed equidistant to the earth-air interface. Fields generated from the image are then multiplied by a suitable reflection coefficient called

the Fresnel reflection coefficient [48]. The Green's function will now read as [49]

$$g(z, z') = \left( \frac{e^{-j\beta R_s}}{R_s} - \Gamma_0^{\text{ref}} \frac{e^{-j\beta R_i}}{R_i} \right) \quad (2.19a)$$

where  $\Gamma_0^{\text{ref}}$  is the Fresnel reflection coefficient due to earth-to-air interface given by [48]

$$\Gamma_0^{\text{ref}} = \frac{\varepsilon_{\text{eff}} - \varepsilon_0}{\varepsilon_{\text{eff}} + \varepsilon_0}. \quad (2.19b)$$

In (2.19b),  $\varepsilon_{\text{eff}}$  is the complex permittivity of earth given by

$$\varepsilon_{\text{eff}} = \varepsilon_g + \frac{\sigma_g}{j\omega}. \quad (2.20)$$

It should be noted that the complex image depth for overhead wires is in fact a different representation of the air-to-earth Fresnel reflection coefficient [51]. An iterative solution for the electromagnetic field coupling to buried wires has been suggested in [52].

In the case of buried pipelines nearby overhead transmission lines, conductors are present in both air and earth of the half-wave problem. Pollaczek developed expressions for self impedance of buried conductors and the mutual impedance between parallel overhead and buried conductors in the form of infinite integrals [53]. The infinite integral format of the mutual impedance between an overhead at a height  $h$  and buried wire at a depth  $d$  placed parallel to each other along the  $z$  direction with a horizontal gap of  $a$  is given by [54]

$$Z_{\text{ob}} = \frac{j\omega\mu_0}{2\pi} \int_0^\infty \frac{2e^{-\lambda h} e^{-d\sqrt{\lambda^2 - k_e^2}} \cos(\lambda a)}{\lambda + \sqrt{\lambda^2 - k_e^2}} d\lambda \quad (2.21a)$$

where,

$$k_e^2 = -j\omega\mu_0\sigma_g. \quad (2.21b)$$

Pollaczek's integral does not have an analytical solution and is highly unstable during numerical integration [53, 55]. Therefore, several researchers have developed closed-form approximate formulas for Pollaczek's formula among which, Lucca's formulation in [54] is considered as the most accurate [55]. Lucca's formula provides a simple closed-form expression for the mutual coupling between parallel overhead and buried conductors as

$$\frac{j\omega\mu_0}{2\pi} \left[ \ln \frac{\bar{R}_{12}}{R_{12}} + \frac{2\bar{H}_{12}}{3\gamma^3} \frac{\bar{H}_{12}^2 - 3a^2}{\bar{R}_{12}^6} \right] \quad (2.22a)$$

where,

$$\gamma = jk_e \quad (2.22b)$$

$$H_{12} = h + d \quad (2.22c)$$

$$\bar{H}_{12} = h + d + \frac{2}{\gamma} \quad (2.22d)$$

$$R_{12} = \sqrt{H_{12}^2 + a^2} \quad (2.22e)$$

and

$$\bar{R}_{12} = \sqrt{\bar{H}_{12}^2 + a^2} \quad (2.22f)$$

based on the approximation that for typical frequencies and ground conductivity values in power lines,

$$e^{-d\sqrt{\lambda^2 - k_e^2}} \approx e^{-d\lambda}. \quad (2.23)$$

Lucca's method of simplification in [54] appears to be easily adaptable for nonparallel con-

ductors as well. Mutual impedance formulation for two inclined conductors placed in the same medium is given in [56] while the same for two nonparallel conductors placed in two media is given in [57]. The formulations in both [56] and [57] are in the form of infinite integrals with no analytical solutions.

## 2.3 Time-Domain Implementation of Non-Uniform Transmission Lines

Time-domain implementation of frequency-independent transmission line is straight forward as discussed in Section 2.1. However, when an equation with frequency-dependent PUL parameters like (2.2) is converted into the time-domain, multiplications between frequency dependent terms get converted into convolutions. Convolution terms can be handled using recursive calculations by fitting the frequency dependent parameters into a rational function [31,32].

A time-domain model for multiconductor frequency-independent non-uniform lines utilizing finite-element-method (FEM) has been introduced in [58]. However, this model involves a numerical integration at each time step. A frequency-dependent non-uniform model based on an iterative and adaptive perturbation technique is proposed in [59]. One dimensional finite-difference methods (1D FDTD), where the wave propagation is considered only along the conductor, have been used to model lossy nonuniform transmission lines in [60–62]. In these models losses are assumed to be frequency-independent and the nonuniformity is conductors being exponentially and linearly tapered or twisted which is not the case with overhead lines. However, this suggests that finite-difference methods are a suitable candidate for solving nonuniform structures in general. The FDTD algorithms discretize the

transmission line structure into a finite number of space segments and calculate the voltage and current of each space segment at every time step. The time step  $\Delta t$  and space step  $\Delta x$  should be chosen such that

$$\frac{\Delta x}{\Delta t} \geq v \quad (2.24)$$

where  $v$  is the speed of propagation, in order to ensure stability.

An approach for modelling uniform frequency-dependent single-conductor overhead transmission lines using a modified finite-difference time-domain (MFDTD) algorithm within a circuit simulator has been developed in [27]. In [27] the frequency-dependent PUL impedance matrix is first fitted into a rational function using a sum of first-order poles with corresponding residues, a proportional term, and a constant term [32] as.

$$Z(j\omega) = R + j\omega L + Z'(j\omega) \quad (2.25a)$$

where

$$Z'(j\omega) = \sum_{k=1}^M \frac{a_k}{j\omega - \alpha_k}. \quad (2.25b)$$

In (2.25)  $a_k$  is the residue corresponding to each pole  $\alpha_k$ . Converting transmission line equations with fitted PUL impedance into time-domain gives

$$\frac{\partial}{\partial z} V(z, t) = -RI(z, t) - L \frac{\partial}{\partial t} I(z, t) - Z'(t) * I(z, t) \quad (2.26a)$$

and

$$\frac{\partial}{\partial z} I(z, t) = -C \frac{\partial}{\partial t} V(z, t). \quad (2.26b)$$

The MFDTD algorithm then solves (2.26) while calculating the convolution term in (2.26a)

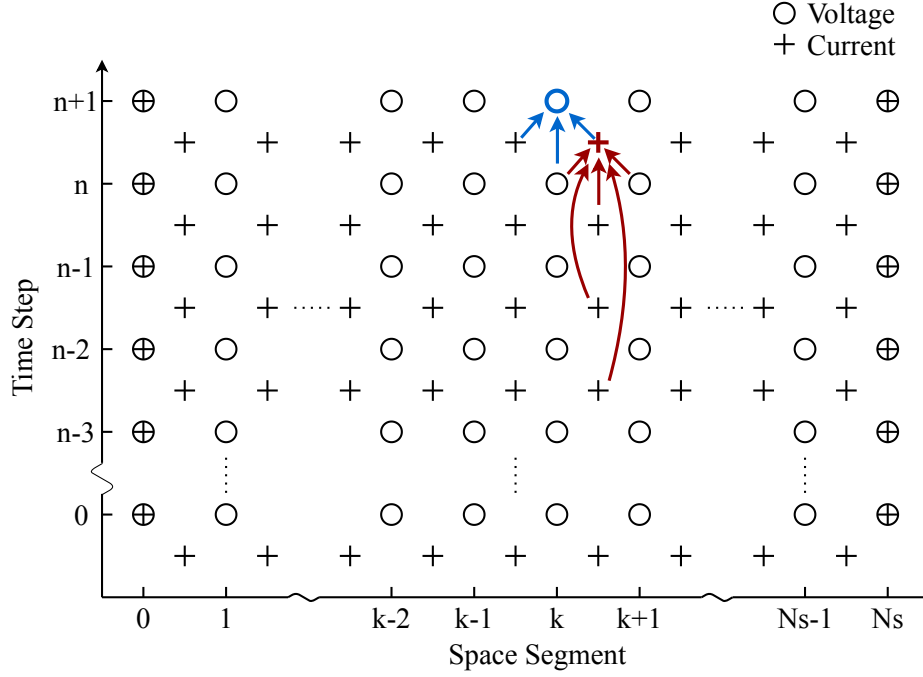


**Fig. 2.4:** Illustration of the calculation of voltage and current of space segment  $k$  at time-step  $n$  in the MFDTD algorithm in [27].

using current ( $I$ ) values of three past time-steps (*i.e.* using recursive convolutions). FDTD algorithms calculate voltages and currents at interleaved nodes along the span of the line [16] as shown in Fig. 2.4. In order to facilitate the implementation on a circuit simulator, MFDTD algorithm calculates both current and voltage at the terminal nodes. The updating equation for the current at a space-segment  $k$  and a time iteration  $n$  is given by [27]

$$I_{k+\frac{1}{2}}^{n+\frac{1}{2}} = Z_2^{-1} \left[ Z_1 I_{k+\frac{1}{2}}^{n-\frac{1}{2}} + \Delta z (\xi + \chi) I_{k+\frac{1}{2}}^{n-\frac{3}{2}} - (V_{k+1}^n - V_{k+1}^n) - \Delta z \Psi^n \right] \quad (2.27a)$$

where

$$Z_1 = \Delta z \left( \frac{L}{\Delta t} - \frac{R}{2} + \frac{\Gamma}{2} - 2\xi - \chi \right) \quad (2.27b)$$

$$Z_2 = \Delta z \left( \frac{L}{\Delta t} + \frac{R}{2} - \frac{\Gamma}{2} - \xi \right) \quad (2.27c)$$

$$\xi = \sum_{i=1}^M \frac{a_i}{\alpha_i} \left[ \frac{1}{\alpha_i \Delta t} \left( 1 + \frac{1}{\alpha_i \Delta t} - \frac{e^{\alpha_i \Delta t}}{\alpha_i \Delta t} \right) \right] \quad (2.27d)$$

$$\chi = \sum_{i=1}^M \frac{a_i}{\alpha_i} \left[ \frac{1}{\alpha_i \Delta t} (e^{\alpha_i \Delta t} - 1) \right] \quad (2.27e)$$

$$\Gamma = \sum_{i=1}^M \frac{a_i}{\alpha_i} \quad (2.27f)$$

$$\Psi^n = \sum_{i=1}^M \frac{a_i}{\alpha_i} \Psi_i^n \quad (2.27g)$$

$$\begin{aligned} \Psi_i^n \frac{e^{\alpha_i \Delta t}}{\alpha_i \Delta t} \left( 1 + \frac{1}{\alpha_i \Delta t} - \frac{e^{\alpha_i \Delta t}}{\alpha_i \Delta t} \right) & \left( 2I_{k+\frac{1}{2}}^{n-\frac{3}{2}} - I_{k+\frac{1}{2}}^{n+\frac{5}{2}} - I_{k+\frac{1}{2}}^{n-\frac{1}{2}} \right) \\ & + \frac{e^{\alpha_i \Delta t}}{\alpha_i \Delta t} (e^{\alpha_i \Delta t} - 1) \left( I_{k+\frac{1}{2}}^{n-\frac{3}{2}} - I_{k+\frac{1}{2}}^{n-\frac{5}{2}} \right) + e^{\alpha_i(z)\Delta t} \Psi_i^{n-1}. \end{aligned} \quad (2.27h)$$

In (2.27),  $\Delta z$  is the space step and  $\Delta t$  is the time step which has to be selected based on the stability criteria.: The voltage updating equation is given by [27]

$$V_k^{n+1} = Y_2^{-1} \left[ Y_1 V_k^n - (I_{k+\frac{1}{2}}^{n+\frac{1}{2}} - I_{k-\frac{1}{2}}^{n+\frac{1}{2}}) \right] \quad (2.28a)$$

where

$$Y_1 = \Delta z \left( \frac{C}{\Delta t} - \frac{G}{2} \right) \quad (2.28b)$$

$$Y_2 = \Delta z \left( \frac{C}{\Delta t} + \frac{G}{2} \right). \quad (2.28c)$$

Currents at the terminal nodes are obtained using [27]

$$I_0^{n+1} = -I_0^n - Y_1 V_0^n + Y_2 V_0^{n+1} + 2I_0^{n+\frac{1}{2}} \quad (2.29)$$

$$I_{N_S}^{n+1} = -I_{N_S}^n - Y_1 V_{N_S}^n + Y_2 V_{N_S}^{n+1} + 2I_{N_S}^{n+\frac{1}{2}}. \quad (2.30)$$

The calculation process of the MFDTD algorithm is graphically illustrated in Fig. 2.4.

Theethayi *et al.* have used a similar FDTD algorithm to solve the transmission line problem of a single buried conductor in [28]. Since both impedance and admittance are frequency dependent in buried conductors, both current and voltage calculations involve recursive convolutions. The model in [28] has not been intended for circuit simulators and therefore, only the voltage is calculated at the terminal nodes. In addition to modelling non-uniform wires MFDTD algorithm has the potential to model non-uniform field-to-line coupling such as from nearby lightning strikes [27]. Current transmission line models in EMT simulators do not have the capability to incorporate external field coupling to transmission lines [17, 18].

## 2.4 External Field Coupling to Non-Uniform Transmission Lines

Lightning is a major factor contributing to overvoltage transients in overhead power lines which ultimately lead to power outages [63, 64]. A lightning incidence can be a direct strike to a phase conductor or a nearby strike to the earth's surface [65]. Direct lightning strikes can be modelled as a current injection [66, 67]. On the other hand, the effect due to a nearby

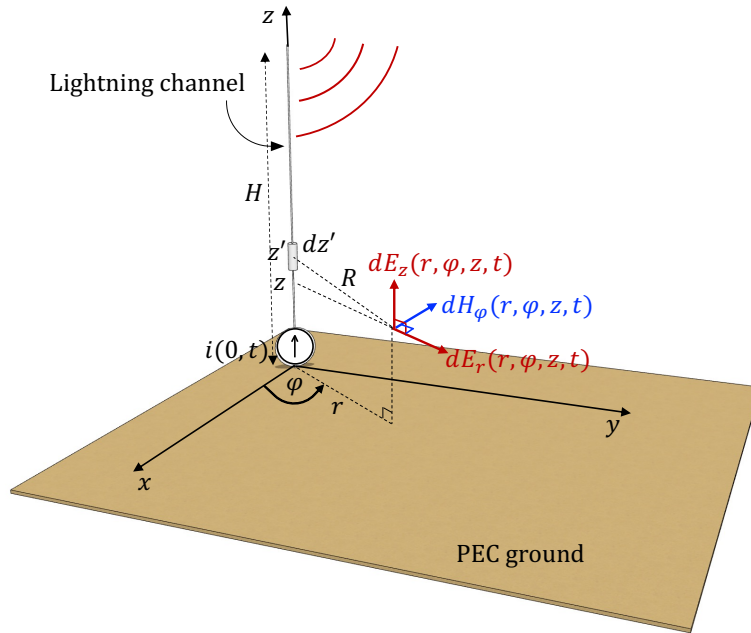


**Fig. 2.5:** Radiated electromagnetic fields by an infinitesimal current element of a monopole antenna.

lightning strike to ground has to be modelled as an external nonuniform field coupling to the transmission line [68]. In [68], the lightning return stroke channel is modelled as a vertical monopole antenna that radiates electromagnetic fields. For a monopole antenna above PEC ground as shown in Fig. 2.5, the radiated electric and magnetic fields at a location  $(r, z, \varphi)$

and a time  $t$  can be calculated as [69]

$$\begin{aligned}
 E_r^{\text{PEC}}(r, z, \varphi, t) = & \frac{1}{4\pi\epsilon_0} \int_0^H \left[ \frac{3r(z-z')}{R^5} \int_0^t i(z', \tau - R/c) d\tau \right. \\
 & + \frac{3r(z-z')}{cR^4} i(z', \tau - R/c) \\
 & \left. + \frac{r(z-z')}{c^2R^3} \frac{\partial i(z', \tau - R/c)}{\partial t} \right] dz'
 \end{aligned} \tag{2.31a}$$

$$\begin{aligned}
 E_z^{\text{PEC}}(r, z, \varphi, t) = & \frac{1}{4\pi\epsilon_0} \int_0^H \left[ \frac{2(z-z')^2 - r^2}{R^5} \int_0^t i(z', \tau - R/c) d\tau \right. \\
 & + \frac{2(z-z')^2 - r^2}{cR^4} i(z', \tau - R/c) \\
 & \left. - \frac{r^2}{c^2R^3} \frac{\partial i(z', \tau - R/c)}{\partial t} \right] dz'
 \end{aligned} \tag{2.31b}$$

and

$$H_\varphi^{\text{PEC}}(r, z, \varphi, t) = \frac{1}{4\pi} \int_0^H \left[ \frac{r}{R^3} i(z', \tau - R/c) + \frac{r}{cR^2} \frac{\partial i(z', \tau - R/c)}{\partial t} \right] dz' \tag{2.31c}$$

where  $c$  is the speed of light in free space,  $\epsilon_0$  is the permittivity of free space, and  $R = \sqrt{r^2 + (z - z')^2}$ . The three terms in the electric field equations are generally referred to as the static, induction and radiation components respectively [70].

There are several ways to model the current distribution ( $i(z', t)$ ) along the lightning channel among which the so-called ‘engineering models’ are the simplest. They have also been successful in predicting the features of lightning electromagnetic fields in close agreement with experimental data [71,72]. Two well known engineering models are the modified transmission line linear (MTLL) and modified transmission line exponential (MTLE) where  $i(z', t)$  is

calculated respectively using

$$i(z', t) = i(0, t - \frac{z'}{v}) \left(1 - \frac{z'}{H}\right) \quad (2.32a)$$

and

$$i(z', t) = i(0, t - \frac{z'}{v}) e^{z'/\lambda}. \quad (2.32b)$$

In (2.32),  $v$  is the propagation speed of the current pulse along the lightning channel while  $\lambda$  represents the attenuation of the current amplitude as it travels along the channel. The channel base current ( $i(0, t)$ ) is generally calculated using Heidler formulation given by [73]

$$i(0, t) = \frac{I_0}{\eta} \frac{(t/\tau_1)^n}{1 + (t/\tau_1)^n} e^{-t/\tau_2}. \quad (2.33)$$

Values for  $I_0$ ,  $\eta$ ,  $\tau_1$ ,  $\tau_2$  and  $n$  for different current shapes can be found in [74]. Thus calculated lightning fields that propagate through the air and reach the cross section of the line are then considered as an external excitation acting upon the transmission line. Three popular formulations used to incorporate external nonuniform field coupling to transmission lines are Taylor *et al.*'s formulation [75], Agrawal *et al.*'s formulation [76] and Rachidi's formulation [77]. These three formulations will be referred to as Taylor model, Agrawal model and Rachidi model herein. Transmission line equations with external field coupling according to Taylor model in the frequency domain is given by [75]

$$\frac{d\mathbf{V}(z)}{dz} + \mathbf{Z}\mathbf{I}(z) = -j\omega \int_0^h \mathbf{B}_y^{\text{inc}}(z, x) dx. \quad (2.34a)$$

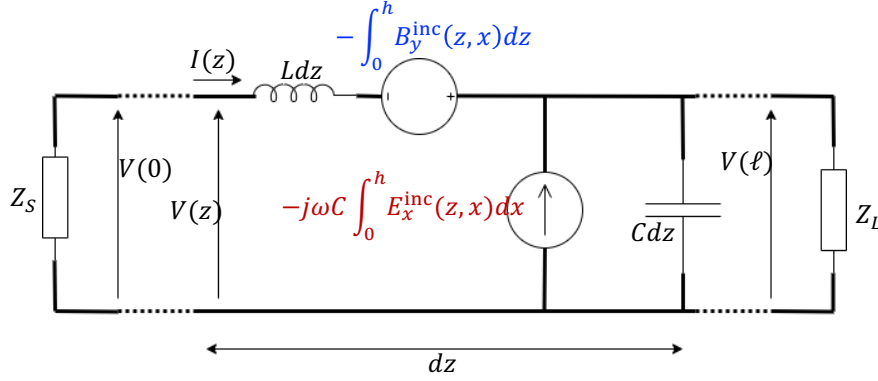


**Fig. 2.6:** Equivalent circuit of the Taylor model [75] for external field coupling.

and

$$\frac{d\mathbf{I}(z)}{dz} + \mathbf{Y}\mathbf{V}(z) = -j\omega\mathbf{C} \int_0^h \mathbf{E}_x^{\text{inc}}(z, x) dx. \quad (2.34b)$$

where  $\mathbf{E}^{\text{inc}}$  and  $\mathbf{B}^{\text{inc}}$  are the vectors containing the incident electric and magnetic field respectively on each line. The equivalent circuit of the Taylor model for a single conductor transmission line along with terminal connections is shown in Fig. 2.6.

Similarly, according to Agrawal model external fields are incorporated in to transmission line equations as [76]

$$\frac{d}{dz}\mathbf{V}^s(z) + \mathbf{Z}\mathbf{I}(z) = \mathbf{E}_z^{\text{inc}}(z, h) - \mathbf{E}_z^{\text{inc}}(z, 0) \quad (2.35a)$$

and

$$\frac{d}{dz}\mathbf{I}(z) + \mathbf{Y}\mathbf{V}^s(z) = 0 \quad (2.35b)$$

where  $\mathbf{V}^s$  is the scattered voltage vector [76]. When transmission line equations are represented with scattered voltage the terminal equations should be adjusted accordingly which

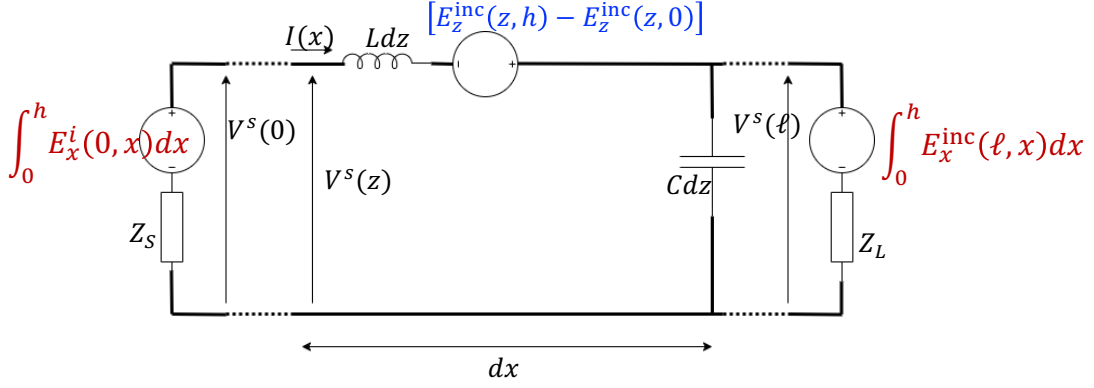


**Fig. 2.7:** Equivalent circuit of the Agrawal model [76] for external field coupling.

will be discussed in a later section. The equivalent circuit of the Agrawal model is shown in Fig. 2.7.

Transmission line equations with external field coupling included according to Rachidi model are [77]

$$\frac{d\mathbf{V}(z)}{dz} + \mathbf{Z}\mathbf{I}^s(z) = 0 \quad (2.36a)$$

and

$$\frac{d\mathbf{I}(z)}{dz} + \mathbf{Y}\mathbf{V}(z) = -\frac{\mathbf{C}}{\mu_0\epsilon_0} \int_0^h \left[ \frac{\partial \mathbf{B}_x^{\text{inc}}(z, x)}{\partial z} - \frac{\partial \mathbf{B}_z^{\text{inc}}(z, x)}{\partial y} \right] dx. \quad (2.36b)$$

where  $\mathbf{I}^s$  is the scattered current vector. The equivalent circuit of the Rachidi model is shown in Fig. 2.8.

It is seen that while the Taylor model requires both external electric and magnetic field to incorporate the field-to-line coupling, Agrawal and Rachidi models require only the electric field and the magnetic field respectively. While theoretically all three methods are equivalent, Taylor model provides a simpler connection with the external circuit compared to the other

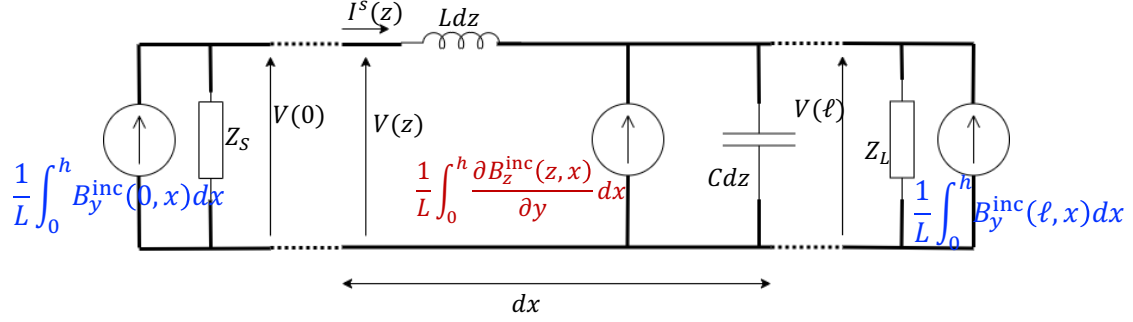


**Fig. 2.8:** Equivalent circuit of the Rachidi model [77] for external field coupling.

two methods. Agrawal and Rachidi models are beneficial when either one of electric field or magnetic field measurement data respectively, is available at a particular transmission line which needs to be analysed using transmission line theory.

Time-domain models to simulate lightning induced voltages on lossy uniform transmission lines have been introduced in [78, 79]. EMT simulator compatible models to analyze transients on uniform transmission lines due to nearby lightning strikes have been proposed in [27, 80]. In these works, Cooray-Rubinstien (CR) approximation [70] has been the widely used method to calculate the horizontal electric field distribution over lossy ground due to lightning required for the implementation of Agrawal model. In the CR method the the horizontal field at ground level is obtained from the magnetic field using the expression for the surface impedance as [81]

$$E_r(r, z = 0, \varphi, j\omega) \approx -H_\varphi^{\text{PEC}}(r, z = 0, \varphi, j\omega) \frac{\sqrt{\mu_0}}{\sqrt{\varepsilon_g + \sigma_g/j\omega}} \quad (2.37)$$

where  $\varepsilon_g$  and  $\sigma_g$  are the permittivity and conductivity of ground. The horizontal electric field at a given height is then obtained by adding the horizontal electric field calculated at

that height assuming the ground to be a perfect conductor to this surface field as [81]

$$E_r(r, z = h, \varphi, j\omega) \approx E_r(r, z = 0, \varphi, j\omega) + E_r^{\text{PEC}}(r, z = h, \varphi, j\omega). \quad (2.38)$$

To improve the accuracy of the CR formulation, a simple modification is suggested in [70]. When calculating  $E_r^{\text{PEC}}$  in (2.38) different weights are given to the static, induction and radiation components as

$$E_r^{\text{PEC}} = E_{r,\text{static}}^{\text{PEC}} + E_{r,\text{induction}}^{\text{PEC}} + 0.4E_{r,\text{radiation}}^{\text{PEC}}. \quad (2.39)$$

Time domain fields can be calculated using the inverse Fourier transform [70]. Vertical electric fields hardly change in the case of lossy ground compared to PEC ground [78]. Therefore, the formulation given in (2.31b) for the vertical electric field above PEC ground can be used for the case of lossy ground as well.

## 2.5 Parallel Implementation of FDTD Algorithms

Distributed transmission line models (such as FDTD) are capable of determining the voltage and current distribution along the line and also are a suitable candidate for modelling nonuniform lines as discussed previously. However, a drawback of FDTD models compared to terminal-based models is that they require more computations per time-step. Therefore, an implementation of the FDTD models using parallel computation will be beneficial. A noteworthy observation on FDTD algorithms based on Fig. 2.4 is that there are no interdependencies within the calculations of a single time-step (*i.e* within a single row in Fig. 2.4). All data required for the calculation of a voltage or current at a particular space seg-

ment, at a particular time-step, are past values of the same segment and the two adjacent segments (see Fig. 2.4). This makes FDTD algorithms easily parallelizable.

The two popular methods of parallel computing currently available are using conventional multi-core central processing units (CPU) and using graphical processing units (GPU) [82]. Existing CPUs can pack only a small number of processor cores on the same die in order to operate within power and thermal constraints [82]. Therefore, the level of parallelism attainable using CPUs is limited to a small number. GPUs, on the other hand, are designed for rendering and other graphics applications [82]. Therefore, they have the capability of executing thousands of threads simultaneously. That being said, a GPU is a separate hardware devices that is initialized and executed by a program running on a CPU [83]. Therefore, there is an additional hardware cost associated with GPUs compared to multi-core CPUs.

High level programming tools are available for parallel programming of CPUs as well as GPUs [84]. The popular standard for CPU parallelization is the message passing interface (MPI) which can be used with programming languages C/C++, Python and Fortran [85]. Various implementations of MPI are available such as OpenMPI, MPICH, MS-MPI, etc. [85]. An MPI based three dimensional parallel FDTD algorithm has been developed in [86] to simulate frequency-independent transmission lines in a cavity excited by an ambient wave. A popular tool for GPU programming is “compute unified device architecture” (CUDA) developed by the GPU manufacturer NVIDIA [84] that is employed in this work. A CUDA-based 2D and 3D FDTD or finite element method (FEM) simulation of electromagnetic problems using parallel computing are proposed in [87,88]. A massive-thread electromagnetic transient (EMT) program (MT-EMTP) based on GPU programming with massive-thread parallel modules for linear passive elements, the universal line model (terminal based T-line model), and the universal machine model has already been developed in CUDA [89].

Efficiency of parallel algorithms are generally determined using ‘speed up factor’ ( $S(p)$ ) which is calculated using [90]

$$S(p) = \frac{\text{Time for serial execution}}{\text{Time for parallel execution.}} \quad (2.40)$$

A linear speed up (*i.e.* program executes  $p$  times faster by using  $p$  processors) might be achievable if the executed program is 100% parallelizable. However, in reality any program will have a portion that has to be executed serially. For example declaration of variables, initialization of processors to be used for parallel operation, etc, has to be executed in series. In addition, depending on the amount of data that has to be transferred among processors the parallel algorithm will introduce a ‘parallel overhead’ to the execution time. Parallel overhead refers to the additional instructions that has to be executed than in a serial algorithm to make the process parallel. Therefore, in practical implementation any program will have a speed up less than a linear speedup.

This is explained in Amdhal’s law which states that if a portion of a program,  $f$ , can be improved by a factor  $p$  ( $p$  can be considered as the number of processors if the portion  $f$  is divided equally among all processors), and the other portion cannot be improved and has to be executed serially, then then the maximum parallel processing speedup ( $S_m(p)$ ) achievable would be [90]

$$S_m(p) = \frac{1}{(1 - f) + \frac{f}{p}}. \quad (2.41)$$

An illustration of Amdhal’s law is given in Fig. 2.9. As seen form Fig. 2.9 as the parallelism of the portion  $f$  increases the speedup drops. This is because the execution time required for the portion  $f$  will reduce when  $p$  increases while the time required for the serial portion  $(1 - f)$  will remain the same. Therefore, as  $p$  increases the contribution from the execution

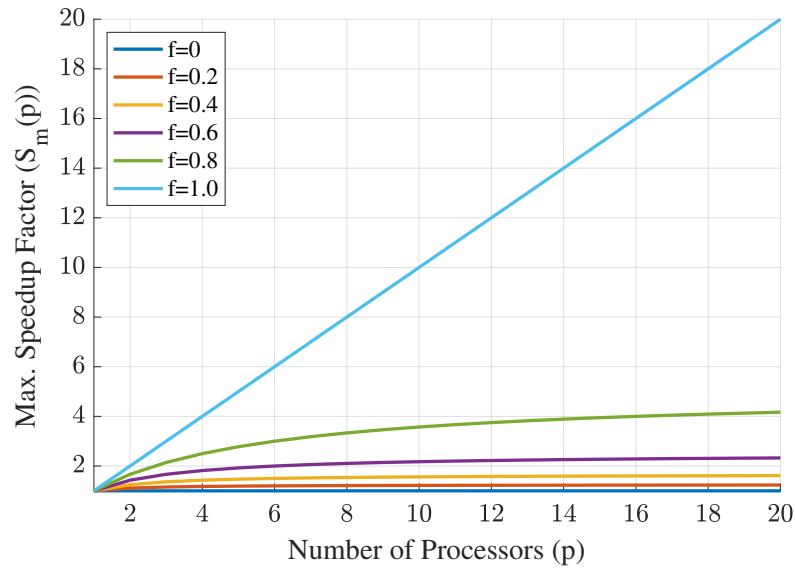


**Fig. 2.9:** Illustration of speedup limit according to Amdhal's law as a function of number of parallel processors ( $p$ ) for different values of parallel portions ( $f$ ).

time of the serial portion to the total execution time will increase. When the execution time of the parallel portion reaches a small value compared to that of the serial portion the speedup will not be improved by further increasing the number of processors.

---

## Chapter 3

# Time-Domain Modelling of Nonuniform Overhead Lines

This chapter proposes a closed-form transmission line model, namely the DSFTL model, based on electromagnetic scattering theory for a lossy, frequency-dependent, nonuniform wire structure over finitely-conducting ground. For clarity the derivation is performed on two single-conductor lines crossing each other. Extension of the single-conductor formulation to multi-conductor cases and other nonuniform structures containing non-parallel wires is then explained. Time-domain implementation of the DSFTL model has been achieved using a modified FDTD algorithm [27] originally introduced for uniform lines which handles the frequency dependency using recursive convolution. The developed model has been implemented in EMTDC/PSCAD (an EMT simulator). The results obtained for transients using the DSFTL model have been compared with those calculated using a commercial full-wave electromagnetic solver. Power frequency results have been compared with field measurements of induced voltages at a power transmission line crossing obtained by other researchers [12].

A case study has also been performed to analyze the effects of typical power line faults and breaker operations on other lines which cross paths with the faulty line.

### 3.1 Dispersive Scattered Field Transmission Line Model for Nonparallel Overhead Wires

Let's consider two single-conductor transmission lines crossing each other at an angle of  $\alpha$  over a finitely-conducting ground, as shown in Fig. 3.1a. The constitutive parameters of the ground are  $\mu_0$ ,  $\varepsilon_g$ , and  $\sigma_g$ , where  $\mu_0$ ,  $\varepsilon_g$  and  $\sigma_g$  are the permeability of free space, permittivity, and conductivity of the ground, respectively. Electromagnetic field distribution of such structures is commonly determined using complex image theory [51] as shown in Fig. 3.1b where

$$p = \frac{1}{\sqrt{j\omega\mu_0(\sigma_g + j\omega\varepsilon_g)}}. \quad (3.1)$$

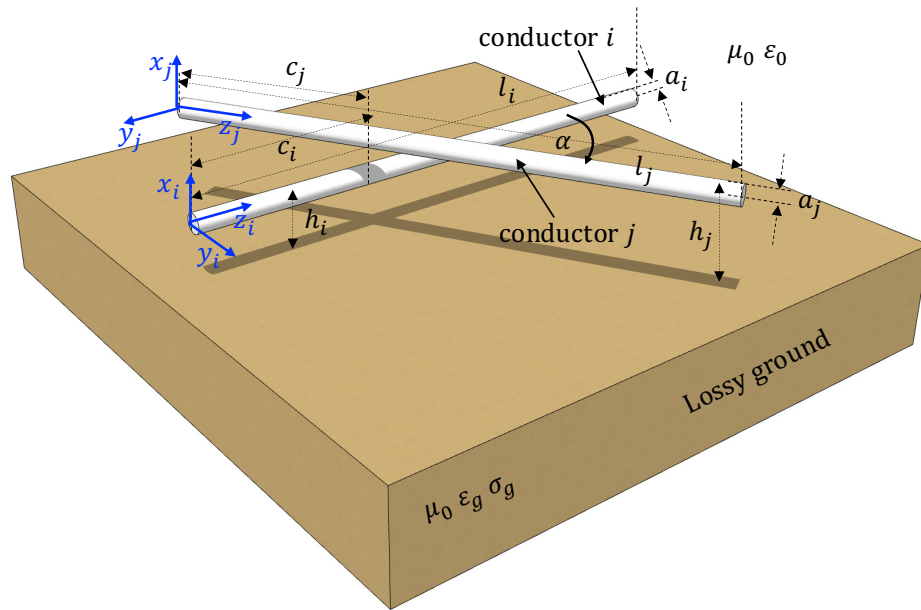
The scattered electric field  $\mathbf{E}^s$  generated by this structure as explained in [25] can be expressed in the frequency-domain as

$$\mathbf{E}^s = -j\omega\mathbf{A} - \nabla\Phi \quad (3.2a)$$

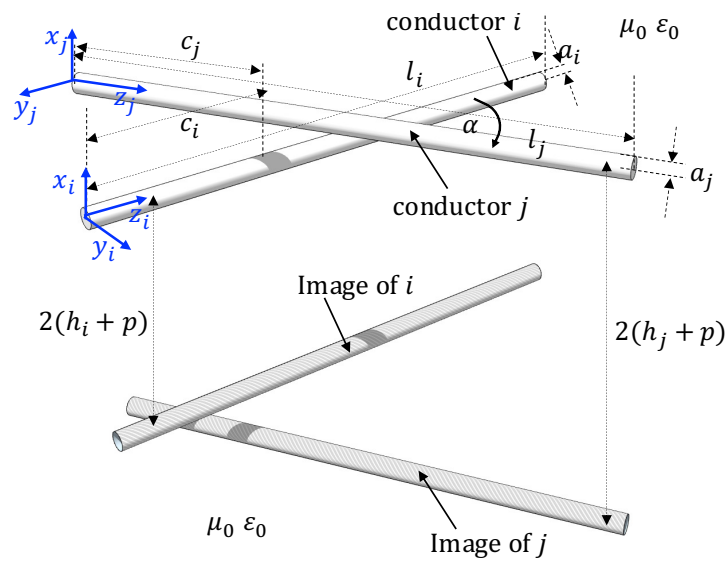
where,  $\mathbf{A}$  and  $\Phi$  are the magnetic vector potential and electric scalar potential, respectively.

For a field point on the conductor  $i$  in the geometry shown in Fig. 3.1

$$A_{z_i}(z_i, j\omega) = \frac{\mu_0}{4\pi} \int_0^{\ell_i} g(z_i, z'_i) I_i(z'_i, j\omega) dz'_i + \cos\alpha \frac{\mu_0}{4\pi} \int_0^{\ell_j} g(z_i, z_j) I_j(z_j, j\omega) dz_j \quad (3.2b)$$



(a)



(b)

**Fig. 3.1:** Single-conductor transmission lines crossing each other above (a) finitely-conducting ground and (b) complex image representation of conductors above ground.

and,

$$\Phi(z_i, j\omega) = \frac{1}{4\pi\epsilon_0} \int_0^{\ell_i} g(z_i, z'_i) \rho_i(z'_i, j\omega) dz'_i + \frac{1}{4\pi\epsilon_0} \int_0^{\ell_j} g(z_i, z_j) \rho_j(z_j, j\omega) dz_j. \quad (3.2c)$$

where  $\alpha$  is the crossing angle,  $\ell_i$  and  $\ell_j$  are the lengths of the conductors,  $I_i$  and  $I_j$  are the currents,  $\rho_i$  and  $\rho_j$  are the electric charge densities at a field point on the surface of the wires  $i$  and  $j$ , and  $\omega$  is the angular frequency, respectively. The Green's function which defines the distribution of the scattered field is given by [39]

$$g(z, z') = \left( \frac{e^{-j\beta R_s}}{R_s} - \frac{e^{-j\beta R_i}}{R_i} \right) \quad (3.3)$$

where  $R_s$  and  $R_i$  are the distances to an observation point  $z$  from the current element and the image current element at a source point  $z'$ , respectively, and  $\beta = \omega\sqrt{\mu_0\epsilon_0}$  is the phase constant. Equation (3.2) looks similar to the scattered electric field of a wire structure above PEC ground given in [29]. However, the Green's functions are quite different from the lossless case since they are now frequency dependent. In [40], it is explained that for lossless structures (*i.e.*, real  $R_s$  and  $R_i$ ), when the maximum cross-sectional dimension of the structure  $h$  is very small compared to the smallest wavelength of interest (*i.e.*,  $h \ll \lambda_{\min}$ ), the exponential terms in (3.3) can be approximated as unity. For finitely-conducting ground,  $R_i$  in (3.3) is frequency-dependent and complex.

The variation of  $e^{-j\beta R_i}$  in the Green's function  $g(z_i, z'_i)$  under different ground resistivities as a function of frequency is shown in Fig. 3.2 for two heights ( $h = 10$  and  $30$  m). It can be seen that  $e^{-j\beta R_i}$  for a lossy ground can also be approximated as 1 upto a certain frequency which depends on the cross-sectional dimensions and resistivity of the ground. For example, for a 10 m high line above a ground with a resistivity of  $100 \Omega\text{m}$  this approximation is valid

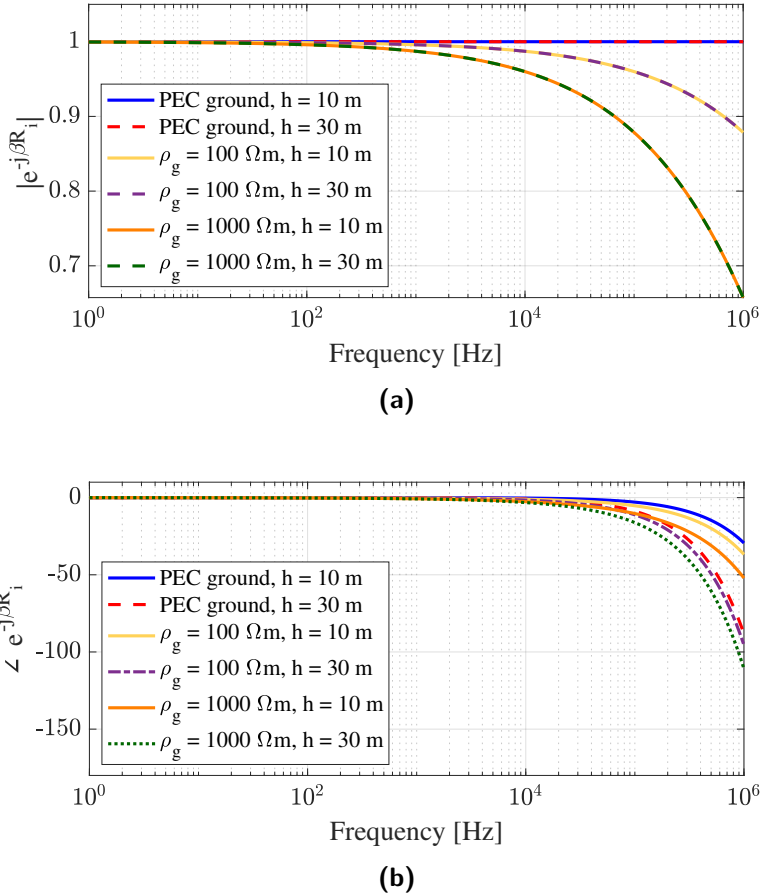


**Fig. 3.2:** (a) Magnitude and (b) phase of  $g(z_i, z'_i)$  vs frequency.

up to around 100 kHz and so would be the proposed model for such a line. Also, for typical power line frequencies since  $\sigma_g \gg \omega \epsilon_g$ , the complex depth  $p$  in (3.1) can be approximated as

$$p \approx \frac{1}{\sqrt{j\omega\mu_0\sigma_g}}. \quad (3.4)$$

Assuming the exponential terms are approximately equal to 1 and  $h \ll \lambda_{\min}$ , closed-form

expression can be obtained for the integral terms of (3.2) as

$$\begin{aligned} \int_0^\ell \left( \frac{e^{-j\beta R_s}}{R_s} - \frac{e^{-j\beta R_i}}{R_i} \right) I(z', j\omega) dz' &= \int_0^\ell \left( \frac{1}{R_s} - \frac{1}{R_i} \right) dz' I(z, j\omega) \\ &= \xi(z, j\omega) I(z, j\omega) \end{aligned} \quad (3.5)$$

where  $\xi$  is the analytical solution for the integral term. This result is important as it eliminates the need of performing a numerical integration at each time step of the upcoming time-domain implementation. Assuming a transverse field structure and a thin-wire geometry, (3.2) can be rearranged into two closed-form transmission-line-like equations as explained in [29] as

$$\frac{dV(z_i, j\omega)}{dz_i} = -Z_c I(z_i, j\omega) - \frac{j\omega\mu_0}{4\pi} \left[ \xi_{ii}'(z_i, j\omega) I_i(z_i, j\omega) + \cos\alpha \xi_{ij}'(z_i, j\omega) I_j(z_j, j\omega) \right] \quad (3.6a)$$

and,

$$V(z_i, j\omega) = -\frac{1}{j\omega 4\pi\epsilon_0} \left[ \xi_{ii}'(z_i) \frac{dI_i(z_i, j\omega)}{dz_i} + \xi_{ij}'(z_i) \frac{dI_j(z_j, j\omega)}{dz_j} \right]. \quad (3.6b)$$

Closed-form expressions for the integral terms are represented using  $\xi$  in (3.6) which are explained further in (3.7).

$$\begin{aligned} \xi_{ii} &= \ln \left( \ell_i + \sqrt{(\ell_i - z_i)^2 + a_i^2} - z_i \right) - \ln \left( \sqrt{(\ell_i - z_i)^2 + a_i^2} - z_i \right) \\ &\quad - \ln \left( \ell_i + \sqrt{(\ell_i - z_i)^2 + (2h_i + 2p)^2} - z_i \right) + \ln \left( \sqrt{(\ell_i - z_i)^2 + (2h_i + 2p)^2} - z_i \right) \end{aligned} \quad (3.7a)$$

and,

$\xi_{ij} =$

$$\begin{aligned}
& \ln \left( \ell_j + \sqrt{[(\ell_j - c_j) + (z_i - c_i) \cos \alpha]^2 + [(z_i - c_i) \sin \alpha]^2 + (h_i - h_j)^2} - c_j + (z_i - c_i) \cos \alpha \right) \\
& - \ln \left( \sqrt{[(\ell_j - c_j) + (z_i - c_i) \cos \alpha]^2 + [(z_i - c_i) \sin \alpha]^2 + (h_i - h_j)^2} - c_j + (z_i - c_i) \cos \alpha \right) \\
& + \ln \left( \ell_j + \sqrt{[\ell_j - c_j + (z_i - c_i) \cos \alpha]^2 + [(z_i - c_i) \sin \alpha]^2 + H^2} - c_j + (z_i - c_i) \cos \alpha \right) \\
& + \ln \left( \sqrt{[(\ell_j - c_j) + (z_i - c_i) \cos \alpha]^2 + [(z_i - c_i) \sin \alpha]^2 + H^2} - c_j + (z_i - c_i) \cos \alpha \right)
\end{aligned} \tag{3.7b}$$

where

$$H = h_i + h_j + 2p$$

$Z_c$  is the conductor resistive loss including skin effect. Since capacitance is considered to be frequency independent in overhead lines [25] and the conductance of air is negligible,  $\xi'$  terms in the current equation (3.6b) can be assumed to be those of a frequency-independent line given by [29].

$$\xi'_{ii} = \sinh^{-1} \left( \frac{\ell_i - z_i}{a_i} \right) - \sinh^{-1} \left( \frac{-z_i}{a_i} \right) - \sinh^{-1} \left( \frac{\ell_i - z_i}{2h_i} \right) + \sinh^{-1} \left( \frac{-z_i}{2h_i} \right) \tag{3.8a}$$

$$\begin{aligned}
 \xi'_{ij} = & \sinh^{-1} \left( \frac{\ell_j - c_j + (c_i - z_i) \cos \alpha}{\sqrt{((c_i - z_i) \sin(\alpha))^2 + (h_i - h_j)^2}} \right) \\
 & - \sinh^{-1} \left( \frac{-c_j + (c_i - z_i) \cos \alpha}{\sqrt{((c_i - z_i) \sin(\alpha))^2 + (h_i - h_j)^2}} \right) \\
 & - \sinh^{-1} \left( \frac{\ell_j - c_j + (c_i - z_i) \cos \alpha}{\sqrt{((c_i - z_i) \sin(\alpha))^2 + (h_i + h_j)^2}} \right) \\
 & + \sinh^{-1} \left( \frac{-c_j + (c_i - z_i) \cos \alpha}{\sqrt{((c_i - z_i) \sin(\alpha))^2 + (h_i + h_j)^2}} \right)
 \end{aligned} \tag{3.8b}$$

Similar equations can be derived for the other conductor ( $j$ ) and the system of equations can be rearranged into the classical transmission line format of as

$$\frac{d}{dz} \begin{bmatrix} \mathbf{V}(z, j\omega) \\ \mathbf{I}(z, j\omega) \end{bmatrix} = - \begin{bmatrix} 0 & \mathbf{Z}(z, j\omega) \\ \mathbf{Y}(z, j\omega) & 0 \end{bmatrix} \begin{bmatrix} \mathbf{V}(z, j\omega) \\ \mathbf{I}(z, j\omega) \end{bmatrix} \tag{3.9a}$$

where

$$\mathbf{Z}(z, j\omega) = \begin{bmatrix} Z_c + \frac{j\omega\mu_0}{4\pi} \xi_{ii}(z, j\omega) & \frac{j\omega\mu_0 \cos(\alpha)}{4\pi} \xi_{ij}(z, j\omega) \\ \frac{j\omega\mu_0 \cos(\alpha)}{4\pi} \xi_{ij}(z, j\omega) & Z_c + \frac{j\omega\mu_0}{4\pi} \xi_{jj}(z, j\omega) \end{bmatrix} \tag{3.9b}$$

and

$$\mathbf{Y}(z, j\omega) = 4\pi\epsilon_0 j\omega \begin{bmatrix} \xi'_{ii}(z) & \xi'_{ij}(z) \\ \xi'_{ji}(z) & \xi'_{jj}(z) \end{bmatrix}^{-1}. \tag{3.9c}$$

This concept can be conveniently extended into multi-conductor lines and other nonuniform geometries such as bends as explained in [42]. When multi-conductor lines cross each other coupling from each individual conductor should be considered. If a transmission line  $i$

consisting of  $N$  conductors crosses with another line  $j$  consisting of  $M$  conductors, the magnetic vector potential and scalar potential of a conductor in line  $i$  can be calculated using

$$\mathbf{A}_{z_i}(z_i) = \frac{\mu}{4\pi} \left\{ \sum_{k=1}^N \left[ \int_0^{\ell_i} g(z_i, z_i') I_k(z_i') dz_i' \right] + \cos \alpha \sum_{k=N+1}^{N+M} \left[ \int_0^{\ell_j} g(z_i, z_j, \alpha) I_k(z_j) dz_j \right] \right\} \quad (3.10a)$$

and,

$$\Phi(z_i) = \frac{1}{4\pi\epsilon} \left\{ \sum_{k=1}^N \left[ \int_0^{\ell_i} g(z_i, z_i') \rho_k(z_i') dz_i' \right] + \sum_{k=N+1}^{N+M} \left[ \int_0^{\ell_j} g(z_i, z_j, \alpha) \rho_k(z_j) dz_j \right] \right\}. \quad (3.10b)$$

Rest of the derivation is identical to the single conductor case.

## 3.2 Time-Domain Implementation

When (3.9) is converted into time-domain, multiplications between frequency dependent terms get converted into convolutions. Therefore time-domain implementation is not as straight forward as for lossless lines in [29]. A method to solve single-conductor uniform dispersive transmission lines has been introduced in [27] and explained in Section 2.3 which is extended to non-uniform multi-conductor structures in this work. Consider the series impedance matrix ( $\mathbf{Z}(z, j\omega)$ ) of one of the space segments ( $z$ ). It can be fitted into a matrix function of the format

$$\mathbf{Z}(z, j\omega) = \mathbf{R}(z) + j\omega\mathbf{L}(z) + \mathbf{Z}'(z, j\omega) \quad (3.11a)$$

where

$$\mathbf{Z}'(z, j\omega) = \sum_{k=1}^M \frac{\mathbf{a}_{z,k}}{j\omega - \alpha_{z,k}}. \quad (3.11b)$$

In (3.11)  $\mathbf{a}_{z,k}$  is the residue matrix corresponding to each pole  $\alpha_{z,k}$ . Note that the set of poles has to be common for all elements of  $\mathbf{a}_{z,k}$ . In contrast to uniform MTL systems which involves a fitted function for all space segments, a nonuniform system will require unique fitted functions for each space segment in the FDTD algorithm. Substituting (3.9) with fitted PUL impedance and converting it to time-domain gives

$$\frac{\partial}{\partial z} \mathbf{V}(z, t) = -\mathbf{R}(z) \mathbf{I}(z, t) - \mathbf{L}(z) \frac{\partial}{\partial t} \mathbf{I}(z, t) - \mathbf{Z}'(z, t) * \mathbf{I}(z, t) \quad (3.12a)$$

and

$$\frac{\partial}{\partial z} \mathbf{I}(z, t) = -\mathbf{C} \frac{\partial}{\partial t} \mathbf{V}(z, t). \quad (3.12b)$$

Equations in (3.12) are solved using the modified finite-difference time-domain (MFDTD) algorithm introduced in [27]. The proposed model is implemented in a commercial power system EMT simulator (EMTDC/PSCAD) and the ability to simulate non-uniform structures along with other power system elements including non-linear elements is demonstrated in the results section.

### 3.3 Implementation of DSFTL on PSCAD/EMTDC

When modelling a power network which consists of transmission lines that cross each other, the components of the network other than the area of crossing can be modelled as in a typical simulation using inbuilt components. To simulate the field coupling in the crossing area, MFDTD algorithm of the DSFTL model is introduced as an external component to update a set of dependent current sources ( $I_{SHi}$  and  $I_{LHi}$ ) in the PSCAD model as shown in Fig.

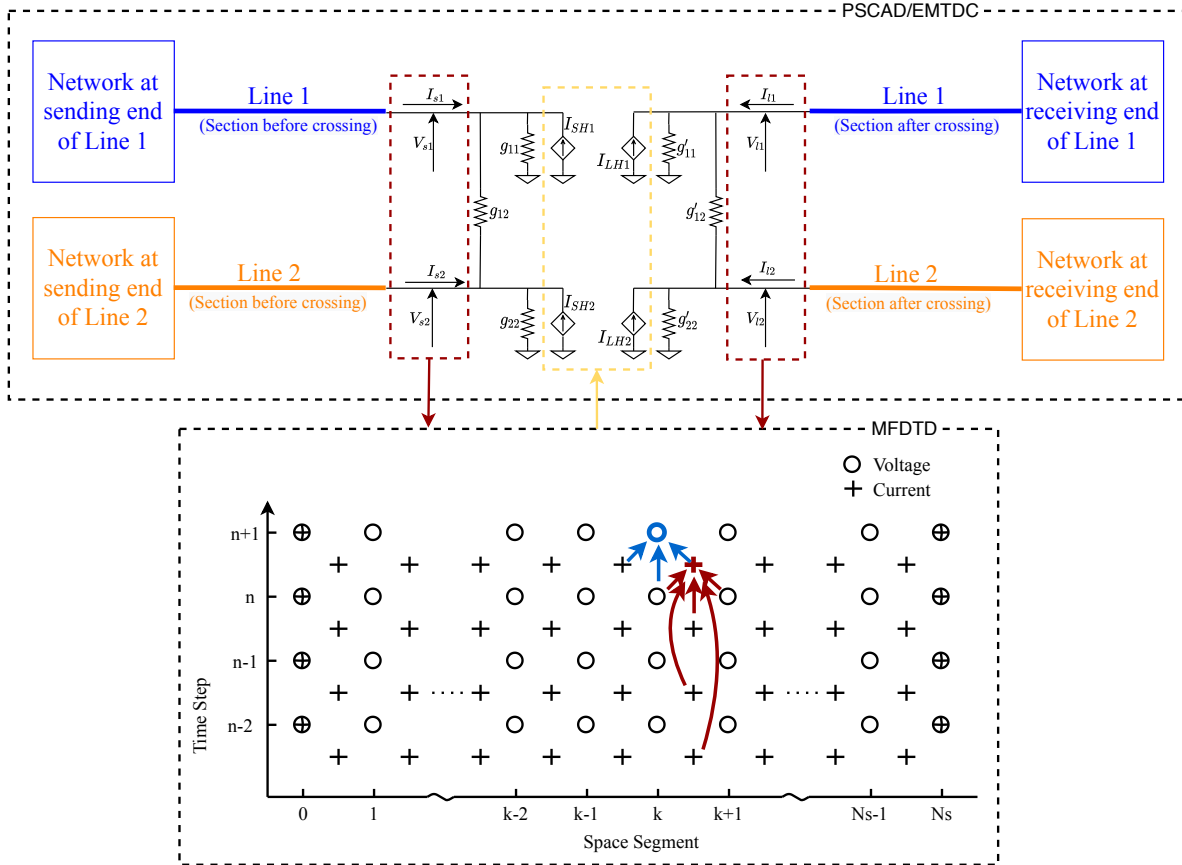


Fig. 3.3: Illustration of the implementation of DSFTL model on PSCAD/EMTDC.

3.3. At each time-step the MFTD algorithm will accept voltage and current measurements ( $V_{si}, V_{li}, I_{si}$  and  $I_{li}$ ) from the PSCAD model, solve the finite-difference problem and update the dependent current sources. In order to avoid any false reflections at the DSFTL-EMT interface, the PUL parameters of the bordering space segments of the DSFTL model should be equal to those of the corresponding transmission line components of the EMT simulator. Also, the mutual coupling between the two lines should be negligible at the bordering space segments of the DSFTL model.

## 3.4 Results and Discussion

Results obtained using the DSFTL model for two single conductor transmission lines crossing at an angle of  $\alpha$  are compared against those obtained from a commercial thin-wire full-wave solver, Numerical Electromagnetic Code (NEC4). Induced voltages at power-frequency on an AC transmission line crossing under a UHV AC line are also compared with measurements obtained by other researchers. A case study on the effect from power system fault currents on nearby lines is also presented.

### 3.4.1 Verification of the DSFTL model using a full-wave solver

Two conductors crossing each other at a variable angle  $\alpha$  are modelled. The dimensions of the lines (see Fig. 3.1) are  $\ell_1 = \ell_2 = 10$  km,  $c_1 = c_2 = 4$  km,  $h_1 = 10$  m,  $h_2 = 12$  m, and  $a_1 = a_2 = 20$  mm. Ground resistivity is taken as  $100 \Omega\text{m}$ . A derivative of a Gaussian pulse with a full-width at half maximum (FWHM) of 22 kHz as shown in Fig. 3.4 is used to excite conductor 1 at the sending end. An excitation which does not contain a DC component is purposely used here since the full-wave solver (NEC4) used to generate reference waveforms doesn't compute DC response [91]. All terminals of the transmission line structure are connected to  $100 \Omega$  resistive loads. Since NEC4 is a frequency-domain solver, FFT-IFFT method is used to obtain time-domain results. It is worth noting that the DSFTL method, being inherently a time-domain method, does not have the limitation of approaches that employ the FFT-IFFT methods.

The current waveform generated in the excited conductor is shown in Fig. 3.5 and the current induced in the victim conductor for different crossing angles are shown in Fig. 3.6 compared with those obtained using NEC4. It can be seen that the DSFTL model has been

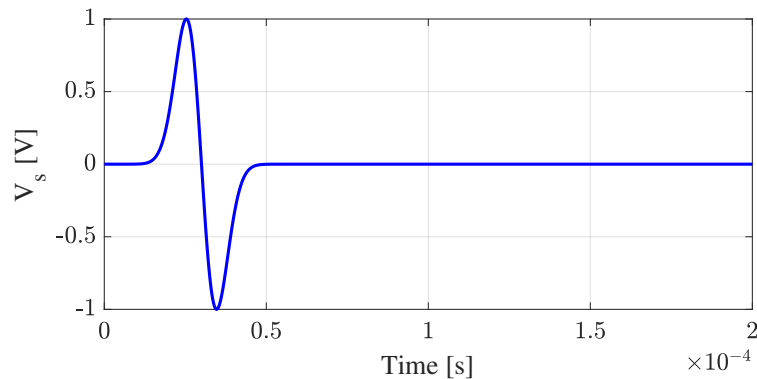


**Fig. 3.4:** Derivative of a Gaussian waveform applied on conductor  $i$ .

able to produce the same results as the full-wave technique. Current waveforms under a lossless approximation [29] is plotted in the same figure to demonstrate the wave distortion occurring due to frequency-dependent losses.

Figure 3.6 also suggests that when the crossing angle increases the magnitude of the induced current on the victim conductor decreases. It is interesting to see that even at an orthogonal crossing (*i.e.*  $\alpha = 90^\circ$ ), a current is still induced in the victim line. This is because when the crossing angle is  $90^\circ$ , even though the mutual inductive coupling in (3.9b) becomes zero, the mutual capacitive coupling in (3.9c) still remains. Computer memory requirement for a full-wave simulation of this geometry is a few giga-bytes (GB), whereas the same of the DSFTL model is in the order of a few Mega-bytes (MB).

### 3.4.2 Verification of the DSFTL model using power frequency measurements

In [12], field measurement data is provided for induced voltage on a 110 kV HVAC line passing under a double circuit 1000 kV UHVAC line at a crossing angle of  $60^\circ$ . Conductor

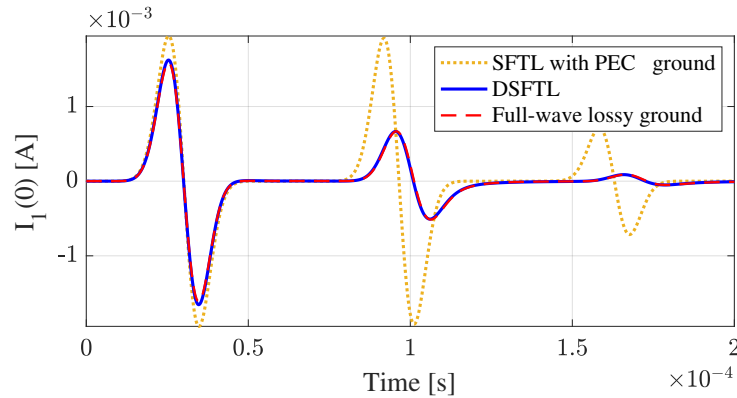


**Fig. 3.5:** Current generated at the sending end in the excited conductor.

arrangements on the two lines are shown in Fig. 3.7. The two circuits of the UHVAC line are supplying loads of 275 MW, 416 MVar and 271 MW, 21 MVar respectively. Field measurements from [12] of the induced voltage on the victim line at the point of crossing when its terminals are ungrounded and grounded are given in Tables 3.1 and 3.2, respectively.

The same structure is modelled using the DSFTL in PSCAD/EMTDC with similar energization and loading. Lines are modelled up to 1 km along each direction from the crossing to be consistent with [12]. The following parameters have to be assumed as they are not mentioned in [12]. Conductor radius is assumed to be 20 mm [92]. Power frequency and ground resistivity are assumed as 50 Hz and 100  $\Omega\text{m}$  based on the location where field measurements were obtained [93]. When obtaining voltages on a grounded line, grounding impedance is a key factor. Since no information on the value of the grounding resistance is provided in [12], grounding resistance values in the range of 1 - 25  $\Omega$ , as recommended in [94], as well as higher values of 35 and 50  $\Omega$  are used to simulate the grounded LV case. For the MFDTD calculation in the DSFTL model a time step of 0.5  $\mu\text{s}$  and a corresponding space step of 153.85 m is used.

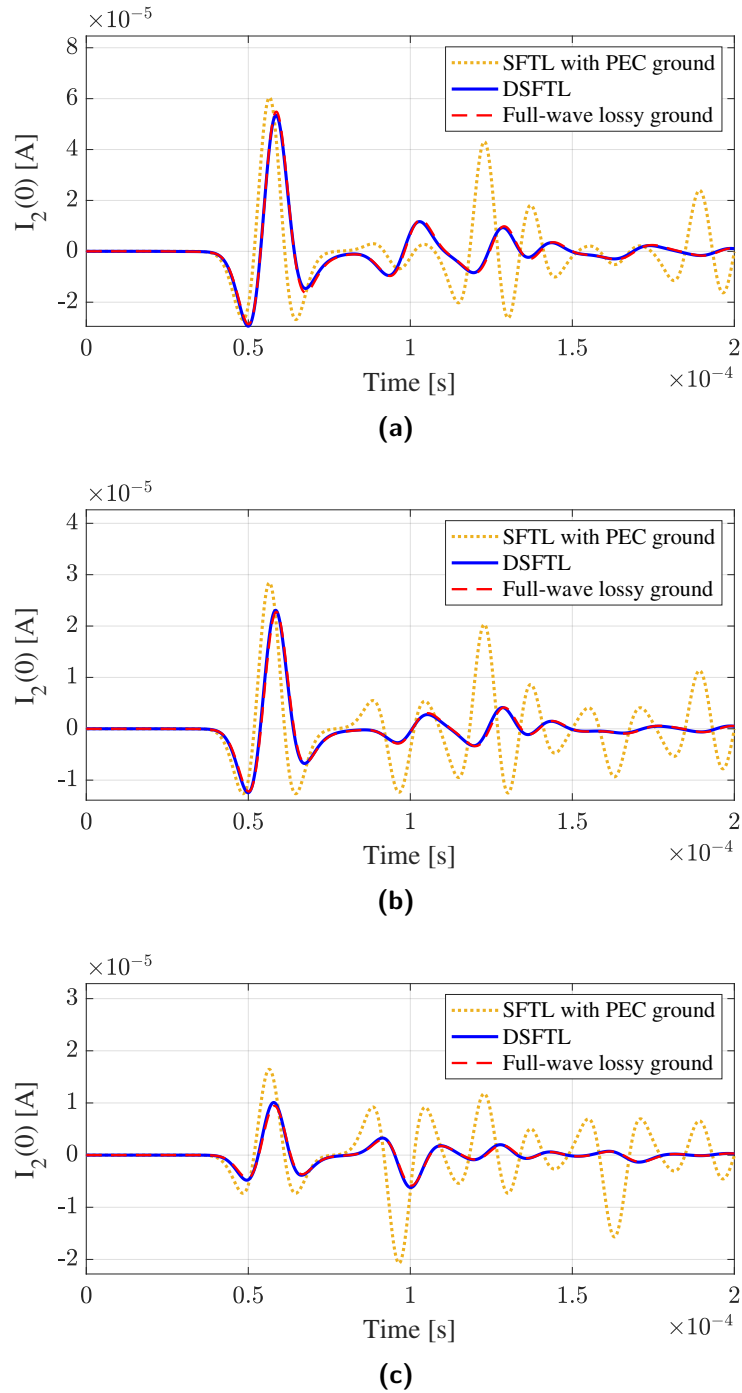


**Fig. 3.6:** Sending end current on the victim conductor for crossing angles of (a)  $30^\circ$  (b)  $60^\circ$  and (c)  $90^\circ$ .

**Table 3.1:** Measurement data from [12] and simulated results using DSFTL model of induced voltages (peak) on the ungrounded LV line when the HV line is energized with a 50 Hz voltage of 816.5 kV (peak).

Phase	Measured Voltage (V)	Simulated Voltage (V)	% Difference
1	17.45	17.00	2.6
2	14.91	14.04	5.8
3	12.49	11.50	7.9

**Table 3.2:** Measurement data from [12] and simulated results using DSFTL model of induced voltages (peak) on the grounded LV line when the HV line is energized with a 50 Hz voltage of 816.5 kV (peak).

Phase	Measured Voltage (V)	Simulated Voltage (V) for different $Z_g$					
		1 $\Omega$	5 $\Omega$	10 $\Omega$	25 $\Omega$	35 $\Omega$	50 $\Omega$
1	3.3	1.6	2.0	2.2	2.6	2.9	3.3
2	3.1	1.5	1.8	1.9	2.2	2.3	2.6
3	3.1	1.3	1.6	1.7	1.9	2.1	2.2

Voltage waveforms at the point of crossing on the energized line and the victim line under the grounded and ungrounded conditions are shown in Fig. 3.8, and their peak values are presented in Tables 3.1 and 3.2, respectively. By comparing measured and simulated voltage values given in Table 3.1, it can be seen that for the case where the LV line is ungrounded the voltage values match closely. For the case of grounded LV line (see Table 3.2) the induced voltages are very small in magnitude (below 5 V) and are seen to be in the same order. By aforementioned comparisons with results from full-wave techniques and field

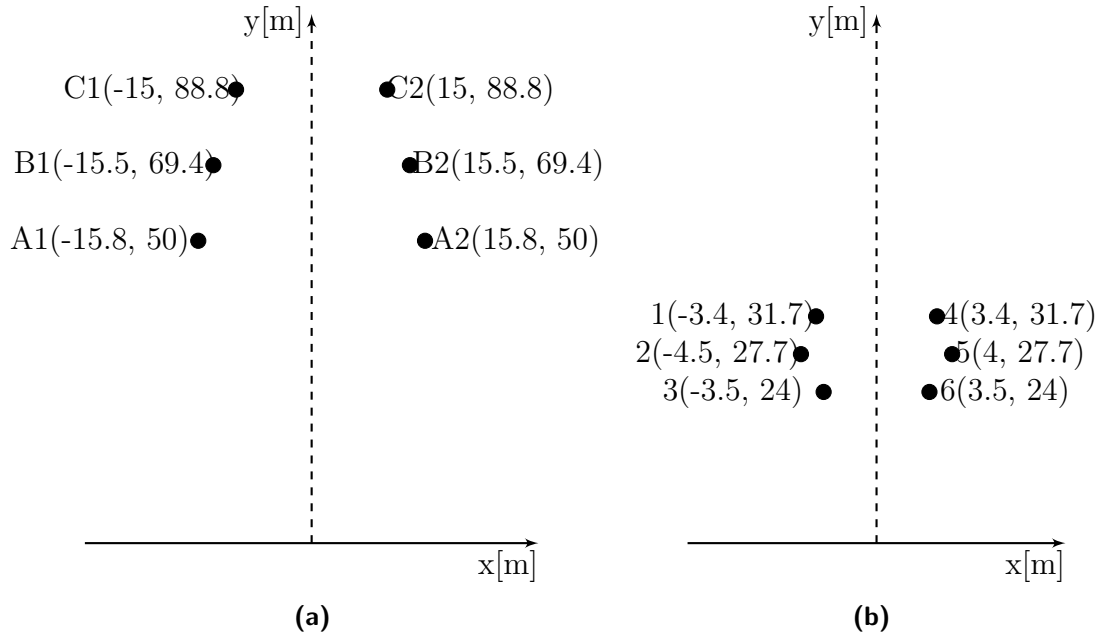


**Fig. 3.7:** Conductor arrangements of (a) 1000 kV UHVAC line and (b) 110 kV HVAC line [12].

measurement data both the transient and power-frequency performance of DSFTL method have been demonstrated.

### 3.4.3 Case study on the effect of faults on nearby lines

A case study is performed to analyze the transient behavior of the lower voltage line due to a fault in the high voltage line simulated in Section 3.4.2. The schematic of the simulated circuit is shown in Fig. 3.9. From an EMT simulator perspective, the simulation model consists of three cascaded multiport networks of which the middle one is the DSFTL model for the region of the crossing and the other two are conventional models for the rest of the transmission line. A fault can be applied at any terminal of the multiport networks. Faults

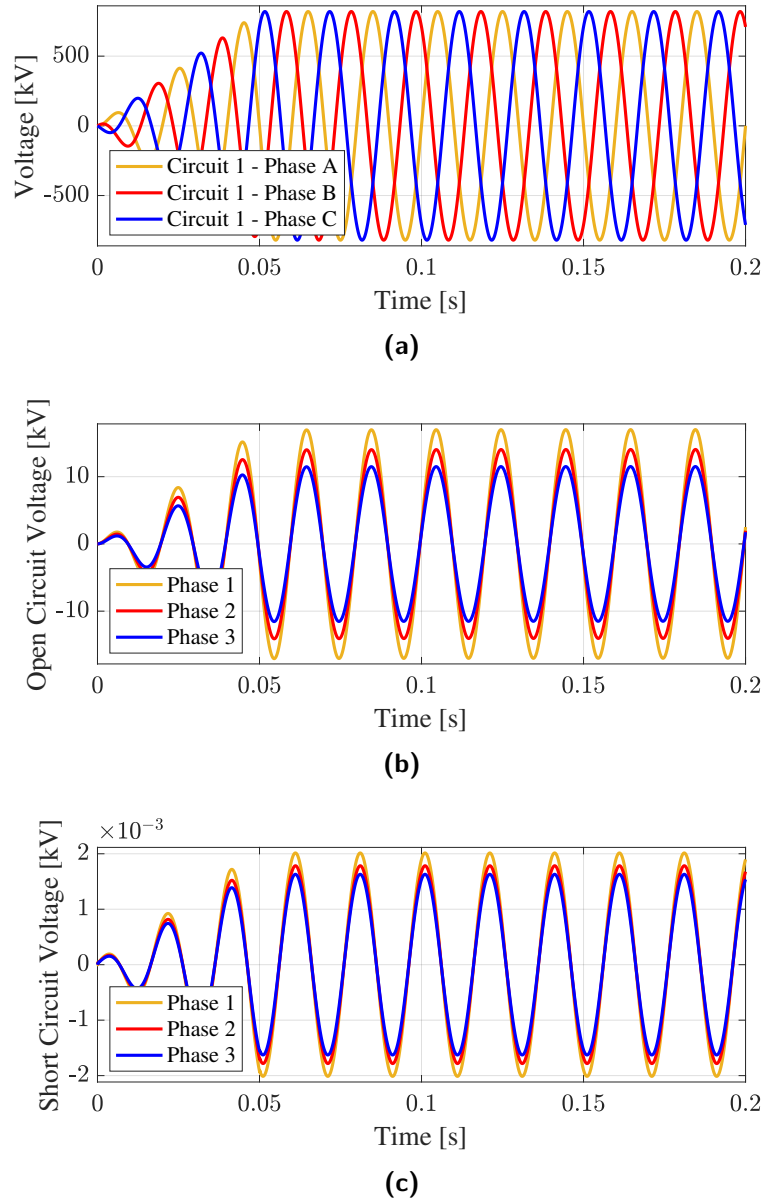


**Fig. 3.8:** Voltage waveforms at the crossing points of (a) energized 1000 kV line (b) 110 kV line with ungrounded ends and (c) 110 kV line with grounded ends obtained using DSFTL model on PSCAD/EMTDC.

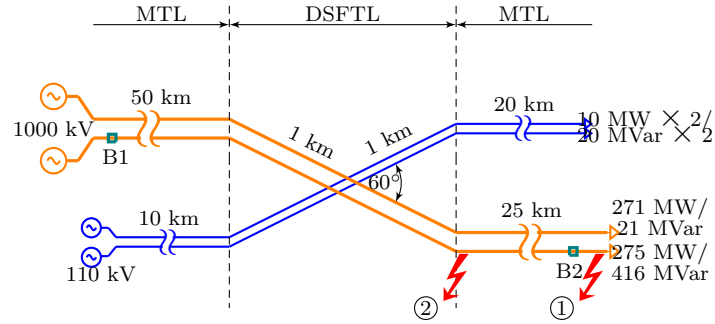


**Fig. 3.9:** Schematic of double circuit 1000 kV and 110 kV transmission lines along with locations where faults were applied.

are created at the farthest (location ①) and closest (location ②) nodes to the point of crossing towards the load side on one of the circuits in the UHV AC line as shown in Fig. 3.9. However, a fault can be applied at any arbitrary location on the transmission line as long as it is divided into cascaded multiport network sections and the fault is applied to the terminal of the multiport network. Loads connected to the 1000 kV line is kept the same as in Section 3.4.2 and the induced voltage in the 110 kV is analysed under both energized and grounded conditions.

First, transient behavior of the energized 110 kV line is studied when a three phase (L-L-L) fault occurs in one of the circuits of the 1000 kV line at the load end (location ① in Fig. 3.9). Voltage drop in the faulty phases is given a fall-time of  $250 \mu\text{s}$  in accordance with the standard switching impulse waveform [95]. Each fault is followed by a breaker operation at locations B1 or B2 triggered by an over-current relay to isolate the fault. Voltage waveforms on both lines at the point of crossing are shown in Fig. 3.10. As evident from the figure, the disturbance in the 1000 kV line does not create a significant interference in the 110 kV line. Faults occurring at other locations shown in Fig. 3.9 produced similar results. Therefore it can be concluded that the set clearances between lines in this case study are sufficient to

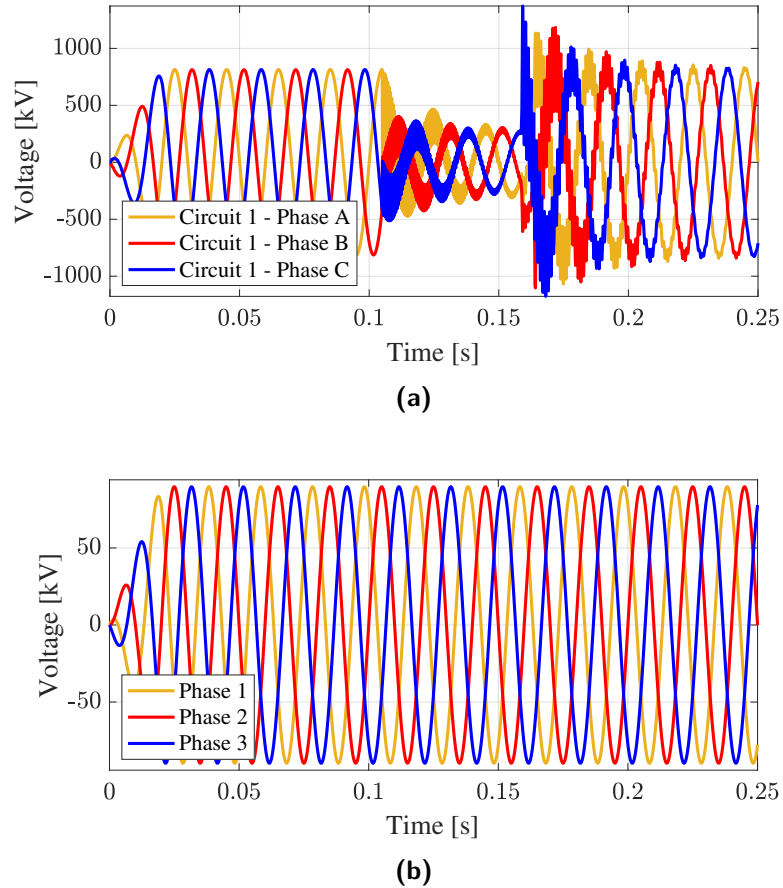


**Fig. 3.10:** Voltage waveforms at the point of crossing on (a) energized 1000 kV line having a 3-phase fault and (b) energized 110 kV line obtained using DSFTL model on PSCAD/EMTDC.

avoid interference under normal operation.

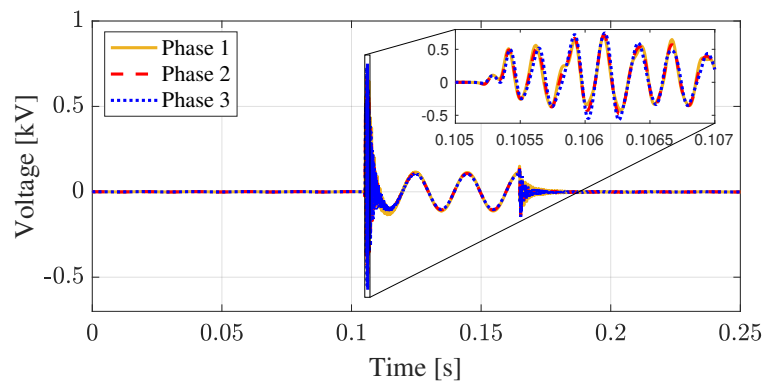
Next, a situation where a fault occurs in the 1000 kV line while the 110 kV line is grounded, simulating the line maintenance procedure, is studied. The voltage induced in the point of crossing under different fault configurations is shown in Fig. 3.11. Before the occurrence of a fault, the induced voltage in the 110 kV line is around 2 ~ 3 V. However, when a fault occurs at the load end of the energized line a transient of around 1 kV is

generated in the grounded line. The power-frequency induced voltage which follows is also much higher than the safe voltage for humans according to [96] which states that voltages as low as 50 V can cause fibrillation. If a failure happens in the protection system of the 1000 kV line, this voltage will remain until the fault is cleared. When the fault happens closer to the crossing the induced voltages are higher as shown in Fig. 3.11b. When a three-phase fault occurs at the load end the induced voltage as shown in Fig. 3.11c is much less than that induced during an unbalanced fault.

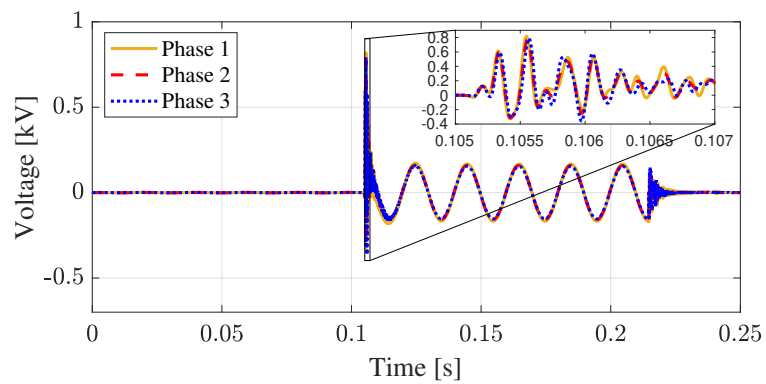
Magnitude of the transients in the victim line is proportional to the rate of change of the original transients in the energized (faulty) line. Therefore, the magnitude of the initial high-frequency transient is highly dependent on the fall-time of the voltage in the faulty line. Results shown in Fig. 3.11 are for a fall-time of  $250 \mu s$  in accordance with the standard switching waveform. Faster fall-times can produce transients with higher magnitudes in the victim line. The magnitude of the power-frequency transient, which is induced during the time between the occurrence of the fault and the operation of the breaker, is not expected to change with the fall-time of the fault and is contributed mainly by the unbalance between phases in the faulty line which remains until breakers operate. This explains why the magnitude of the transients during a L-G fault is much larger compared to that of a L-L-L fault.

#### **3.4.4 DSFTL for modelling bent conductors**

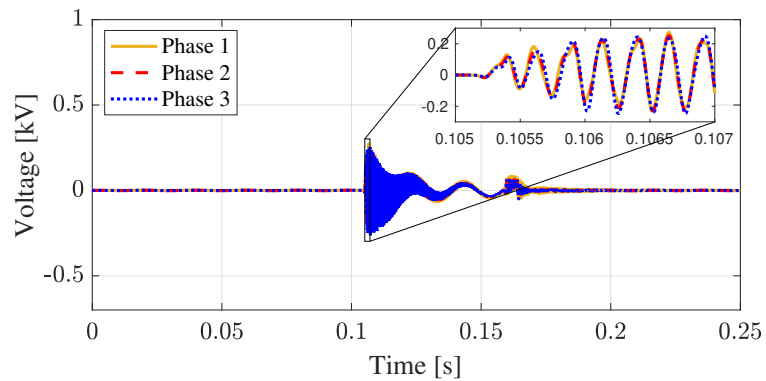
A time-domain analysis has been performed on a three-conductor transmission line having two orthogonal bends in close proximity as shown in Fig. 3.12. The dimensions are obtained from [97] for a typical 230 kV line where the line clearance to ground is assumed to be 10 m, the gap between conductors to be 3 m, and the radius of conductors to be 20 mm. The bends



(a)



(b)



(c)

**Fig. 3.11:** Voltage waveforms at the crossing point of the grounded 110 kV line when the 1000 kV line undergoes a (a) L-G fault at load end (location ①) cleared by breaker B2, (b) L-G fault at location ② cleared by breaker B1, and (c) L-L-L fault at load end cleared by breaker B2 obtained using DSFTL model incorporated in PSCAD/EMTDC.

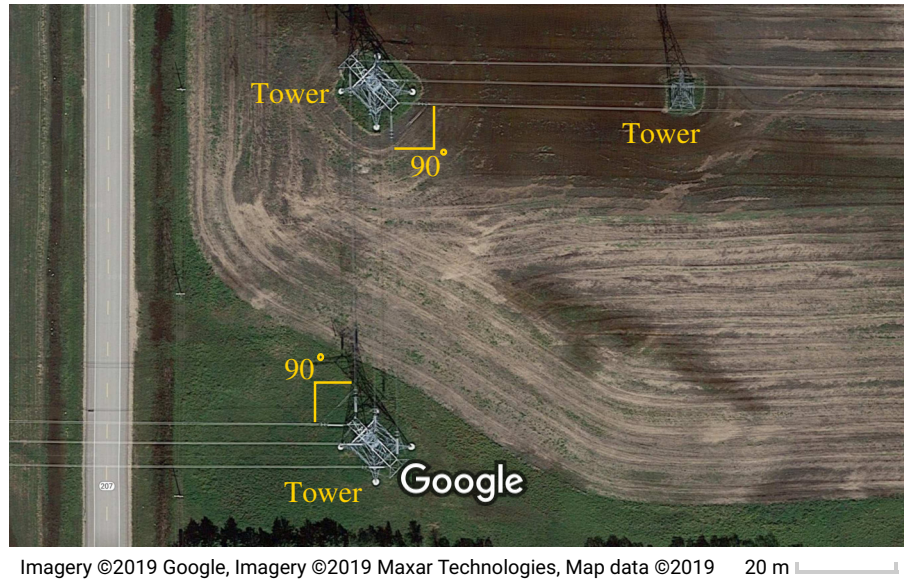


**Fig. 3.12:** A transmission line bend near Riel converter station, Winnipeg, Manitoba, Canada.

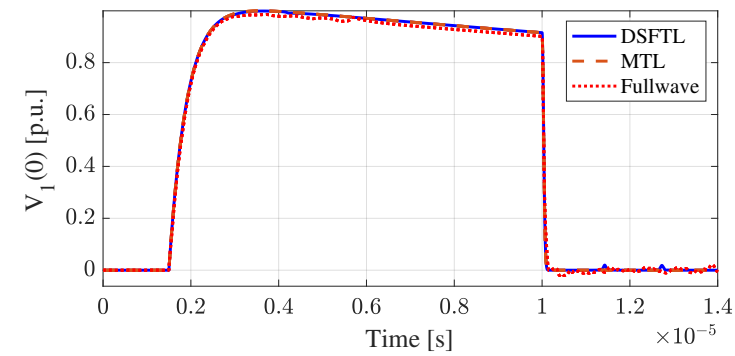
are assumed to be 200 m apart. A standard  $1.2/50 \mu\text{s}$  lightning impulse chopped after  $5 \mu\text{s}$  with a chopping time of  $0.1 \mu\text{s}$  is injected at a distance of 200 m prior to the first bend. Since the modelled line segments are shorter than 1 km, the ground is assumed to be PEC [80].

Figure 3.13 shows the recorded sending end voltages using the SFITL model, a classical MTL model which assumes the line has a uniform cross-section throughout its span and a commercial full-wave solver (COMSOL multiphysics). As the figure depicts, MTL is unable to simulate the voltage spikes which are generated due to the bend and propagate backwards along the line while the proposed DSFITL model has been able to simulate them in close agreement with full-wave results. It should also be mentioned that the reflections occurring at the bend are less significant in magnitude compared to the original transient. Therefore, classical MTL model can be considered to be providing a satisfactory representation. However, in the event of faster transients occurring in power systems, DSFITL will provide a

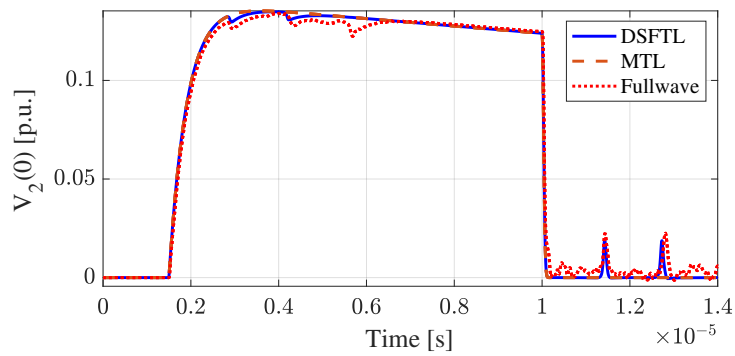
better representation of the wave propagation.

## 3.5 Summary

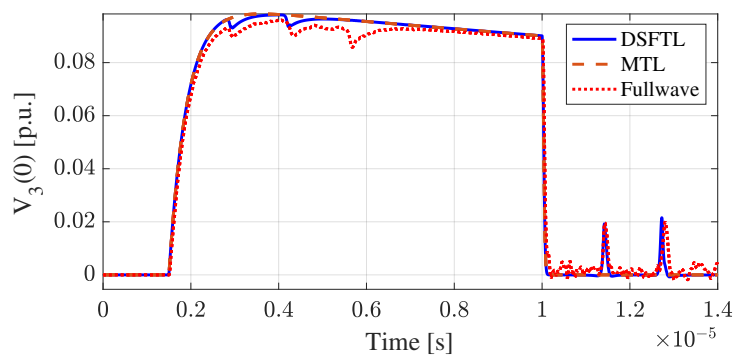
This chapter proposed an approach, namely dispersive scattered field transmission line (DSFTL) model, to simulate nonuniformities, such as crossing, in frequency-dependent transmission lines above lossy, frequency-dependent ground. The initial mathematical model was developed using electromagnetic scattering equations under the thin-wire approximation. Then it was simplified into a transmission-line-like form considering the geometrical characteristics and frequencies of interest in typical power transmission lines. Resulting nonuniform transmission line equations were solved using a modified FDTD algorithm. The proposed model was successfully implemented in a power system EMT simulator and used to model a real world scenario of two transmission lines crossing each other. The accuracy of the transient waveforms obtained using the DSFTL model were verified with those calculated using a commercial full-wave electromagnetic solver. The comparison demonstrated that DSFTL can correctly model the transient behavior at a transmission line crossing. The DSFTL model was also able to regenerate power-frequency measurements of induced voltages obtained by other researchers. A case study on induced transients on power lines passing under faulty higher voltage lines was also performed with non-linear and time-dependent elements included in the circuit. Based on these results, it is advisable to use temporary grounding during maintenance of such structures. It can be concluded that this work demonstrates the capabilities of DSFTL model as a suitable candidate for a nonuniform frequency-dependent transmission line model for power system EMT simulators.



(a)



(b)



(c)

**Fig. 3.13:** Sending end voltages (normalized to the excited conductor) of the (a) excited conductor and (b) and (c) victim conductors for an excitation of a standard  $1.2/50 \mu\text{s}$  lightning impulse chopped after  $5 \mu\text{s}$  with a chopping time of  $0.1 \mu\text{s}$  obtained using SFTL model and classical MTL theory.

---

## Chapter 4

# External Field Coupling to Nonuniform Overhead Lines

In this chapter the DSFTL model is modified to accommodate the external field coupling generated by a nearby lightning channel. The effect of such a strike on the transient behaviour of two crossing conductors is analysed. Results obtained using the proposed model for conductors above PEC ground are compared to those obtained using full-wave simulations. In order to confirm the external field coupling in the presence of lossy ground is modelled accurately, the voltage induced on a uniform transmission line above lossy ground obtained using the proposed approach is compared to data available in the literature. A case study is performed to investigate the transient behaviour of an overhead wire above lossy ground with and without the presence of a nearby nonparallel wire. Results indicate a nearby transmission line can intensify transients occurring on a wire that cannot be calculated using the conventional uniform transmission line approaches.

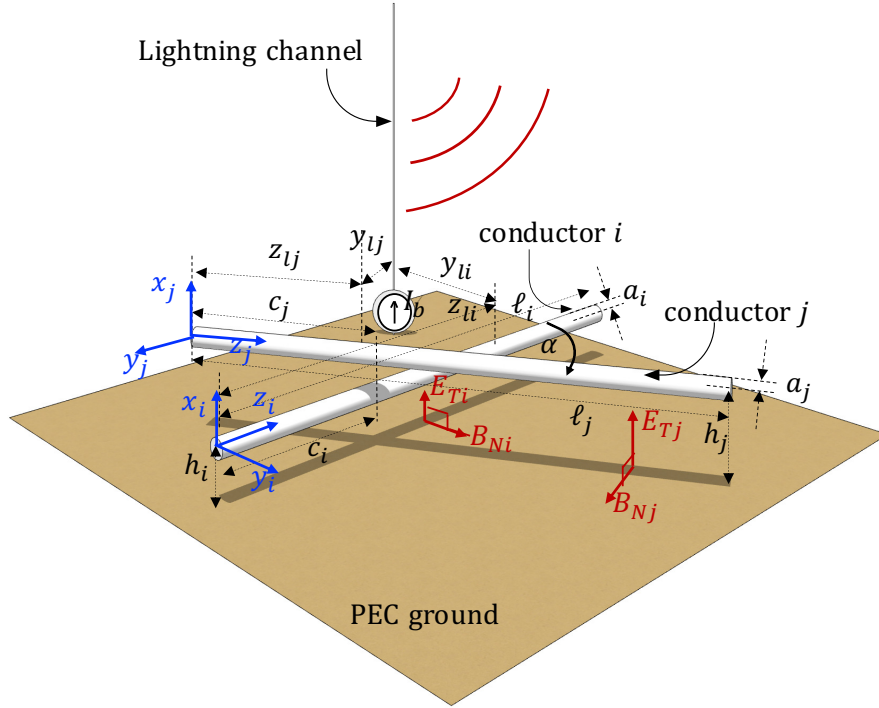


**Fig. 4.1:** A schematic of a lightning return stroke channel nearby two transmission lines crossing at an angle of  $\alpha$ .

## 4.1 Inclusion of External Fields in Transmission Lines Over Perfectly Conducting Ground

Transmission line equations with field-to-transmission line coupling for a non-uniform wire structure, as shown in Fig. 4.1, are given by [16, 39]

$$\frac{\partial}{\partial z} \mathbf{V}(z, t) + \mathbf{R}(z) \mathbf{I}(z, t) + \mathbf{L}(z) \frac{\partial}{\partial t} \mathbf{I}(z, t) = \mathbf{V}_e(z, t) \quad (4.1a)$$

$$\frac{\partial}{\partial z} \mathbf{I}(z, t) + \mathbf{G}(z) \mathbf{V}(z, t) + \mathbf{C}(z) \frac{\partial}{\partial t} \mathbf{V}(z, t) = \mathbf{I}_e(z, t) \quad (4.1b)$$

where,  $\mathbf{V}$  and  $\mathbf{I}$  are the voltage and current vectors at any location  $z$  at time  $t$ , and  $\mathbf{R}$ ,  $\mathbf{L}$ ,  $\mathbf{G}$  and  $\mathbf{C}$  are the per-unit-length (PUL) resistance, inductance, conductance, and capacitance matrices at any location  $z$ . Vectors  $\mathbf{V}_e(z, t)$  and  $\mathbf{I}_e(z, t)$  are the exciting voltage and current terms due to the electromagnetic fields generated by the lightning return stroke channel. In [29], non-uniform transmission line equations without external field coupling are solved using a 1D FDTD algorithm. As detailed in [29], for the FDTD algorithm to work, the structure is assumed to be symmetrical on either sides of the crossing (*i.e.*  $c_i = c_j$  and  $\ell_i = \ell_j$ ) and the variable  $z$  is the common variable used for the FDTD algorithm assuming  $\hat{z} = \hat{z}_i = \hat{z}_j$ . Transmission lines of different lengths can be connected to the terminals of the non-uniform model if needed [29]. In the present work,  $\mathbf{R}$  is assumed to be constant for all  $z$  and frequency independent. Since conductance of air is negligible [1] (pp. 23),  $\mathbf{G}$  is assumed to be zero for overhead wires. Space-dependent  $\mathbf{L}(z)$  and  $\mathbf{C}(z)$  for crossing conductors are given by [29].

$$\mathbf{L}(z) = \frac{\mu}{4\pi} \begin{bmatrix} \xi_{ii}(z) & \cos \alpha \xi_{ij}(z) \\ \cos \alpha \xi_{ji}(z) & \xi_{jj}(z) \end{bmatrix} \quad (4.2a)$$

$$\mathbf{C}(z) = \frac{4\pi\epsilon}{\xi_{ii}(z)\xi_{jj}(z) - \xi_{ij}(z)\xi_{ji}(z)} \begin{bmatrix} \xi_{jj}(z) & -\xi_{ij}(z) \\ -\xi_{ji}(z) & \xi_{ii}(z) \end{bmatrix} \quad (4.2b)$$

where  $\xi(z)$  were given in Section 2.1. Expressions for  $\mathbf{L}(z)$  and  $\mathbf{C}(z)$  are closed-form and can be pre-calculated before execution of the FDTD algorithm. The excitation terms can be

obtained using Taylor model [75] as

$$\mathbf{V}_e(z, t) = \frac{\partial}{\partial t} \begin{bmatrix} \int_0^{h_i} B_{Ni}(z_i, x'_i, t) dx'_i \\ \int_0^{h_j} B_{Nj}(z_j, x'_j, t) dx'_j \end{bmatrix} \quad (4.3a)$$

$$\mathbf{I}_e(z, t) = -\mathbf{C}(z) \frac{\partial}{\partial t} \begin{bmatrix} \int_0^{h_i} E_{Ti}(z_i, x'_i, t) dx'_i \\ \int_0^{h_j} E_{Tj}(z_j, x'_j, t) dx'_j \end{bmatrix} \quad (4.3b)$$

where  $B_{Ni}$  and  $E_{Ti}$  are the normal magnetic field and transverse electric field on line  $i$  created by the lightning return stroke channel, respectively.

It is common to assume that the incident fields created by a nearby lightning channel are constant over the cross section of the transmission line and are equal to the value calculated at the ground level [98]. Under this assumption, (4.3) simplifies into

$$\mathbf{V}_e(z, t) = \frac{\partial}{\partial t} \begin{bmatrix} h_i B_{Ni}(z_i, -h_i, t) \\ h_j B_{Nj}(z_j, -h_j, t) \end{bmatrix} \quad (4.4a)$$

and

$$\mathbf{I}_e(z, t) = -\mathbf{C}(z) \frac{\partial}{\partial t} \begin{bmatrix} h_i E_{Ti}(z_i, -h_i, t) \\ h_j E_{Tj}(z_j, -h_j, t) \end{bmatrix}. \quad (4.4b)$$

Following the space-time discretization convention used for currents and voltages in FDTD

algorithms given in [16], the excitation terms for a space segment  $k$  and a time step  $n$  can be written as

$$\mathbf{V}_{e,(k+\frac{1}{2})}^n = \left( \frac{\mathbf{h} \cdot \mathbf{B}_{N,(k+\frac{1}{2})}^{n+\frac{1}{2}} - \mathbf{h} \cdot \mathbf{B}_{N,(k+\frac{1}{2})}^{n-\frac{1}{2}}}{\Delta t} \right) \quad (4.5a)$$

$$\mathbf{I}_{e,k}^{n+\frac{1}{2}} = -C_k \left( \frac{\mathbf{h} \cdot \mathbf{E}_{T,k}^{n+1} - \mathbf{h} \cdot \mathbf{E}_{T,k}^n}{\Delta t} \right) \quad (4.5b)$$

where

$$\mathbf{h} = \begin{bmatrix} h_i \\ h_j \end{bmatrix}.$$

In (4.5),  $\mathbf{E}_T$  and  $\mathbf{B}_N$  are vectors consisting of transverse electric field and normal magnetic field incident on each line at ground level.

Since engineering models are considered reasonably accurate, in this work, modified transmission line linear (MTLL) model [99] is used to model the return stroke channel. Channel base current  $I_b$  is generated using Heidler formulation [73]. Electric and magnetic fields generated by the lightning return stroke at the cross-section of each line at a time  $t$  is calculated using the formulation proposed in [69] and presented in Section 2.4.

## 4.2 Inclusion of External Fields in Transmission Lines Over Lossy Ground

External fields can be coupled into transmission line equations according to Agrawal's model [76] as

$$\frac{\partial}{\partial z} \mathbf{V}^s(z, j\omega) + \mathbf{Z}(z, j\omega) \mathbf{I}(z, j\omega) = \mathbf{E}_z^{\text{inc}}(z, j\omega) \quad (4.6a)$$

$$\frac{\partial}{\partial z} \mathbf{I}(z, j\omega) + \mathbf{Y}(z, j\omega) \mathbf{V}^s(z, j\omega) = 0 \quad (4.6b)$$

where  $\mathbf{V}^s$  is the scattered voltage vector and  $\mathbf{E}_z^{\text{inc}}$  is the vector containing the horizontal electric field along each conductor given by

$$\mathbf{E}_z^{\text{inc}}(z, j\omega) = \begin{bmatrix} E_{z_i}^{\text{inc}}(z_i, j\omega, h_i) - E_{z_i}^{\text{inc}}(z_i, j\omega, 0) \\ E_{z_j}^{\text{inc}}(z_j, j\omega, h_j) - E_{z_j}^{\text{inc}}(z_j, j\omega, 0) \end{bmatrix}. \quad (4.7)$$

When using Agrawal's model since the Telegrapher's equations are solved using the scattered voltage, terminal equations are adjusted as

$$\mathbf{V}^s(0) = \mathbf{V}_S - \mathbf{Z}_S \mathbf{I}(0) + \int_0^h \mathbf{E}_x^{\text{inc}}(0, j\omega) dz \quad (4.8a)$$

and

$$\mathbf{V}^s(\ell) = \mathbf{Z}_L \mathbf{I}(\ell) + \int_0^h \mathbf{E}_x^{\text{inc}}(\ell, j\omega) dz \quad (4.8b)$$

where  $\mathbf{V}_s$  is the source voltage vector,  $\mathbf{Z}_S$  and  $\mathbf{Z}_L$  are the sending and receiving end impedances respectively and  $\mathbf{E}_x^{\text{inc}}$  is the vector containing the vertical electric field. A modified finite-difference time-domain (MFDTD) algorithm has been introduced in [27] to solve single conductor frequency dependent transmission lines by fitting the frequency-dependent impedance to a set of poles and residues using vector fitting [32]. This method was been extended into non-parallel multiconductor transmission lines in Section 3.1 In order to include the external fields the current updating equation of the MFDTD algorithm is modified as

$$\mathbf{I}_{k+\frac{1}{2}}^{n+\frac{1}{2}} = \mathbf{Z}_2^{-1} \left[ \mathbf{Z}_1 \mathbf{I}_{k+\frac{1}{2}}^{n-\frac{1}{2}} + \Delta z (\boldsymbol{\xi} + \boldsymbol{\chi}) \mathbf{I}_{k+\frac{1}{2}}^{n-\frac{3}{2}} - (\mathbf{V}_{k+1}^{s,n} - \mathbf{V}_{k+1}^{s,n}) - \Delta z \boldsymbol{\Psi}^n + \Delta z \mathbf{E}_{z,k+\frac{1}{2}}^{\text{inc},n} \right] \quad (4.9a)$$

where

$$\mathbf{Z}_1 = \Delta z \left( \frac{\mathbf{L}_{k+\frac{1}{2}}}{\Delta t} - \frac{\mathbf{R}_{k+\frac{1}{2}}}{2} + \frac{\boldsymbol{\Gamma}}{2} - 2\boldsymbol{\xi} - \boldsymbol{\chi} \right) \quad (4.9b)$$

$$\mathbf{Z}_2 = \Delta z \left( \frac{\mathbf{L}}{\Delta t} + \frac{\mathbf{R}}{2} - \frac{\boldsymbol{\Gamma}}{2} - \boldsymbol{\xi} \right) \quad (4.9c)$$

$$\boldsymbol{\xi} = \sum_{i=1}^M \frac{\mathbf{a}_{z,i}}{\alpha_{z,i}} \left[ \frac{1}{\alpha_{z,i} \Delta t} \left( 1 + \frac{1}{\alpha_{z,i} \Delta t} - \frac{e^{\alpha_{z,i} \Delta t}}{\alpha_{z,i} \Delta t} \right) \right] \quad (4.9d)$$

$$\boldsymbol{\chi} = \sum_{i=1}^M \frac{\mathbf{a}_{z,i}}{\alpha_{z,i}} \left[ \frac{1}{\alpha_{z,i} \Delta t} (e^{\alpha_{z,i} \Delta t} - 1) \right] \quad (4.9e)$$

$$\boldsymbol{\chi} = \sum_{i=1}^M \frac{\mathbf{a}_i}{\alpha_i} \quad (4.9f)$$

$$\boldsymbol{\Psi}^n = \sum_{i=1}^M \frac{\mathbf{a}_{z,i}}{\alpha_{z,i}} \boldsymbol{\Psi}_i^n \quad (4.9g)$$

$$\begin{aligned} \boldsymbol{\Psi}_i^n = & \frac{e^{\alpha_{z,i} \Delta t}}{\alpha_{z,i} \Delta t} \left( 1 + \frac{1}{\alpha_{z,i} \Delta t} - \frac{e^{\alpha_{z,i} \Delta t}}{\alpha_{z,i} \Delta t} \right) \left( 2\mathbf{I}_{k+\frac{1}{2}}^{n-\frac{3}{2}} - \mathbf{I}_{k+\frac{1}{2}}^{n+\frac{5}{2}} - \mathbf{I}_{k+\frac{1}{2}}^{n-\frac{1}{2}} \right) \\ & + \frac{e^{\alpha_{z,i} \Delta t}}{\alpha_{z,i} \Delta t} (e^{\alpha_{z,i} \Delta t} - 1) \left( \mathbf{I}_{k+\frac{1}{2}}^{n-\frac{3}{2}} - \mathbf{I}_{k+\frac{1}{2}}^{n-\frac{5}{2}} \right) + e^{\alpha_{z,i} \Delta t} \boldsymbol{\Psi}_i^{n-1}. \end{aligned} \quad (4.9h)$$

In (4.9),  $\mathbf{a}_{z,i}$  are the residue matrices corresponding to each pole  $\alpha_{z,i}$  at any location  $z$ .  $M$  is the number of poles. For terminal equations the integral of the vertical electric field at

$z = 0$  and  $z = \ell$  is approximated as [98]

$$\int_0^h \mathbf{E}_x^{\text{inc}}(0, j\omega) dz = \begin{bmatrix} h_i E_{x_i}^{\text{inc},n}(x_i = 0, z) \\ \\ h_j E_{x_j}^{\text{inc},n}(x_j = 0, z) \end{bmatrix}. \quad (4.10)$$

Horizontal external electric field vector,  $\mathbf{E}_z^{\text{inc}}$  is calculated using the Cooray-Rubinstein approximation [70] for lossy ground while the vertical external electric field vectors  $\mathbf{E}_x^{\text{inc}}$  are calculated under the PEC ground assumption [78].

### 4.3 Results and Discussion

In this section the scenario shown in Fig. 4.2 where a lightning strike occurs nearby two crossed transmission lines is modelled using the proposed method. Line heights are taken as  $h_1 = 10$  m and  $h_2 = 12$  m. A standard lightning waveform of 1.2/50  $\mu s$  with a peak value of 20 kA is chosen as the channel base current of the lightning strike generated using Heidler function for the first stroke of lightning with  $\eta = 0.9496$ ,  $\tau_1 = 2.2717 \mu s$  and  $\tau_2 = 68.526 \mu s$  [74]. Channel base current is shown in Fig. 4.3 Results obtained from the developed model for the case of PEC ground are compared with those obtained from a full-wave electromagnetic solver. Results obtained for a single conductor above lossy ground are compared with those obtained by other researchers in . A case study is also performed on the transient behaviour of the wire structure shown in Figure 4.2 above lossy ground.

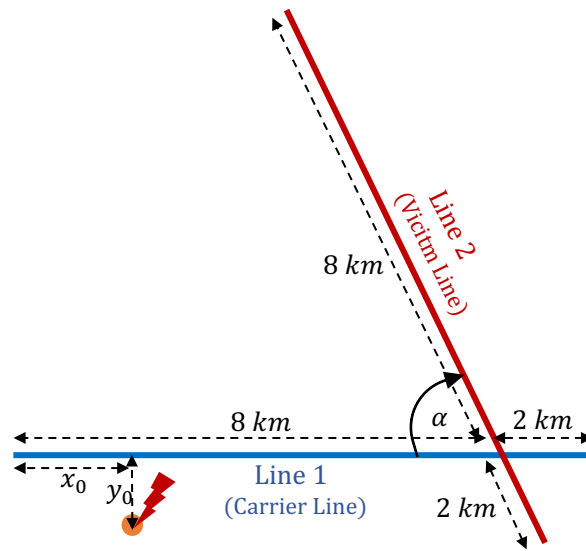


**Fig. 4.2:** A schematic a lightning strike in the vicinity of two crossed transmission lines.

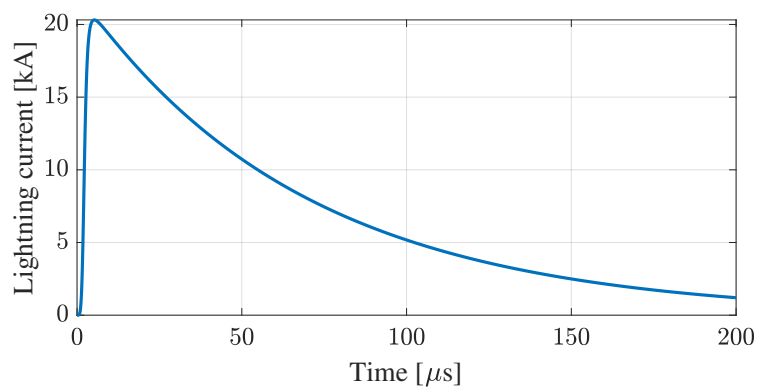


**Fig. 4.3:** 20 kA 1.2/50  $\mu\text{s}$  base current of the lightning channel generated using Heidler formulation for the first stroke.

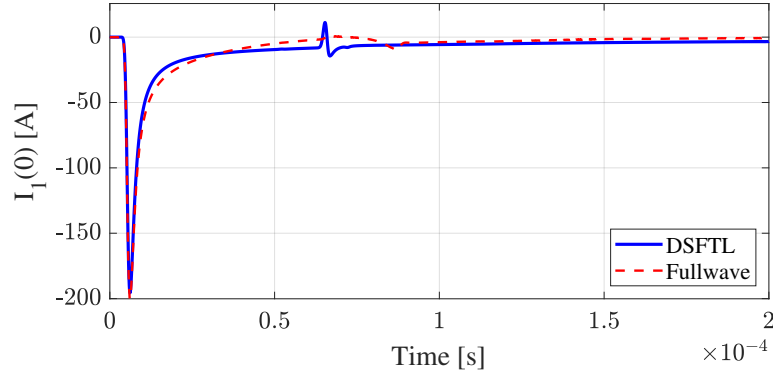


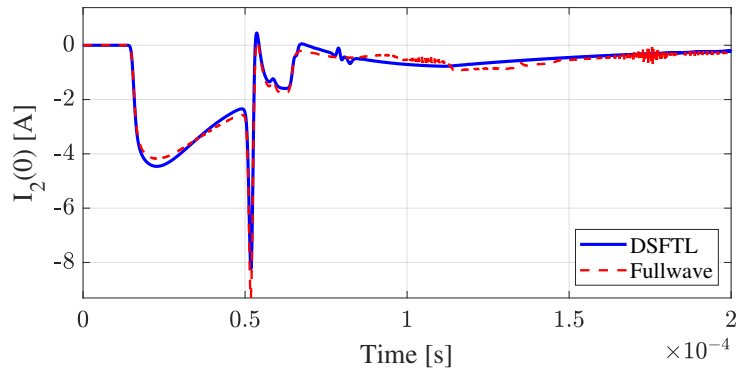
**Fig. 4.4:** Terminal current at the far end of the crossing on the carrier line when terminations of each line are matched to its corresponding characteristic impedance.

### 4.3.1 Comparison with full-wave results

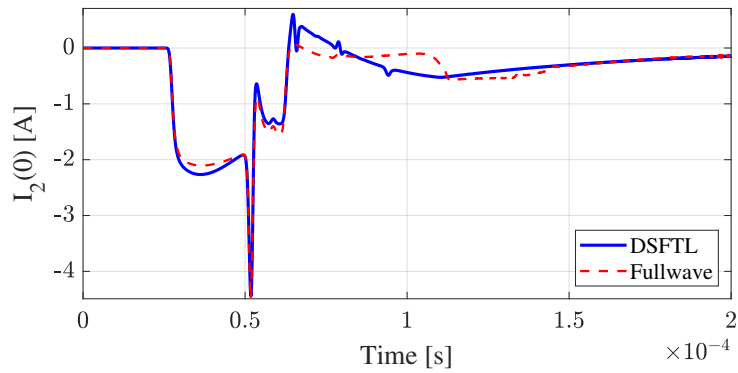
The wire structure shown in Fig. 4.2 is modeled over PEC ground with  $x_0 = 1$  km and  $y_0 = 50$  m. Conductors are assumed to be lossless and terminals of line 1 and line 2 connected to resistors of  $414 \Omega$  and  $425 \Omega$  (*i.e.* characteristic impedance of each line) respectively. Currents at the far end from the crossing obtained using the proposed DSFTL method and a full-wave thin-wire electromagnetic solver are shown in Fig. 4.4 and 4.5 for the carrier line and victim line respectively. It is seen that the results obtained using the proposed technique agree well with full-wave results.

### 4.3.2 Comparison of results in the presence of frequency-dependent ground

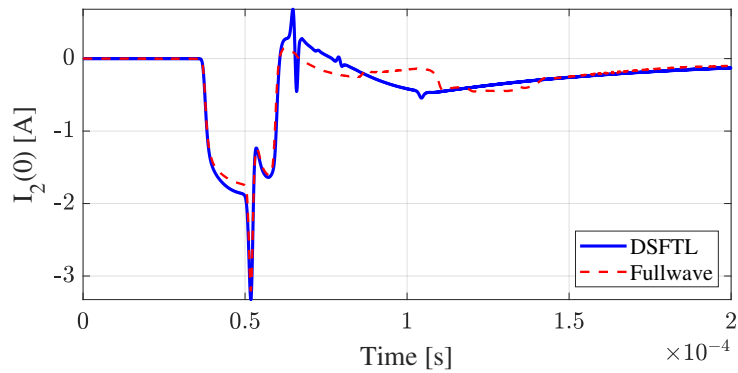
In order to confirm that the developed model is accurate for cases involving frequency-dependent ground, the single conductor case presented in [78] is modelled. Here, a lightning



(a)



(b)



(c)

**Fig. 4.5:** Terminal current at the far end of the crossing on the victim line for crossing angles of (b) 30°, (c) 60°, and (d) 90°, when terminations of each line are matched to its corresponding characteristic impedance.

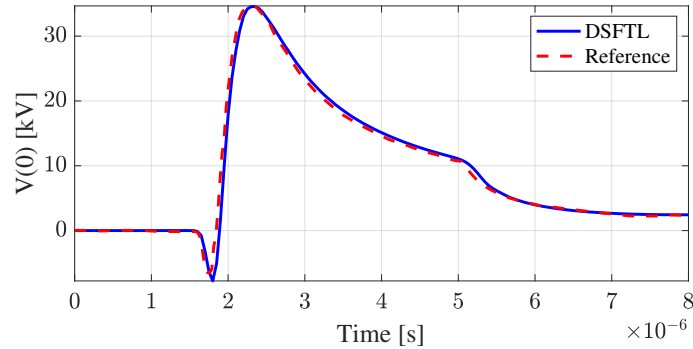


**Fig. 4.6:** Voltage induced at a terminal of a 1 km long line due to a lightning strike at a lateral distance of 50 m from its midpoint obtained using the proposed DSFTL model compared with results found in [78].

strike occurs at a lateral distance of 50 m from the midpoint of a 1 km long transmission line. The line height is 8 m and the ground conductivity is 0.01 S/m. Lightning channel parameters are set as specified in [78]. Line ends are matched to its characteristic impedance. The voltage obtained at a terminal of the line using the proposed DSFTL model is shown along with the same obtained by the authors of [78] in Figure 4.6. It is seen that results obtained using proposed model agrees with those provided in [78].

### 4.3.3 Lightning near crossing conductors above perfectly conducting ground

In this section, a scenario where a lightning strike occurs in the vicinity of two transmission lines crossing each other as shown in Fig. 4.2 is analyzed with  $x_0 = 50$  m and  $y_0 = 50$  m. Lightning strike is assumed to be closer to one line referred to as the carrier line here in. The second line, referred to as the victim line herein, experiences electromagnetic fields generated

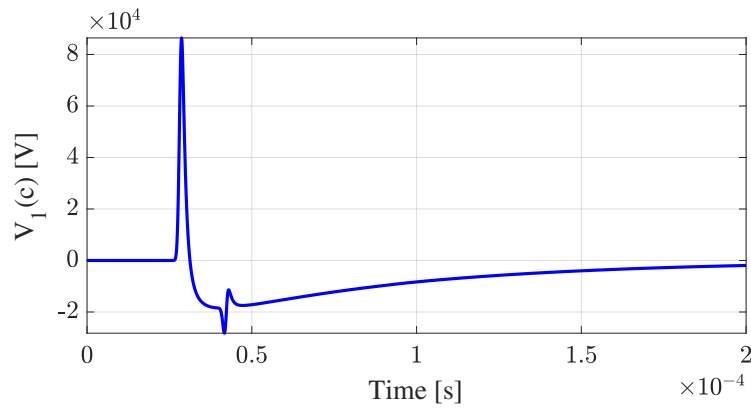
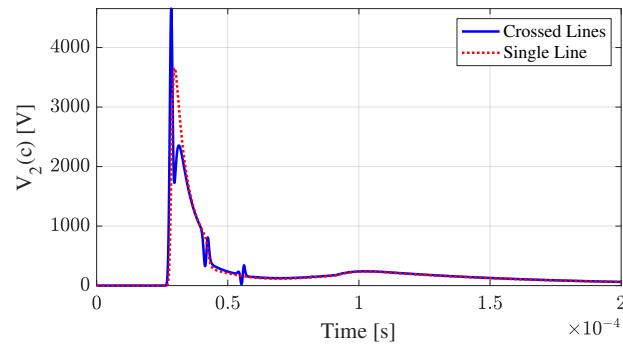


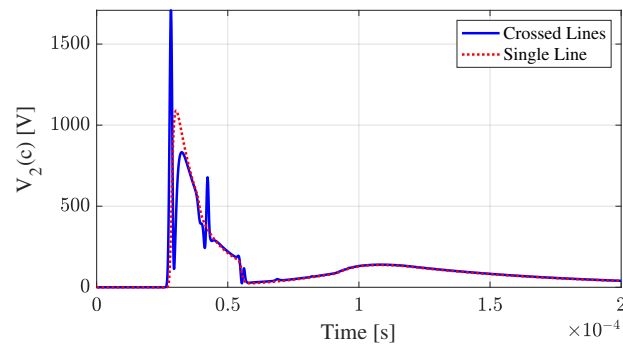
**Fig. 4.7:** Voltage at the point of crossing on the carrier line when terminations of each line are matched to its corresponding characteristic impedance.

by the lightning channel which travel directly through air as well as along the carrier line. For comparison the second line is also modelled individually. A time-step of  $0.1 \mu\text{s}$  and a space-step of 36 m is chosen such that the stability criterion [27] of FDTD calculations is satisfied.

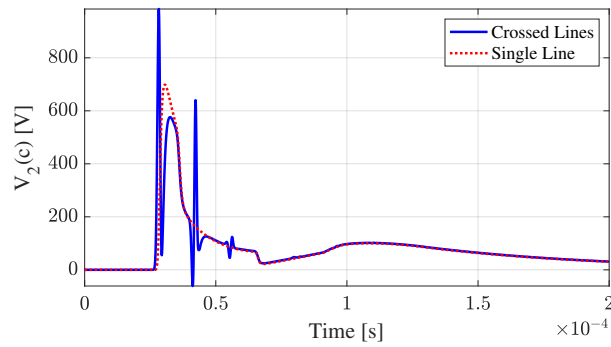
First, the structure is analyzed when the ends of each transmission line are terminated using resistive loads equal to their respective characteristic impedance. This ensures that no reflections occur at the line ends. Fig. 4.7 shows the voltage at the point of crossing on the carrier line and fig. 4.8 shows the same on the victim line for different crossing angles ( $\alpha$ ). Induced voltage due to the direct coupling through air can be seen from the single line case (in the absence of the carrier line) plotted using a dotted line. The combined effect of coupling through air and the carrier line is shown by the solid line. When the induced transient travels along the carrier line it is seen to create additional spikes in the induced voltage of the victim line. The spike due to the coupling between the two lines coincides with the peak of the induced voltage due to direct coupling to create a larger voltage than



(a)



(b)



(c)

**Fig. 4.8:** Voltage at the point of crossing on the victim line for crossing angles of (a) 30°, (b) 60°, and (c) 90°, when terminations of each line are matched to its corresponding characteristic impedance.

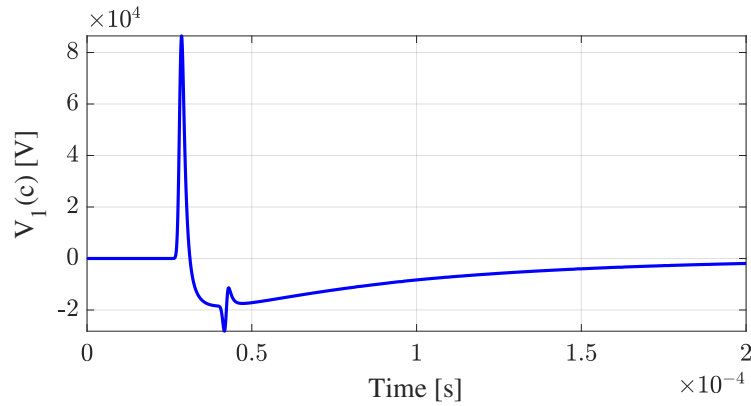


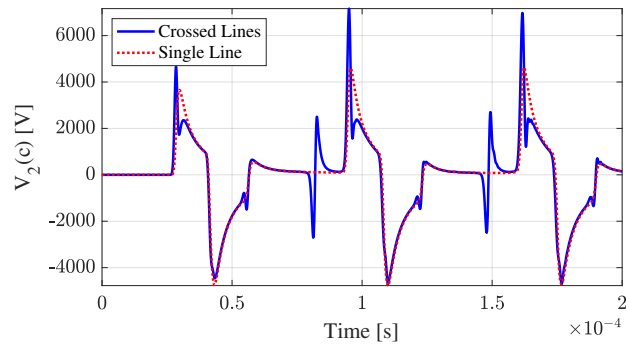
**Fig. 4.9:** Voltage at the point of crossing on the carrier line when the carrier line has matched ends and the victim line is grounded.

expected. Another observation is that the magnitude of the induced voltage on the victim line due to direct coupling is decreasing as the crossing angle increases. This is expected because when  $\alpha$  in Fig. 4.2 increases, the shortest distance from the lightning channel to the victim line increases which weakens the direct coupling. However, the voltage spike induced by the transient travelling along the carrier line drops at a lower rate than the direct coupling.

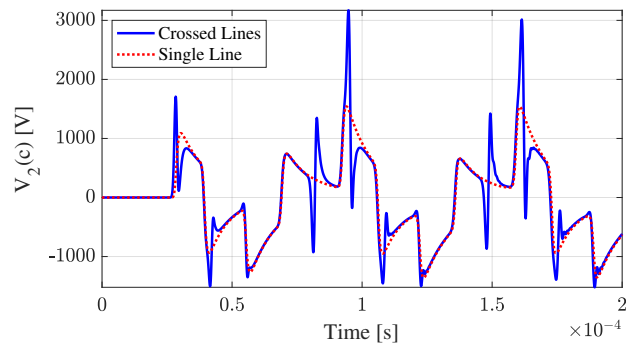
Next the victim line is grounded while the carrier line is terminated with matched loads similar to a condition during maintenance. Fig. 4.9 and Fig. 4.10 shows the induced voltages on the carrier line and victim line respectively.

It is clearly visible that the voltage spikes induced by the transient on the carrier line increases the total voltage peak of the victim line. Also, to note is that the grounded terminals of the victim line cause transients to reflect at the terminals. The back-and-forth travelling allows them to prevail for a longer period than with matched terminations.

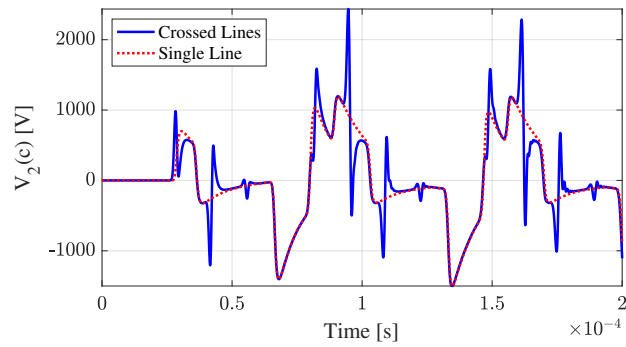
Voltage waveforms of a situation where both carrier and victim lines are grounded are shown in Figs. 4.11 and 4.12. In this case, the effect due to the coupling between the lines



(a)



(b)



(c)

**Fig. 4.10:** Voltage at the point of crossing on the victim line for crossing angles of (a) 30°, (b) 60°, and (c) 90°, when the carrier line has matched ends and the victim line is grounded.

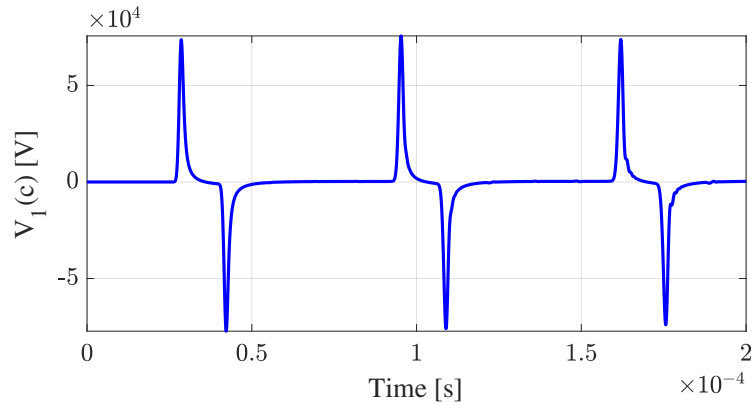
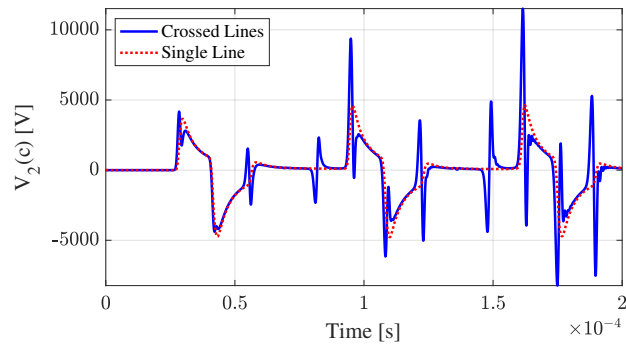


**Fig. 4.11:** Voltage at the point of crossing on the carrier line when both lines are grounded.

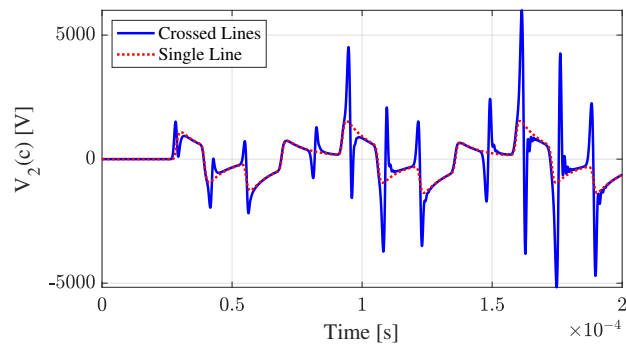
is more adverse since the transients on the carrier line also keep reflecting between the two ends. Magnitude of the induced spike keeps increasing since the geometry considered here is symmetric and each time the transient reaches the point of crossing it adds up to the already existing spike. Transients in both lines are expected to decay very slowly since only the resistance of the lines contributes to the decay of the waves.

#### 4.3.4 Lightning near crossing conductors above finitely-conducting ground

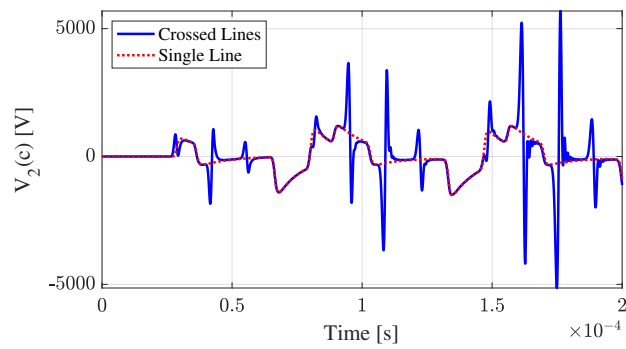
The wire structure shown in Fig. 4.2 is modeled with  $x_0 = y_0 = 50$  m. For comparison the victim line is modelled alone in the vicinity of the lightning strike at the same location. Currents at the far end from crossing on the victim line for different ground conductivity values are shown in Fig. 4.13. It is seen that for high conductive ground the current induced is close to that for PEC ground shown in Fig. 4.5. However, when the ground conductivity is lower, the induced currents are larger in magnitude and also are dispersed in shape.



(a)



(b)



(c)

**Fig. 4.12:** Voltage at the point of crossing on the victim line for crossing angles of (b) 30°, (c) 60°, and (d) 90°, when both lines are grounded.

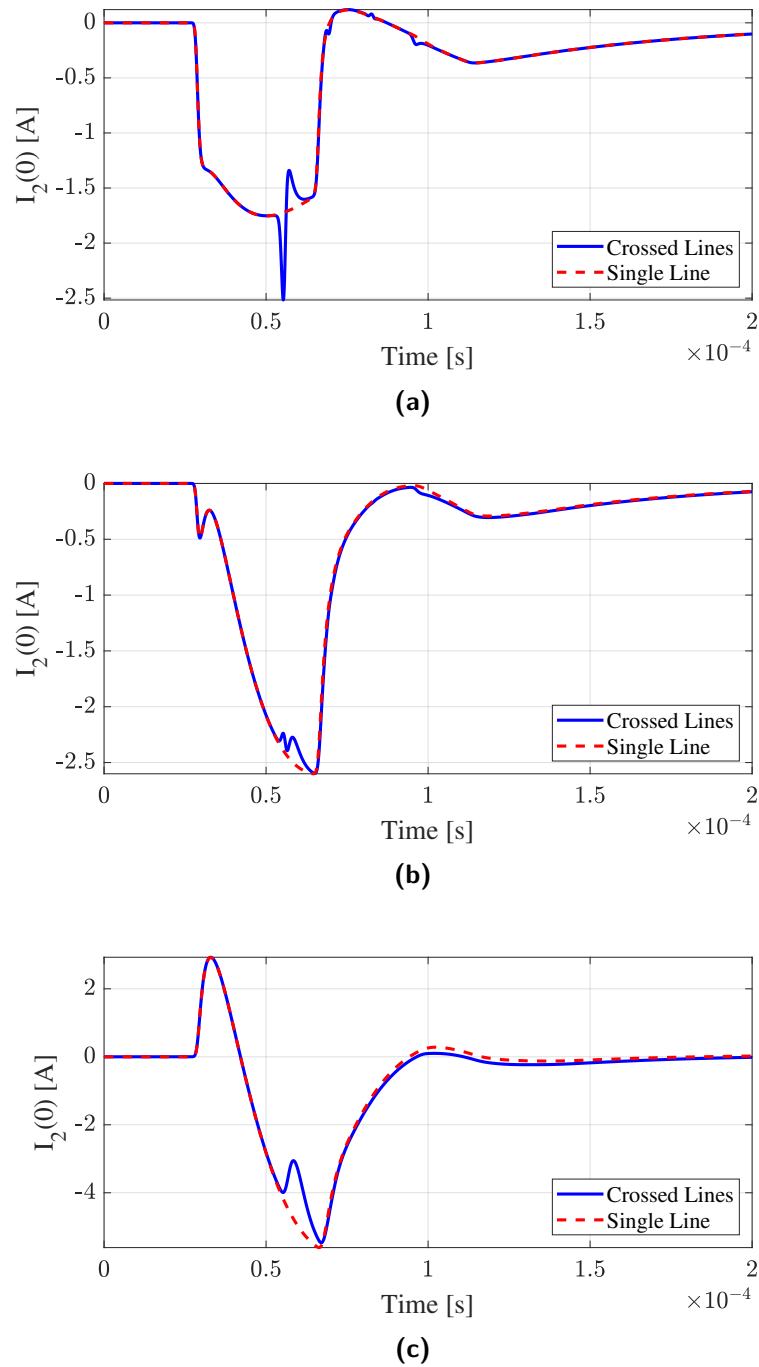


**Fig. 4.13:** Terminal current at the far end of the crossing on the victim line for a crossing angles of  $60^\circ$  and ground conductivity of (a) 0.1 S/m, (b) 0.01 S/m and (c) 0.001 S/m when terminations of each line are matched to its corresponding characteristic impedance.

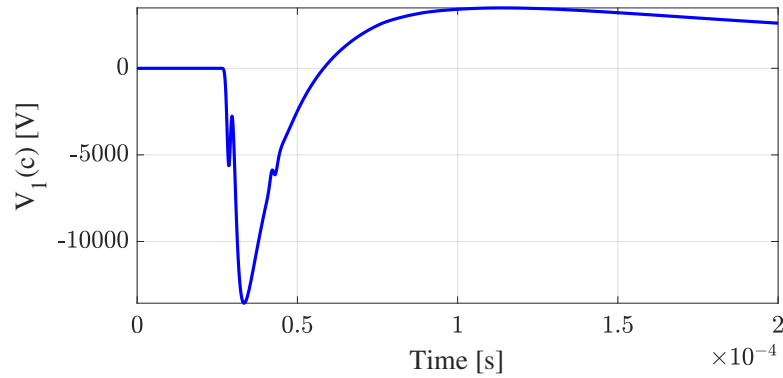


**Fig. 4.14:** Voltage at the point of crossing on the carrier line when terminations of each line are matched to their corresponding characteristic impedance.

Next the effect of the crossing angle is analyzed with the ground conductivity set at 0.001 S/m. Voltage at the point of crossing on the carrier line and victim line is shown in Figs 4.14 and 4.15 respectively. Voltage on the carrier line has decayed and dispersed when it reached the point of crossing compared to the lossless case. Therefore, voltage obtained on the victim line with the presence of the carrier line differs only slightly compared to that obtained without the carrier line.

Voltages at the point of crossing on the carrier line and victim line when both lines are grounded is shown in Figs. 4.16 and 4.17 respectively. The ground conductivity is set at 0.001 S/m. In contrast to the previous case where line ends were matched, the voltage on the victim line with the presence of the carrier line consists of additional voltage spikes and higher peaks than the same in the absence of the carrier line.

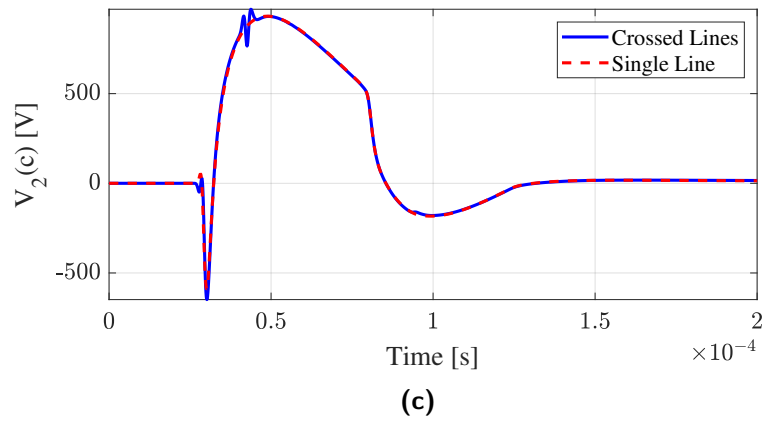
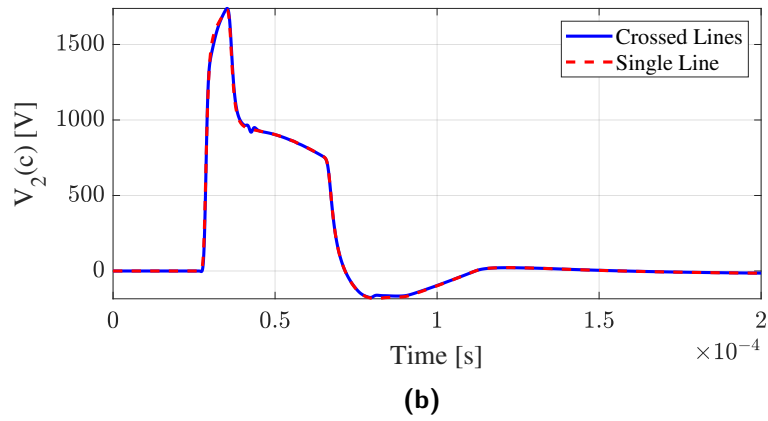
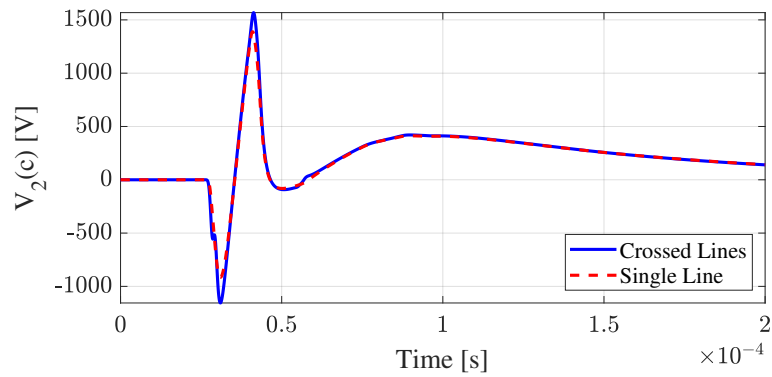


**Fig. 4.15:** Voltage at the point of crossing on the victim line for crossing angles of (a)  $30^\circ$ , (b)  $90^\circ$ , and (c)  $150^\circ$ , when terminations of each line are matched to their corresponding characteristic impedance.

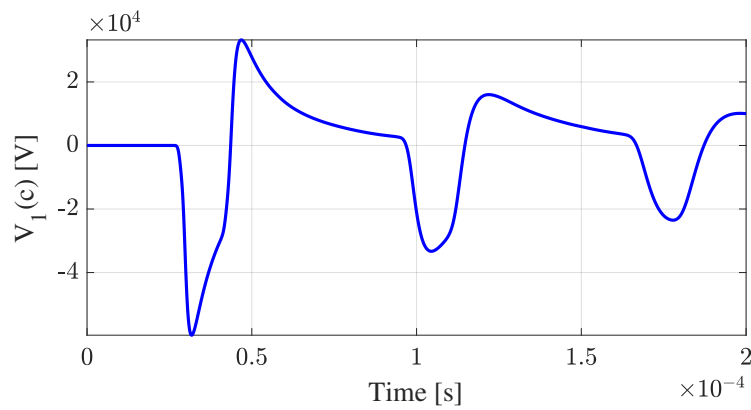


**Fig. 4.16:** Voltage at the point of crossing on the carrier line when terminals of both line are grounded

## 4.4 Summary

In this chapter a transmission line models with field-to-transmission line coupling was developed for both, frequency-independent and frequency-dependent nonuniform structures. The transient behavior of a non-uniform transmission line structure due to a nearby lightning strike was analyzed under different ground conductivity, crossing angles and terminating conditions. It was seen that the transients induced in the line closer to the lightning strike travel along the line to generate additional spikes in the second line which is farther away from the lightning channel. Conventional transmission line models that assume a uniform cross-section are not capable of modelling these additional transients. Therefore, there is a possibility of underestimating the effects due to lightning surges which can result in inadequate design of protection schemes.

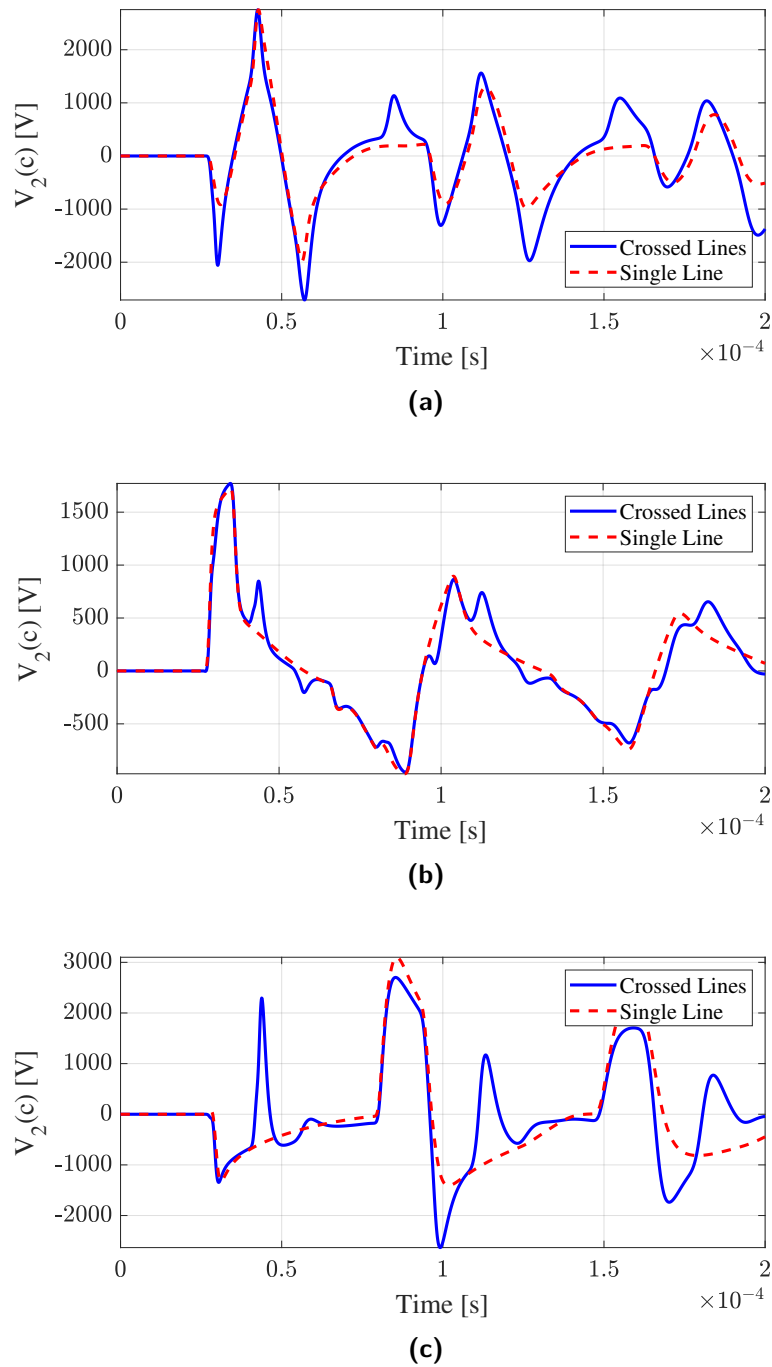


**Fig. 4.17:** Voltage at the point of crossing on the victim line for crossing angles of (a) 30°, (b) 90°, and (c) 150°, when terminals of both line are grounded

---

## Chapter 5

# Nonparallel Overhead and Buried Conductors

In this chapter, the DSFTL model introduced in Section 3.1 is extended for nonparallel overhead and buried conductors. Self coupling of overhead and buried conductors is formulated using thin-wire scattering theory [39] and complex image theory [51]. A formulation for the mutual coupling between overhead and buried wires is first obtained using the Hertzian vector for the field coupling between two media and following the derivation procedure given in [56] to calculate the mutual impedance between two inclined conductors in air. The resulting formulation is then simplified to a closed-form expression using the procedure introduced by Lucca for parallel wires in [54]. Results obtained using the proposed model are compared with those calculated using a commercial full-wave electromagnetic solver for different values of the crossing angle, ground conductivity, conductor radius and burial depth. A case study is also performed on induced voltages in the buried conductor during direct lightning strikes to the overhead line.

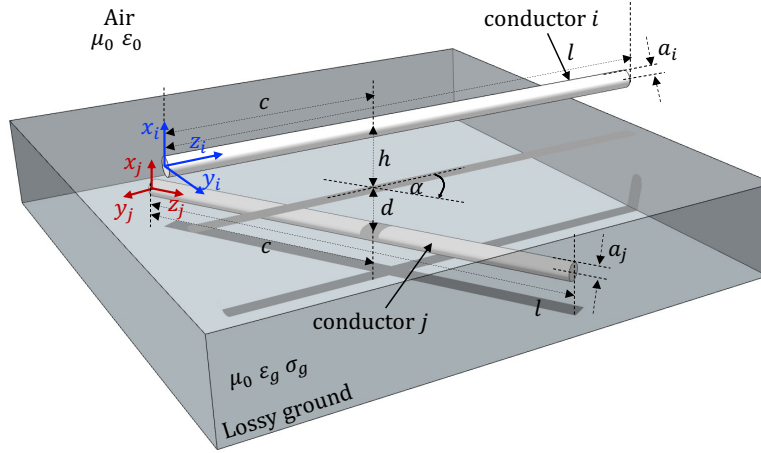


**Fig. 5.1:** Single-conductor over head transmission line crossing above a bare conductor buried in finitely-conducting ground.

## 5.1 DSFTL Model for Overhead and Buried Conductors

Transmission line equations for a nonuniform wire structure in the frequency domain can be given as [16]

$$\frac{\partial}{\partial z} \mathbf{V}(z, j\omega) + \mathbf{Z}(z, j\omega) \mathbf{I}(z, j\omega) = \mathbf{0} \quad (5.1a)$$

$$\frac{\partial}{\partial z} \mathbf{I}(z, j\omega) + \mathbf{Y}(z, j\omega) \mathbf{V}(z, j\omega) = \mathbf{0} \quad (5.1b)$$

where,  $\mathbf{V}$  and  $\mathbf{I}$  are the voltage and current vectors and  $\mathbf{Z}$  and  $\mathbf{Y}$  are the PUL impedance and admittance matrices at any location  $z$ . For a wire structure as shown in Fig. 5.1 where both overhead and underground conductors are present, elements of  $\mathbf{Z}$  and  $\mathbf{Y}$  can be written as

$$\mathbf{Z} = \begin{bmatrix} Z_o & Z_{ob} \\ Z_{ob} & Z_b \end{bmatrix} \quad (5.2a)$$

and

$$\mathbf{Y} = \begin{bmatrix} Y_o & Y_{ob} \\ Y_{ob} & Y_b \end{bmatrix} \quad (5.2b)$$

where, subscript “o” stands for overhead wires, “b” for buried wires, and “ob” for the mutual coupling between overhead and buried wires.  $Z_o$  of a overhead line of finite length  $\ell_i$  at any location  $z$  can be obtained as explained in Section 3.1 as

$$Z_o = \frac{j\omega\mu_0}{4\pi} \xi \quad (5.3a)$$

where,

$$\begin{aligned} \xi = & \ln \left( \ell + \sqrt{(\ell - z_i)^2 + a_i^2} - z_i \right) - \ln \left( \sqrt{(\ell - z_i)^2 + a_i^2} - z_i \right) \\ & - \ln \left( \ell + \sqrt{(\ell - z_i)^2 + (2h + 2p)^2} - z_i \right) + \ln \left( \sqrt{(\ell - z_i)^2 + (2h + 2p)^2} - z_i \right). \end{aligned} \quad (5.3b)$$

In (5.3b),  $p$  is the complex image depth [51] given by

$$p = \frac{1}{\sqrt{j\omega\mu_0(\sigma_g + j\omega\varepsilon_g)}}. \quad (5.4)$$

$\mu_0$ ,  $\varepsilon_g$  and  $\sigma_g$  are the permeability of free space, permittivity, and conductivity of the ground, respectively.  $Y_o$  of a overhead line of finite length  $\ell_i$  can be obtained using [100]

$$Y_o = 4\pi\varepsilon_0 j\omega\xi' \quad (5.5a)$$

where,

$$\xi' = \sinh^{-1} \left( \frac{\ell - z_i}{a_i} \right) - \sinh^{-1} \left( \frac{-z_i}{a_i} \right) - \sinh^{-1} \left( \frac{\ell - z_i}{2h_i} \right) + \sinh^{-1} \left( \frac{-z_i}{2h_i} \right). \quad (5.5b)$$

According to the complex image theory explained in [51] for a overhead conductor at height  $h$ , the ground half-space is replaced with air and an image of the conductor is placed at a complex depth of  $h + 2p$ . Similarly for a buried conductor at a burial depth  $d$  the air half-space can be replaced with ground and an image of the conductor be placed at a complex height  $d + 2p$  [51]. Therefore, following the procedure presented in [100] for overhead lines, the self impedance of a buried conductor ( $Z_b$ ) of finite length  $\ell_j$  can be written as

$$Z_b = \frac{j\omega\mu_0}{4\pi} \chi \quad (5.6a)$$

where,

$$\begin{aligned} \chi = & \ln \left( \ell + \sqrt{(\ell - z_j)^2 + a_j^2} - z_j \right) - \ln \left( \sqrt{(\ell - z_j)^2 + a_j^2} - z_j \right) \\ & - \ln \left( \ell + \sqrt{(\ell - z_j)^2 + (2d + 2p)^2} - z_j \right) + \ln \left( \sqrt{(\ell - z_j)^2 + (2d + 2p)^2} - z_j \right). \end{aligned} \quad (5.6b)$$

The self admittance  $Y_b$  can be obtained using [101]

$$Y_o = j4\pi\omega(\varepsilon_0\varepsilon_g + \frac{\sigma_g}{j\omega})\chi^{-1}. \quad (5.7)$$

If the buried conductor is insulated, the sheath capacitance needs to added to the admittance,

and the total admittance can be obtained as [101]

$$Y_{o,tot} = j\omega \frac{C_s Y_o}{j\omega C_s + Y_o} \quad (5.8a)$$

where  $C_s$  is the capacitance of the insulation sheath given by

$$C_s = \frac{2\pi\epsilon_s}{\ln \frac{b_j}{a_j}} \quad (5.8b)$$

where  $\epsilon_s$ ,  $a_j$  and  $b_j$  are the relative permittivity, inner radius and outer radius of the sheath, respectively.

To obtain a closed-form formulation for the mutual impedance between a overhead and buried conductor placed at an angle of  $\alpha$  to each other one has to consider the field created in ground by a horizontal electric dipole (HED) in air. The  $z$  component of the Hertzian vector of the electric field in ground at a depth  $d$  and a horizontal distance  $r$  due to a HED of length  $ds$  placed in air at a height  $h$  carrying current  $I$  given by [56],

$$\Pi_{1,z} = \frac{j\omega\mu_0 I ds}{4\pi\gamma_1^2} \int_0^\infty \frac{2ue^{-\alpha_0 h} e^{-\alpha_1 d}}{\alpha_0 + \alpha_1} J_0(ru) du \quad (5.9a)$$

where

$$\alpha_0 = \sqrt{u^2 + \gamma_0^2} \quad (5.9b)$$

and

$$\alpha_1 = \sqrt{u^2 + \gamma_1^2}. \quad (5.9c)$$

In (5.9),  $\gamma_0$  is the propagation constant of air given by  $\gamma_0 = j\omega\sqrt{\mu_0\epsilon_0}$  while  $\gamma_1$  is the propagation constant of ground given by  $\gamma_1 = \sqrt{j\omega\mu_0(\sigma_g + j\omega\epsilon_g)}$ .  $J_0$  is the zeroth order Bessel

function of the first kind. As explained in [56] the mutual impedance of between the overhead conductor ( $i$ ) and the buried conductor ( $j$ ) can be obtained using

$$Z_{\text{ob}} = \frac{j\omega\mu_0 \cos \alpha}{2\pi} \int_0^\ell \int_0^\infty \frac{ue^{-\alpha_0 h} e^{-\alpha_1 d}}{\alpha_0 + \alpha_1} J_0(ru) du dz'_i \quad (5.10)$$

In [29] it was shown that for two crossing transmission lines of finite length the mutual impedance and admittance near line ends are negligible compared to those in areas near the crossing. Also, in [39] it is explained that if the location ( $z$ ) of an observation point on a transmission line is sufficiently far from its ends (*i.e.* by a distance greater than twice the maximum cross-sectional dimension), then it can be considered as a point on an infinitely long transmission line. Since a crossing between an overhead line and a buried pipeline generally occurs sufficiently far from its ends  $Z_{\text{ob}}$  in (5.10) can be approximated as

$$Z_{\text{ob}} = \frac{j\omega\mu_0 \cos \alpha}{2\pi} \int_{-\infty}^\infty \int_0^\infty \frac{ue^{-\alpha_0 h} e^{-\alpha_1 d}}{\alpha_0 + \alpha_1} J_0(ru) du dz'_i. \quad (5.11)$$

This approximations allows the simplification of  $Z_{\text{ob}}$  into a closed-form expression using well known mathematical identities. For overhead wires [54]

$$\alpha_0 \approx u \quad (5.12)$$

and  $\gamma_g^2 \approx j\omega\mu_0\sigma_g = \frac{1}{p^2}$  [54] which gives

$$\alpha_1 \approx \sqrt{u^2 + \frac{1}{p^2}} \quad (5.13)$$

Substituting (5.12) and (5.13) in (5.11) and rearranging further gives

$$Z_{\text{ob}} = \frac{j\omega\mu_0 \cos \alpha}{2\pi} \int_0^\infty \int_0^\infty \frac{2ue^{-hu} e^{-d\sqrt{u^2 + \frac{1}{p^2}}}}{u + \sqrt{u^2 + \frac{1}{p^2}}} J_0(ru) du dz'_i. \quad (5.14)$$

In [54] it is shown that an integral of the above format can be rearranged into

$$Z_{\text{ob}} = \frac{j\omega\mu_0 \cos \alpha}{2\pi} \left[ \int_0^\infty \int_0^\infty u \frac{e^{-u(h+d)} - e^{-u(h+d+2p)}}{u} J_0(ru) du dz'_i + C \right] \quad (5.15a)$$

where

$$C = \frac{1}{\gamma_g^3} \frac{\partial^2 Q}{\partial \bar{y}_{ij}^2} + \frac{3}{20\gamma_g^5} \frac{\partial^4 Q}{\partial \bar{y}_{ij}^4} + \dots \quad (5.15b)$$

In (5.15b),  $\bar{y}_2$  is the shortest horizontal distance from a point  $z_i$  on the overhead line to the buried line that can be written as

$$\bar{y}_{ij} = (c - z_i) \sin \alpha \quad (5.16)$$

and

$$Q = \frac{\bar{H}_{ij}}{\bar{R}_{ij}^2} \quad (5.17a)$$

where  $H_e$  is given by [54]

$$\bar{H}_{ij} = h + d + 2p \quad (5.17b)$$

and

$$\bar{R}_{ij} = \sqrt{\bar{H}_{ij}^2 + \bar{y}_{ij}^2}. \quad (5.17c)$$

For typical power line and pipeline scenarios approximating  $C$  using the first term of the series expansion in (5.15b) is sufficient [54]. Therefore, using (5.15b), (5.16) and (5.17),  $C$

can be written as

$$C = \frac{2\bar{H}_{ij} \bar{H}_{ij}^2 - 3\bar{y}_{ij}^2}{3\gamma_g^3 \bar{R}_{ij}^6}. \quad (5.18)$$

The expression for  $C$  in (5.18) is identical by format to that obtained by Lucca in [54] for a parallel overhead and buried wire. However,  $\bar{H}_{ij}$ ,  $\bar{y}_{ij}$  and  $\bar{R}_{ij}$  terms are dependent on location ( $z_i$ ) at which it is calculated and the crossing angle ( $\alpha$ ).

Also, using the Sommerfeld Identity [48] the integral in (5.15a) can be rewritten as

$$\begin{aligned} & \int_0^\infty \int_0^\infty 2u \frac{e^{-u(h+d)} - e^{-u(h+d+2p)}}{u} J_0(ru) du dz'_i \\ &= \int_0^\infty 2 \left( \frac{e^{-\gamma_g R_{12}}}{R_{12}} - \frac{e^{-\gamma_g \bar{R}_{12}}}{\bar{R}_{12}} \right) dz'_i. \end{aligned} \quad (5.19a)$$

where,

$$R_{ij} = \sqrt{(h+d)^2 + \bar{y}_{ij}^2}. \quad (5.19b)$$

Substituting (5.18) and (5.19a) in (5.15a) gives

$$Z_{\text{ob}} = \frac{j\omega\mu_0 \cos \alpha}{2\pi} \left[ \int_0^\infty \left( \frac{e^{-\gamma_g R_{12}}}{R_{12}} - \frac{e^{-\gamma_g \bar{R}_{12}}}{\bar{R}_{12}} \right) dz'_i + \frac{2\bar{H}_{ij} \bar{H}_{ij}^2 - 3\bar{y}_{ij}^2}{3\gamma_g^3 \bar{R}_{ij}^6} \right]. \quad (5.20)$$

The infinite length assumption can be reversed for the integration term in (5.20) as

$$Z_{\text{ob}} = \frac{j\omega\mu_0 \cos \alpha}{2\pi} \left[ \frac{1}{2} \int_0^\ell \left( \frac{e^{-\gamma_g R_{12}}}{R_{12}} - \frac{e^{-\gamma_g \bar{R}_{12}}}{\bar{R}_{12}} \right) dz'_i + \frac{2\bar{H}_{ij} \bar{H}_{ij}^2 - 3\bar{y}_{ij}^2}{3\gamma_g^3 \bar{R}_{ij}^6} \right]. \quad (5.21)$$

By substituting the analytical formula derived in [100] for integrals of this format, an ex-

pression for the mutual impedance between overhead and buried wires can be obtained as

$$\begin{aligned}
 Z_{\text{ob}} = \frac{j\omega\mu_0 \cos \alpha}{4\pi} & \left[ \right. \\
 & \ln \left( \ell + \sqrt{[(\ell - c) + (z_i - c) \cos \alpha]^2 + [(z_i - c) \sin \alpha]^2 + (h + d)^2} - c + (z_i - c) \cos \alpha \right) \\
 & - \ln \left( \sqrt{[(\ell - c) + (z_i - c) \cos \alpha]^2 + [(z_i - c) \sin \alpha]^2 + (h + d)^2} - c + (z_i - c) \cos \alpha \right) \\
 & - \ln \left( \ell + \sqrt{[\ell - c + (z_i - c) \cos \alpha]^2 + [(z_i - c) \sin \alpha]^2 + (h + d + 2p)^2} - c + (z_i - c) \cos \alpha \right) \\
 & + \ln \left( \sqrt{[(\ell - c) + (z_i - c) \cos \alpha]^2 + [(z_i - c) \sin \alpha]^2 + (h + d + 2p)^2} - c + (z_i - c) \cos \alpha \right) \\
 & \left. + \frac{4\bar{H}_{ij} \bar{H}_{ij}^2 - 3\bar{y}_{ij}^2}{3\gamma_g^3 \bar{R}_{ij}^6} \right]
 \end{aligned} \tag{5.22}$$

Mutual admittance between overhead and buried conductors ( $\mathbf{Y}_{\text{ob}}$ ) is generally assumed to be zero [102].

## 5.2 Time-Domain Implementation

Equation (5.1) in the time-domain gives

$$\frac{\partial}{\partial z} \mathbf{V}(z, t) + \mathbf{Z}(z, t) * \mathbf{I}(z, t) = \mathbf{0} \tag{5.23a}$$

$$\frac{\partial}{\partial z} \mathbf{I}(z, t) + \mathbf{Y}(z, t) * \mathbf{V}(z, t) = \mathbf{0} \tag{5.23b}$$

where “\*” denotes convolution. Since the admittance is also frequency dependent, the MFDTD algorithm introduced in [27] and then extended to nonparallel overhead lines in Section 3.2 is modified to accommodate frequency dependent admittance. In this case the

admittance matrices is also fitted into a matrix function of the format [32]

$$\mathbf{Y}(z, j\omega) = \mathbf{G}(z) + j\omega\mathbf{C}(z) + \mathbf{Y}'(z, j\omega) \quad (5.24a)$$

where

$$\mathbf{Y}'(z, j\omega) = \sum_{k=1}^M \frac{\mathbf{a}'_k(z)}{j\omega - \alpha'_k(z)}. \quad (5.24b)$$

In (5.24),  $\mathbf{a}'_k(z)$  is the residue matrices corresponding to each pole  $\alpha'_k(z)$  respectively at any location  $z$ .  $M$  is the number of poles. With this approximation (5.23) can be re-written as

$$\frac{\partial}{\partial z}\mathbf{V}(z, t) = -\mathbf{R}(z)\mathbf{I}(z, t) - \mathbf{L}(z)\frac{\partial}{\partial t}\mathbf{I}(z, t) - \mathbf{Z}'(z, t) * \mathbf{I}(z, t) \quad (5.25a)$$

$$\frac{\partial}{\partial z}\mathbf{I}(z, t) = -\mathbf{G}(z)\mathbf{V}(z, t) - \mathbf{C}(z)\frac{\partial}{\partial t}\mathbf{V}(z, t) - \mathbf{Y}'(z, t) * \mathbf{V}(z, t). \quad (5.25b)$$

It should be noted that an FDTD algorithm to solve a single conductor transmission line with both frequency dependent impedance and admittance has been introduced in [101]. However, in [101] only the voltage is calculated at the terminal nodes. Since, in the MFDTD algorithm both the current and voltage is calculated at the terminal loads it is more suitable for implementation on EMT-simulators. Therefore it has been chosen to be extended to buried structures in this paper.

Following the space-time discretization convention used for currents and voltages in FDTD algorithms [16, 27] shown in Fig. 5.2, the updating equation for the current at a space-segment  $k$  and a time iteration  $n$  can be written as

$$\mathbf{I}_{k+\frac{1}{2}}^{n+\frac{1}{2}} = \mathbf{Z}_2^{-1} \left[ \mathbf{Z}_1 \mathbf{I}_{k+\frac{1}{2}}^{n-\frac{1}{2}} + \Delta z (\boldsymbol{\xi} + \boldsymbol{\chi}) \mathbf{I}_{k+\frac{1}{2}}^{n-\frac{3}{2}} - (\mathbf{V}_{k+1}^n - \mathbf{V}_{k+1}^{n-1}) - \Delta z \boldsymbol{\Psi}^n \right] \quad (5.26a)$$

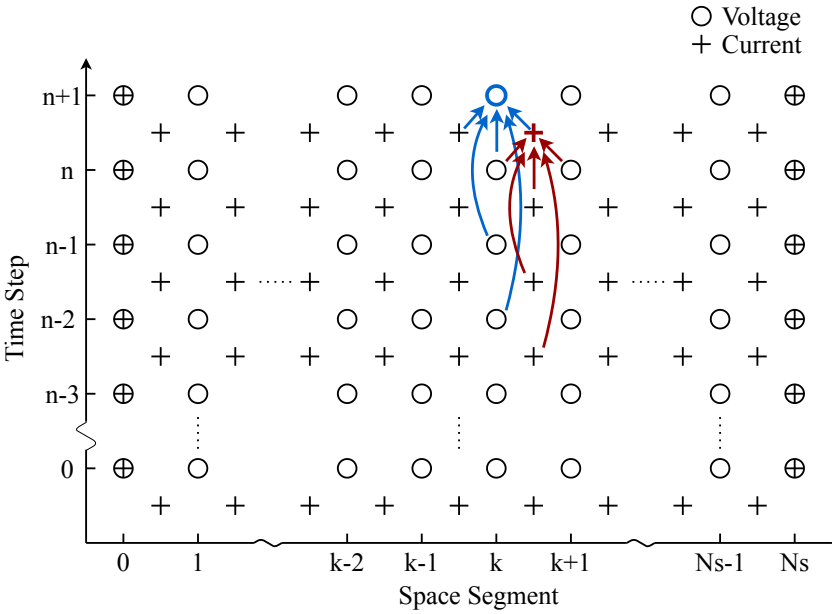


**Fig. 5.2:** Illustration of the space-time discretization and the update procedure of voltage and current vectors of space segment  $k$  at time-step  $n$  in the MFDTD algorithm.

where

$$\mathbf{Z}_1 = \Delta z \left( \frac{\mathbf{L}(z)}{\Delta t} - \frac{\mathbf{R}(z)}{2} + \frac{\mathbf{\Gamma}}{2} - 2\boldsymbol{\xi} - \boldsymbol{\chi} \right) \quad (5.26b)$$

$$\mathbf{Z}_2 = \Delta z \left( \frac{\mathbf{L}(z)}{\Delta t} + \frac{\mathbf{R}(z)}{2} - \frac{\mathbf{\Gamma}}{2} - \boldsymbol{\xi} \right) \quad (5.26c)$$

$$\boldsymbol{\xi} = \sum_{i=1}^M \frac{\mathbf{a}_i(z)}{\alpha_i(z)} \left[ \frac{1}{\alpha_i(z)\Delta t} \left( 1 + \frac{1}{\alpha_i(z)\Delta t} - \frac{e^{\alpha_i(z)\Delta t}}{\alpha_i(z)\Delta t} \right) \right] \quad (5.26d)$$

$$\boldsymbol{\chi} = \sum_{i=1}^M \frac{\mathbf{a}_i(z)}{\alpha_i(z)} \left[ \frac{1}{\alpha_i(z)\Delta t} (e^{\alpha_i(z)\Delta t} - 1) \right] \quad (5.26e)$$

$$\boldsymbol{\Psi}^n = \sum_{i=1}^M \frac{\mathbf{a}_i(z)}{\alpha_i(z)} \boldsymbol{\Psi}_i^n \quad (5.26f)$$

$$\begin{aligned} \boldsymbol{\Psi}_i^n = & \frac{e^{\alpha_i(z)\Delta t}}{\alpha_i(z)\Delta t} \left( 1 + \frac{1}{\alpha_i(z)\Delta t} - \frac{e^{\alpha_i(z)\Delta t}}{\alpha_i(z)\Delta t} \right) \left( 2\mathbf{I}_{k+\frac{1}{2}}^{n-\frac{3}{2}} - \mathbf{I}_{k+\frac{1}{2}}^{n+\frac{5}{2}} - \mathbf{I}_{k+\frac{1}{2}}^{n-\frac{1}{2}} \right) \\ & + \frac{e^{\alpha_i(z)\Delta t}}{\alpha_i(z)\Delta t} (e^{\alpha_i(z)\Delta t} - 1) \left( \mathbf{I}_{k+\frac{1}{2}}^{n-\frac{3}{2}} - \mathbf{I}_{k+\frac{1}{2}}^{n-\frac{5}{2}} \right) + e^{\alpha_i(z)\Delta t} \boldsymbol{\Psi}_i^{n-1}. \end{aligned} \quad (5.26g)$$

In (5.26),  $\Delta z$  is the space step and  $\Delta t$  is the time step. Similarly, for a transmission line system with frequency dependent admittance, the voltage equation can be written as

$$\mathbf{V}_k^{n+1} = \mathbf{Y}_2^{-1} \left[ \mathbf{Y}_1 \mathbf{V}_k^n + \Delta z (\boldsymbol{\xi}' + \boldsymbol{\chi}') \mathbf{V}_k^{n-1} - (\mathbf{I}_{k+\frac{1}{2}}^{n+\frac{1}{2}} - \mathbf{I}_{k-\frac{1}{2}}^{n+\frac{1}{2}}) - \Delta z \boldsymbol{\Psi}'^n \right] \quad (5.27a)$$

where

$$\mathbf{Y}_1 = \Delta z \left( \frac{\mathbf{C}(z)}{\Delta t} - \frac{\mathbf{G}(z)}{2} + \frac{\mathbf{\Gamma}'}{2} - 2\boldsymbol{\xi}' - \boldsymbol{\chi}' \right) \quad (5.27b)$$

$$\mathbf{Y}_2 = \Delta z \left( \frac{\mathbf{C}(z)}{\Delta t} + \frac{\mathbf{G}(z)}{2} - \frac{\mathbf{\Gamma}'}{2} - \boldsymbol{\xi}' \right) \quad (5.27c)$$

and  $\boldsymbol{\xi}'$ ,  $\boldsymbol{\chi}'$  and  $\boldsymbol{\Psi}'$  are analogous to  $\boldsymbol{\xi}$ ,  $\boldsymbol{\chi}$  and  $\boldsymbol{\Psi}$  respectively in the current equation. In order

to integrate MFDTD into EMT simulators, both the current and voltage are calculated at the terminal loads as seen in Fig. 5.2. While terminal voltage vectors ( $\mathbf{V}_0^{n+1}$  and  $\mathbf{V}_{N_S}^{n+1}$ ) are updated by the EMT simulator, terminal current vectors are calculated by discretizing the half-space-segment ( $\Delta z/2$ ) at the two ends of the line [27]. Using (5.27a), the voltage equation at the starting node can be written as

$$\mathbf{V}_0^{n+1} = \mathbf{Y}_2^{-1} \left[ \mathbf{Y}_1 \mathbf{V}_0^n + \frac{\Delta z}{2} (\boldsymbol{\xi}' + \boldsymbol{\chi}') \mathbf{V}_0^{n-1} - \left( \mathbf{I}_{\frac{1}{2}}^{n+\frac{1}{2}} - \frac{\mathbf{I}_0^{n+1} + \mathbf{I}_0^n}{2} \right) - \frac{\Delta z}{2} \boldsymbol{\Psi}^m \right]. \quad (5.28)$$

Equation (5.28) can be rearranged to obtain the current vector at the starting node as

$$\mathbf{I}_0^{n+1} = -\mathbf{I}_0^n - \mathbf{Y}_1 \mathbf{V}_0^n + \mathbf{Y}_2 \mathbf{V}_0^{n+1} - \Delta z (\boldsymbol{\xi}' + \boldsymbol{\chi}') \mathbf{V}_0^{n-1} + 2\mathbf{I}^{n+\frac{1}{2}} + \Delta z \boldsymbol{\Psi}^m. \quad (5.29)$$

Similarly, at the ending node

$$\mathbf{I}_{N_S}^{n+1} = -\mathbf{I}_{N_S}^n - \mathbf{Y}_1 \mathbf{V}_{N_S}^n + \mathbf{Y}_2 \mathbf{V}_{N_S}^{n+1} - \Delta z (\boldsymbol{\xi}' + \boldsymbol{\chi}') \mathbf{V}_{N_S}^{n-1} + 2\mathbf{I}^{n+\frac{1}{2}} + \Delta z \boldsymbol{\Psi}^m. \quad (5.30)$$

The updating procedure for current and voltage vectors is shown in Fig. 5.2.

## 5.3 Results and Discussion

First the validity of the MFDTD algorithm extended to accommodate frequency-dependent admittance is checked by comparing results those obtained from a thin-wire, full-wave using a thin-wire full-wave electromagnetic solver (Numerical Electromagnetic Code - NEC4) [91]. A buried bare conductor placed at a depth of 1 m and a 10 m high overhead conductor placed parallel to each other at a horizontal distance of 2 m are modelled. Radius of both conductors is taken as 20 mm. A derivative of a Gaussian pulse with a full-width at half maximum (FWHM) of 150 kHz as shown in Fig. 5.3 is used to excite the overhead conductor at the sending end. Both ends of the overhead conductor is grounded with 100  $\Omega$  resistors.

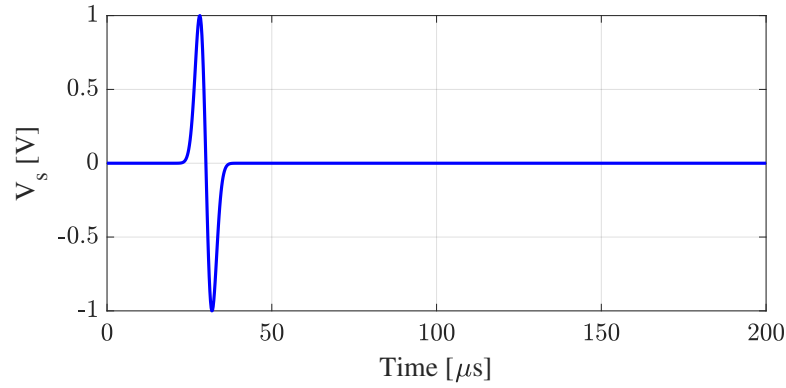
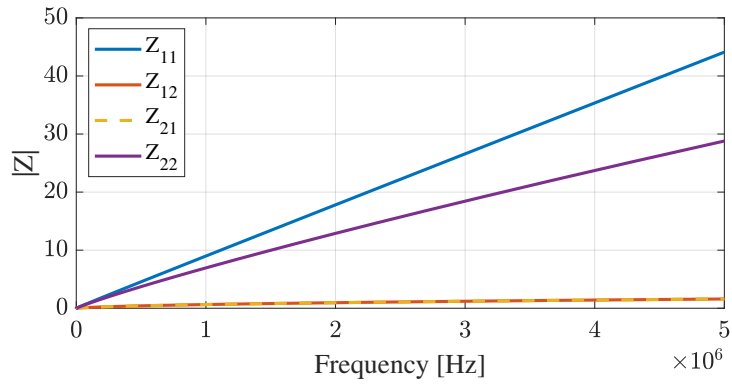


**Fig. 5.3:** Derivative of a Gaussian waveform applied on the overhead conductor.

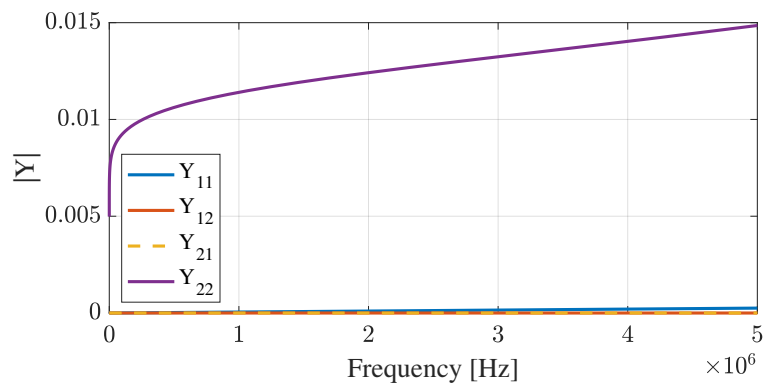
The finitely conducting ground is assumed to have a conductivity of 0.01 S/m and a relative permittivity of 15.

Elements of PUL impedance and admittance matrices are calculated using formulas derived by other researchers for uniform wire structures and are shown in Fig 5.4. The self impedance of the overhead line determined by Deri's closed-form approximation [44] for the well known Carson's formula [19]. Admittance is generally considered frequency independent for overhead lines and calculated as  $j\omega C$  where  $C$  is the DC capacitance. Impedance and admittance of the buried bare conductor are calculated using closed-form formulas given in [101]. Lucca's formulation is used to calculate the mutual impedance between the overhead wire and buried wire. Mutual admittance between overhead and buried conductors is generally assumed to be zero [102]. As seen by Fig. 5.4 both  $\mathbf{Z}$  and  $\mathbf{Y}$  are frequency dependent.

For the MFDTD algorithm, a time-step of  $0.2 \mu\text{s}$  is used. A space-step of 72 m is chosen in order to satisfy the stability criterion for FDTD simulations [27]. Sending end currents on the overhead wire and the ground wire are shown in Fig. 5.5 along with those obtained



(a)



(b)

**Fig. 5.4:** Elements of PUL (a) impedance and (b) admittance matrices of the wire structure.

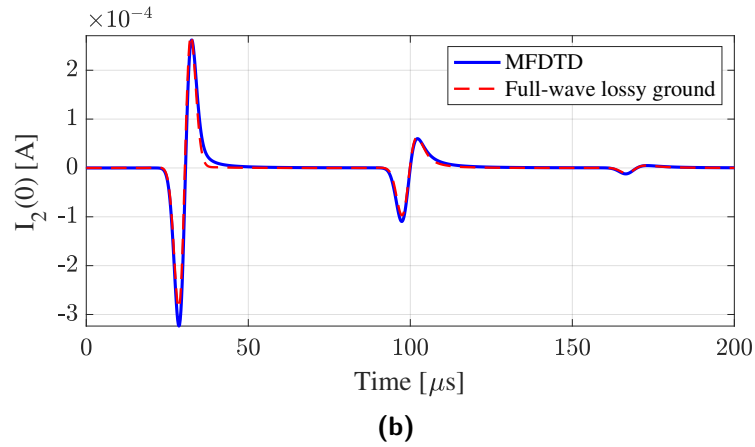
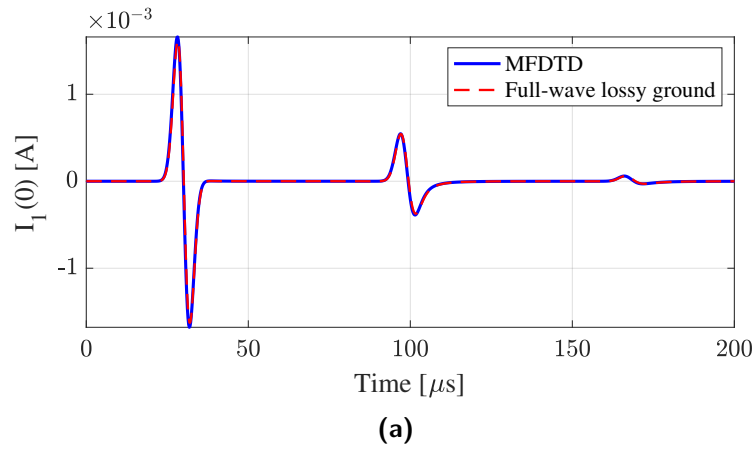


**Fig. 5.5:** Sending end currents of (a) the overhead conductor and (b) the buried conductor obtained using MFDTD method and a thin-wire full-wave solver.

using NEC. As evident from the current waveforms the transmission line approach along with the MFDTD algorithm is capable of modelling the wave propagation in both overhead and buried wires accurately.

Then, a wire structure where an overhead line crosses a buried conductor (similar to Fig. 5.1) is simulated with  $\ell = 1$  km,  $c = 0.4$  km,  $h = 10$  m, and  $a_i = 20$  mm. The buried conductor is assumed to be a bare pipeline since the frequency dependency of the

admittance of buried bare conductors is more significant than insulated conductors. The relative permittivity of the ground is taken as  $\epsilon_g = 10$ . Results under varying crossing angle ( $\alpha$ ), ground conductivity ( $\sigma_g$ ), pipeline radius ( $a_j$ ) and burial depth ( $d$ ) are compared with those obtained using Numerical Electromagnetic Code - (NEC4), a thin-wire full-wave electromagnetic solver [91]. The overhead line is terminated using  $100 \Omega$  resistor loads which are grounded using 1-m long vertical electrodes with 20 mm radius to be consistent with the full-wave simulator. For the values of ground conductivity and the electrode length used in this work, the impedance of the grounding electrodes is resistive. The value of the resistive grounding impedance is in the range of  $68 \Omega$  to  $6.8 \text{ k}\Omega$  when the ground conductivity varies from  $\sigma_g = 0.01$  to  $\sigma_g = 0.0001 \text{ S/m}$  [103]. The overhead line is excited using the same derivative of a Gaussian pulse used in the previous study and shown in Fig. 5.3.

In NEC4, to properly model the buried conductor and verify the accuracy of the thin-wire approximation employed in the proposed DSFTL model, the buried conductor is modelled as a cylinder made of 8 straight conductors each having a radius of 20 mm and short circuited using rings at every 100 m as shown in Fig. 5.6. The current in the buried conductor is calculated by adding the currents in all straight wires together.

The current in the overhead wire at the point of crossing, assuming  $\sigma_g = 0.001 \text{ S/m}$ ,  $d = 1 \text{ m}$ ,  $a_j = 25 \text{ cm}$  and a crossing angle ( $\alpha$ ) of  $30^\circ$ , is shown in Fig. 3.5, and the current in the buried wire at  $z = \frac{dz}{2}$ ,  $z = c$  and  $z = \ell - \frac{dz}{2}$  (where  $dz = 25 \text{ m}$  is the segment size used for the MFDTD algorithm and the NEC4 simulation), are shown in Fig. 3.6. Note that from a transmission line perspective, at  $z = 0$  and  $z = \ell$  the current on the buried wire is zero since the ends are open circuited. It is seen that the currents induced in the buried conductor by the overhead wire calculated by the proposed DSFTL model agree with those obtained using full-wave techniques. The peak current induced in the buried wire is close to

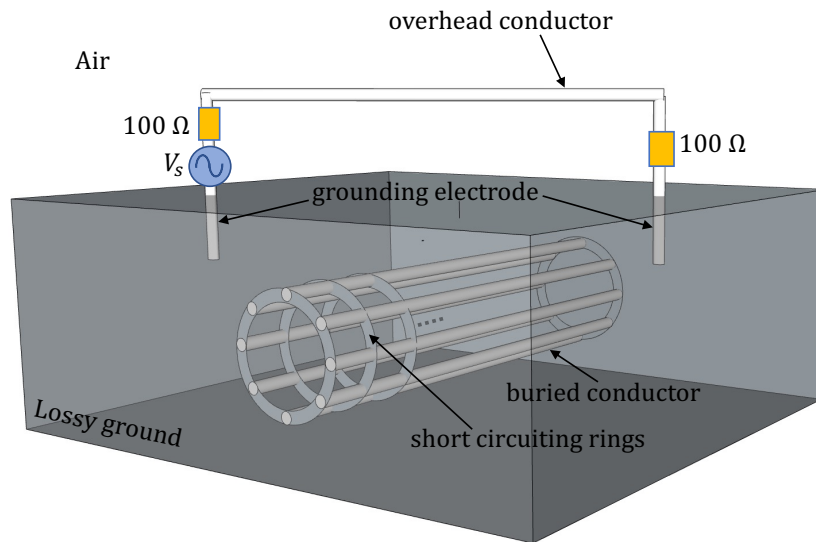


**Fig. 5.6:** A wire model of the geometry implemented in the fullwave solver (NEC4) used to validate the proposed DSFTL model. The buried conductor is modeled as 8 straight, parallel wires that allow simulating a conductor with an arbitrary diameter.

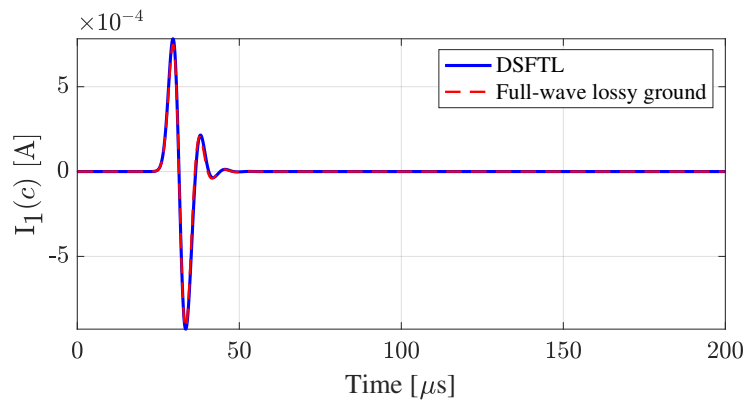


**Fig. 5.7:** Current at the point of crossing in the overhead wire.

1/3 of the current in the overhead wire. Another noticeable fact is that the current in the buried conductor toward its ends are negligibly small compared to that induced at the point of crossing. This is due to the fact the current dissipates quickly to the ground due to its finite conductivity. This case is referred to as the base case herein.

### 5.3.1 Effect of the crossing angle

The base case explained above is simulated with two other crossing angle ( $\alpha$ ) values,  $60^\circ$  and  $90^\circ$  and the current induced in the buried conductor at the point of crossing is shown in Fig. 5.9. The magnitude of the induced current in the buried wire decreases as the crossing angle increases. At a crossing angle of  $90^\circ$ , since  $Y_{ob}$  was assumed to be zero and  $Z_{ob} = 0$  when  $\alpha = 90^\circ$ , the DSFTL model will calculate a zero current in the buried wire. In reality there is a small current induced in the buried wire due to capacitive coupling (*i.e.* the existence of a small  $Y_{ob}$ ) as seen by the full-wave results in Fig. 3.6c. However, this current is seen to be negligibly small compared to the induced current at smaller angles. Therefore, it can be concluded that the assumption of  $Y_{ob} = 0$  is adequate for engineering purposes.

### 5.3.2 Effect of the ground conductivity

The base case is simulated with two other ground conductivity ( $\sigma_g$ ) values, 0.01 S/m and 0.0001 S/m based on the typical ground conductivity values given in [93]. The current induced in the buried conductor at the point of crossing is shown in Fig. 5.10. It is seen that results obtained using the proposed model and the full-wave solver agree for typical ground conductivity values. For larger ground conductivity values, the impedance of grounding electrodes will deviate from the purely resistive nature at lower frequencies [103]. Since, the effect of grounding electrodes are incorporated a resistor in the DSFTL model, there can be

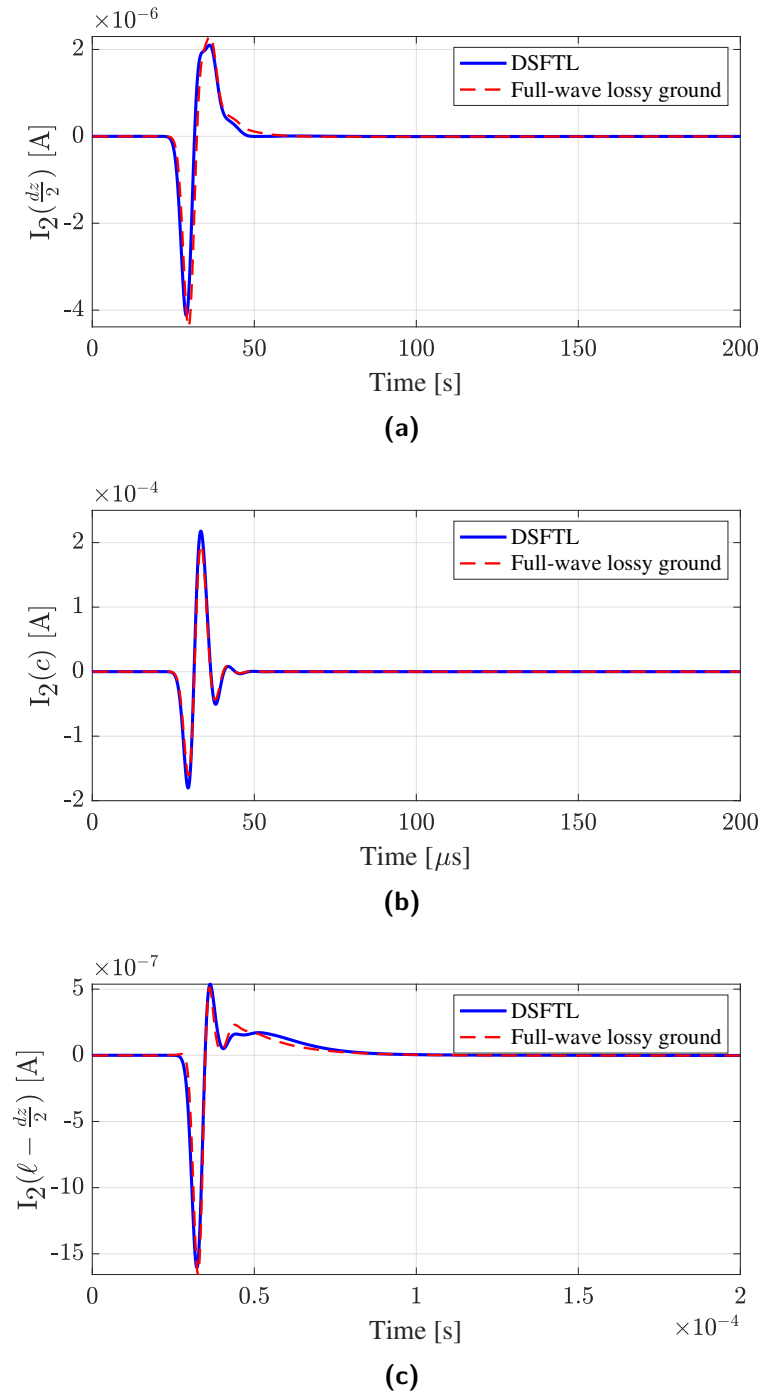


**Fig. 5.8:** Current at (a)  $z = \frac{dz}{2}$ , (b)  $z = c$  and (c)  $z = \ell - \frac{dz}{2}$  in the buried conductor.

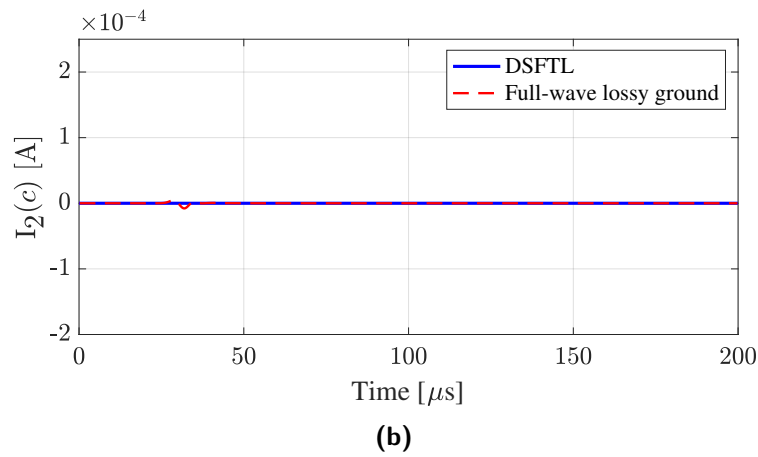
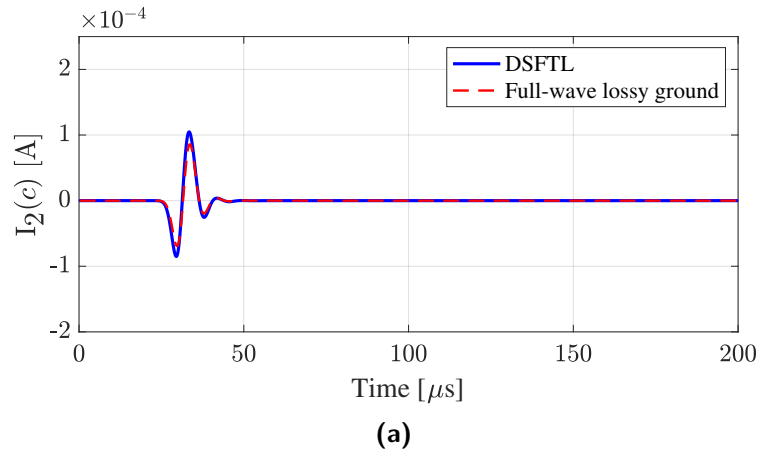


**Fig. 5.9:** Current at the point of crossing in the buried conductor for crossing angles of (a)  $60^\circ$ (b)  $90^\circ$ .

discrepancies with the full-wave results as seen in Fig. 5.10b. However, a high-frequency model of the grounding electrodes can be incorporated when implementing the DSFTL model in EMT simulators as explained in [100].

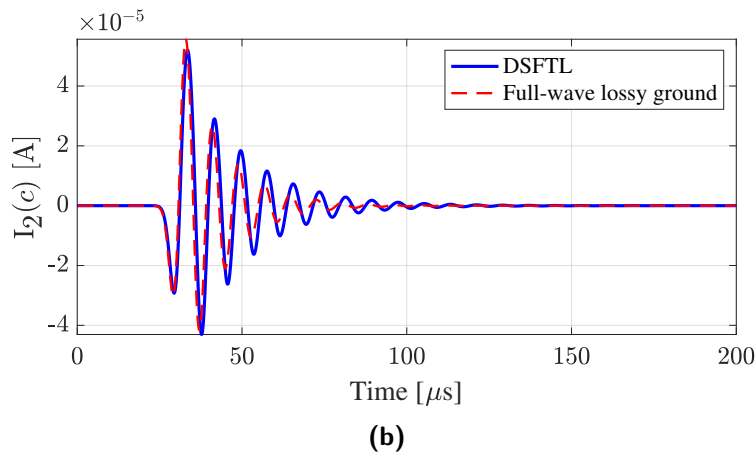
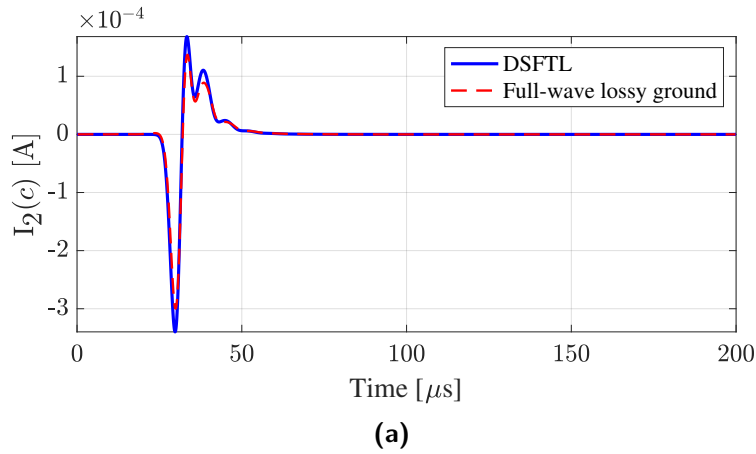


**Fig. 5.10:** Current at the point of crossing in the buried conductor for ground conductivity values of (a) 0.01 S/m and (b) 0.0001 S/m.

### 5.3.3 Effect of the radius of the buried conductor

The base case is simulated for buried conductor radii of 0.5 m and 0.99 m (in the latter, the buried conductor is close to the ground surface). Thin-wire approximation can be expected to hold for radii smaller than 0.25 m. The current induced in the buried conductor at the point of crossing is shown in Fig. 5.11. A slight increase is seen with increasing radii in both DSFTL and full-wave results which can be attributed to the fact that the gap between the

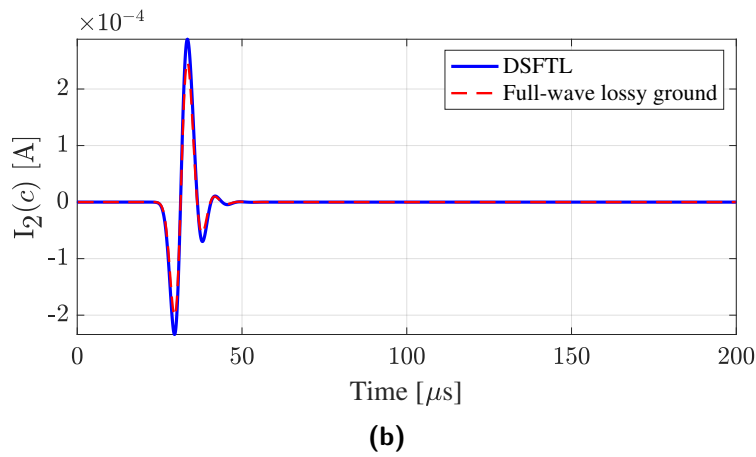
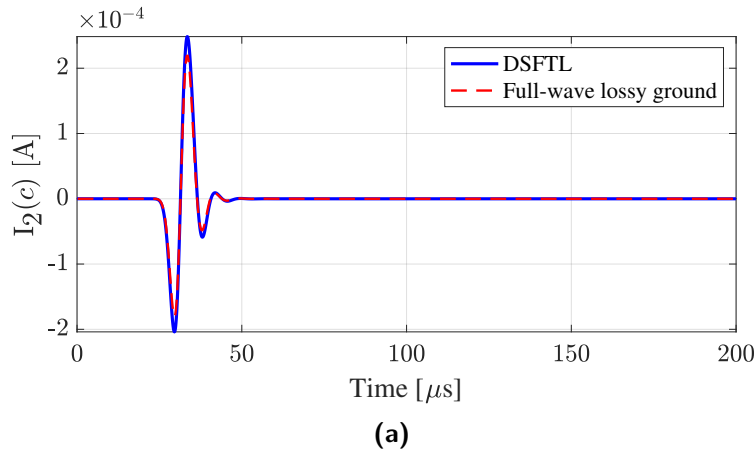


**Fig. 5.11:** Current at the point of crossing in the buried conductor for conductor radii of (a) 0.5 m and (b) 0.99 m.

overhead and buried conductors reduces when the buried conductor radius increases.

### 5.3.4 Effect of the burial depth

The base case is simulated with the underground conductor buried at depths ( $d$ ) of 5 m and 10 m. The current induced in the buried conductor at the point of crossing is shown in Fig. 5.12. A slight reduction in amplitude is seen in results obtained using both the DSFTL

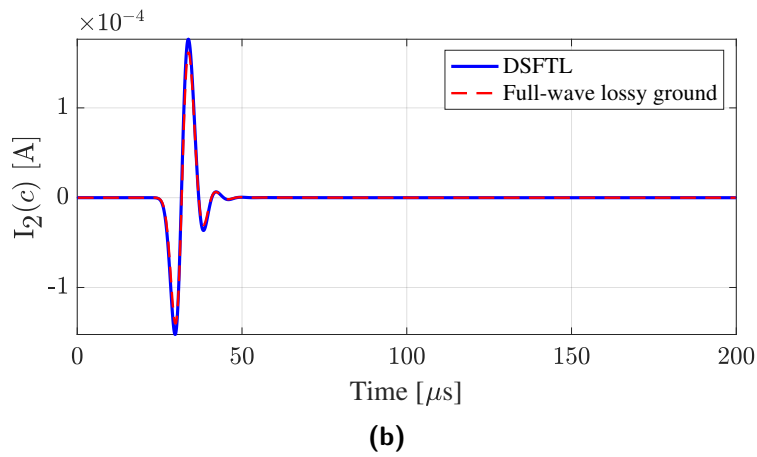
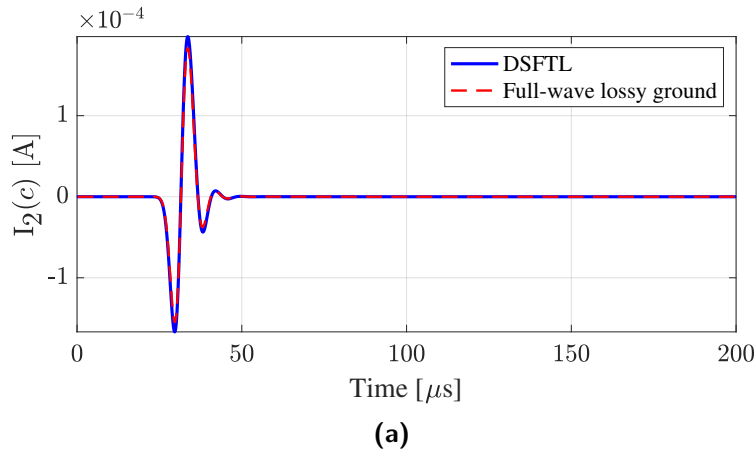


**Fig. 5.12:** Current at the point of crossing in the buried conductor for burial depths of (a) 5 m and (b) 10 m.

model and the full-wave solver when the burial depth increases.

### 5.3.5 Case study of lightning induced voltages

The base case is simulated with the ends of the overhead line matched to its characteristic impedance and  $z = 0$  excited with (a) a standard lightning impulse waveform of  $1.2/50 \mu\text{s}$  and (b) a standard lightning impulse of  $1.2/50 \mu\text{s}$  chopped after  $5 \mu\text{s}$  [104]. The voltage is

set to reach zero during chopping in  $0.5 \mu\text{s}$ . The magnitude of the excitation waveforms is chosen such that the voltage in the overhead line at the point of crossing has a peak magnitude of unity. Voltages obtained at the location of the crossing on the overhead and buried conductors are shown in Fig. 5.13. It is seen that the peak voltage on the buried conductor is around  $0.05\% \sim 0.3\%$  of the voltage on the overhead line. According to [105], a direct lightning strike to a 138 kV line above a ground with a conductivity of 0.001 S/m can cause a lightning voltage of around 500 kV. This means that the induced voltage peak in the buried conductor will be a few hundred volts. According to [96] voltages as low as 50 V are dangerous for humans.

## 5.4 Summary

This chapter proposed a nonuniform transmission line formulation to model a system of nonparallel overhead and buried conductors in the presence of finitely conducting ground. Closed-form expressions were derived for the PUL impedance and admittance matrices of a system of nonparallel overhead and buried wires. The MFDTD algorithm was modified further to accommodate a frequency dependent PUL admittance matrix. Results obtained using the proposed model were compared with those calculated using a commercial full-wave electromagnetic solver under varying crossing angle, ground conductivity, buried conductor radius and burial depth. Results produced by the proposed model agreed with full-wave results

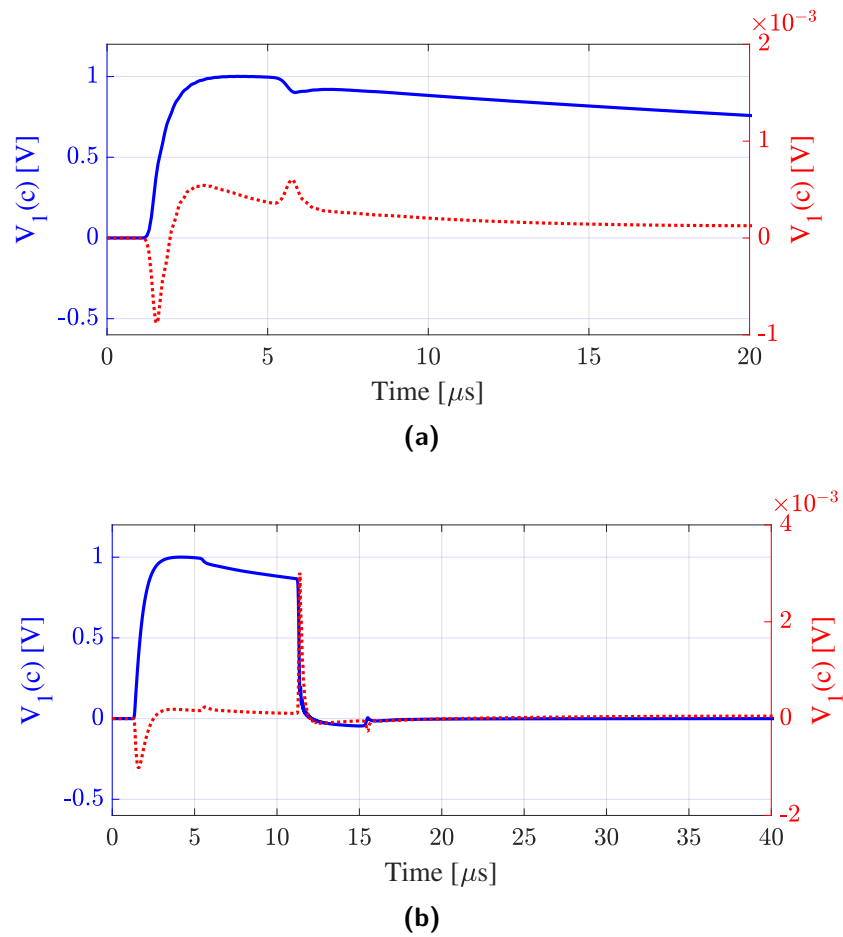


**Fig. 5.13:** Voltage at the crossing in the overhead line and buried conductor when the overhead line is excited with (a) a standard 1.2/50  $\mu$ s lightning impulse and (b) a standard 1.2/50  $\mu$ s lightning impulse chopped after 5  $\mu$ s with a chopping time of 0.5  $\mu$ s.

---

## Chapter 6

# Parallel Computing Methods for Finite-Difference Time-Domain

Parallel algorithms to increase the computational efficiency of the MFDTD method are proposed. As discussed in Section 2.5, since multi-core CPU and GPU architectures have their own advantages and disadvantages two parallel algorithms that utilize each of the architectures are proposed. Accuracy and performance of both algorithms are analyzed and discussed.

### 6.1 Parallel MFDTD Using multicore CPU

The basic concept of the proposed algorithm is to share the computations of the space-segments of the MFDTD model equally among the processor cores as shown in Fig. 6.1. When a serial algorithm is converted into parallel, additional commands needed for operations such as initialization of processors and data sharing gets added to the program. Processing time required for these additional commands is commonly referred to as the par-

allel overhead. These additional commands require additional processing time compared to serial programs. Work allocation to processors shown in Fig 6.1 is chosen such that the computational load is distributed equally among processors using a minimum parallel overhead. The leap-frog calculation of the MFDTD algorithm that was performed for one space-segment at a time is can now performed simultaneously at  $p$  segments where  $p$  is the number of processor cores available. Computations allocated to a particular core are executed serially. In Fig. 6.1 bold arrows represent information that has to be shared between processors. It is seen that at each time-step the last space segment of each processor except for processor  $p$  needs the voltage vector of the first space-segment of the adjacent processor from the previous time-step to compute its current vector. Similarly the first space segment of each processor except for processor 1 needs the newly calculated current vector of the last space-segment of the adjacent processor to compute its voltage vector.

This exchange of data can be conveniently performed using an “MPI\_SEND” (to send data) and an “MPI\_RECV” (to receive data) command among specified processor. Here the processor that is sending out data should call “MPI\_SEND” command specifying to which processor it is sending data. The receiving processor should call “MPI\_RECV” command specifying which processor it is expecting data from in order to complete the data exchange. A unique ID assigned to each data transfer assures that the data exchange happens only among the intended processors. Apart from the exchange of data this procedure keep the MFDTD algorithm synchronized making sure one processor would not perform a computation before other processors calculate the data needed for that particular calculation. It should be noted that for shared-memory architectures data sharing among processors is not needed. However, a synchronizing mechanism is still essential. Therefore, it is advisable to use the “MPI\_SEND” + “MPI\_RECV” mechanism even inside shared-memory architectures.

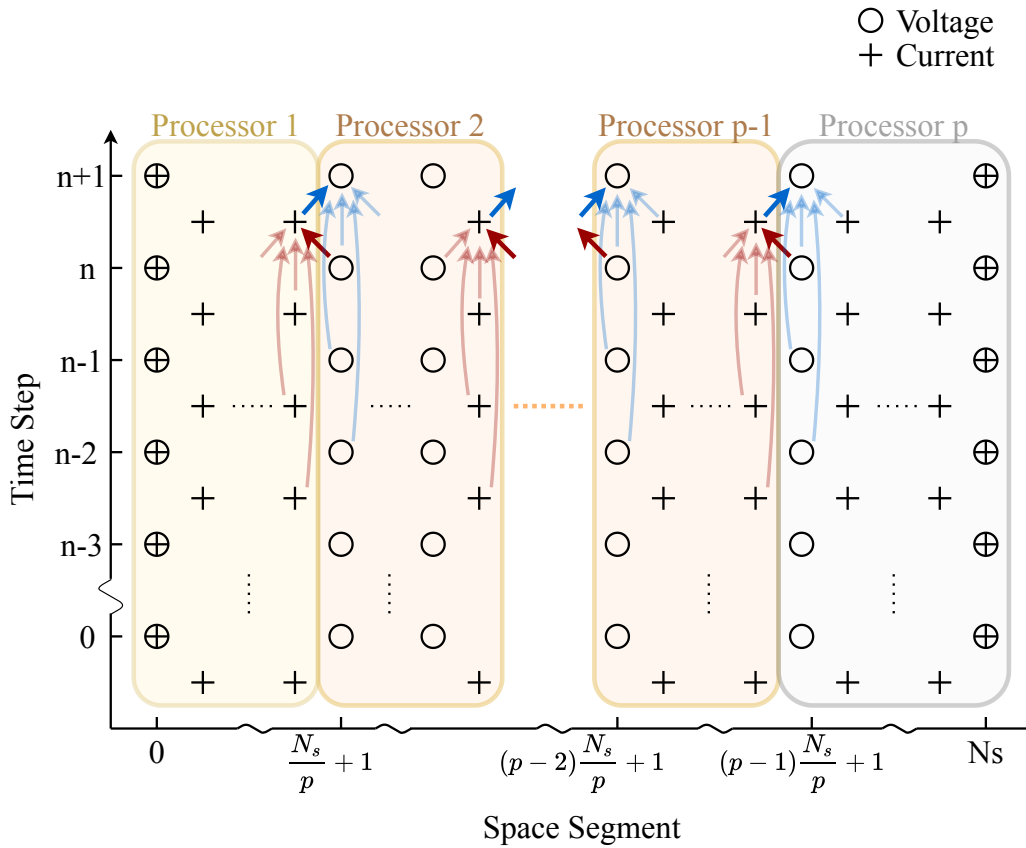


**Fig. 6.1:** Proposed parallel algorithm for MFDTD using multicore CPU architecture.

## 6.2 Parallel MFDTD Using GPU

A ‘host code’ running in the CPU performs the pre-calculations required and copies relevant data to the global memory of the GPU. The MFDTD algorithm is saved in the ‘device code’ which will be executed on the GPU on all GPU cores simultaneously when the kernel is called. The host code calls the GPU using a “device kernel” as shown in Fig. 6.2 in order to perform the MFDTD calculation. The device code is organized such that each space-segment of the MFDTD problem is allocated to a single core in the GPU. Therefore, unlike in the

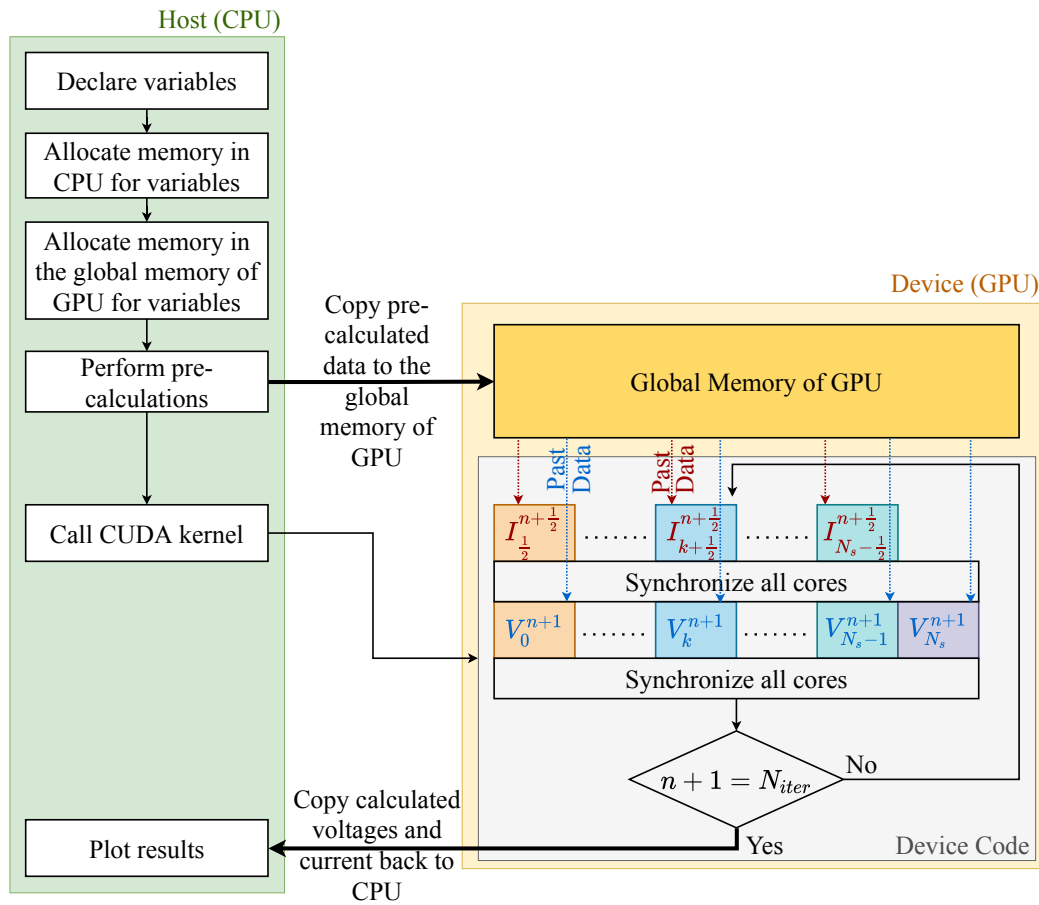


**Fig. 6.2:** Proposed parallel algorithm for MFDTD using GPU architecture.

CPU parallel algorithm explained in Section 6.1 all nodes will be calculated simultaneously enabling a massive speedup. Since all threads will be reading and writing from the global memory manual data transfer is not necessary. A synchronizing command is run after each current calculation and voltage calculation as shown in Fig. 6.2 forcing individual threads to wait until all threads finish the calculations related to the current time-step. This ensures that a thread would not advance to the next time-step until relevant past-data is available in the global memory.

## 6.3 Results and Discussion

A buried bare conductor and an overhead conductor parallel to each other are modelled. Cross-sectional dimensions of the structure (see Fig. 5.1) are  $h = 10$  m,  $d = 2$  m,  $b = 1$  m and  $a_1 = a_2 = 20$  mm. A derivative of a Gaussian pulse with a full-width at half maximum (FWHM) of 150 kHz is used to excite the overhead conductor at the sending end. Both ends of the overhead conductor is grounded with  $100 \Omega$  resistors. The finitely conducting ground is assumed to have a conductivity of 0.01 S/m and a relative permittivity of 15. Speed-up of the computational process achieved using the proposed parallel algorithms on CPU and GPU architectures are also discussed.

### 6.3.1 Performance of the parallel CPU algorithm

The mixed wire structure of overhead and buried wires is implemented using the parallel algorithm proposed for multicore CPU architecture in Section 6.1. The structure is discretized into 138 space segments. Fig. 6.3 shows the sending end currents of the overhead and buried wires obtained by distributing the work among different number of processors. It is seen that the parallel algorithm is able to produce the same result for each case. Execution time for vs the number of time-steps and the number of processors is shown in Table 6.1. Efficiency of parallel algorithms are generally calculated using ‘speed up factor’ ( $S(p)$ ) given by [90]

$$S(p) = \frac{\text{Time for serial execution}}{\text{Time for parallel execution}} \quad (6.1)$$

is shown in Fig. 6.4. It is clearly seen that the efficiency of the proposed algorithm increases and becomes closer to linear speedup when the number of time iterations increases. Behavior of the speed up factor agrees with Amdhal’s which states that if only a portion of a program

**Table 6.1:** Execution time of the MFDTD algorithm using different number of processors.

No. of time-steps	Execution time (s) for no. of processors (p)							
	1	2	3	4	5	6	7	8
1001	0.680	0.464	0.366	0.311	0.294	0.258	0.251	0.242
10001	6.231	3.406	2.324	1.837	1.586	1.436	1.276	1.213
100001	61.150	32.434	21.796	17.181	14.436	11.863	11.614	10.743

can be paralleled, when the level of parallelism of that portion increases the time taken for the execution of the serial portion will start to dominate the total execution time [90]. This explains why the curves tend to saturate when the number of processors increase. On the other hand, when the number of time-steps increases the parallelable portion of the program increases which allows for speed-up factors closer to linear speed-up. Changing the number of space-segments in the structure does not have an effect on the speed-up factor since the number of calculations in every section of the program will change proportionately. For example if the number of space-segments are doubled, the number of pre-calculations (which are performed serially) as well as the number of MFDTD calculations allocated to each processor (which are performed parallelly) will be doubled, causing both the serial and parallel portions of the program to consume twice the time as before.

### 6.3.2 Performance of the parallel GPU algorithm

The mixed wire structure of overhead and buried wires simulated is implemented using an NVIDIA GeForce GTX-1080 GPU which has approximately 2500 CUDA cores. Execution times compared to a serial programming approach is given in Table 6.2. Sending end currents

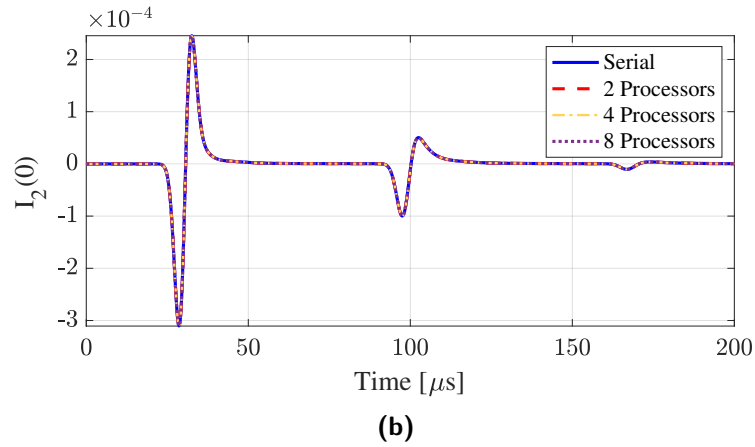
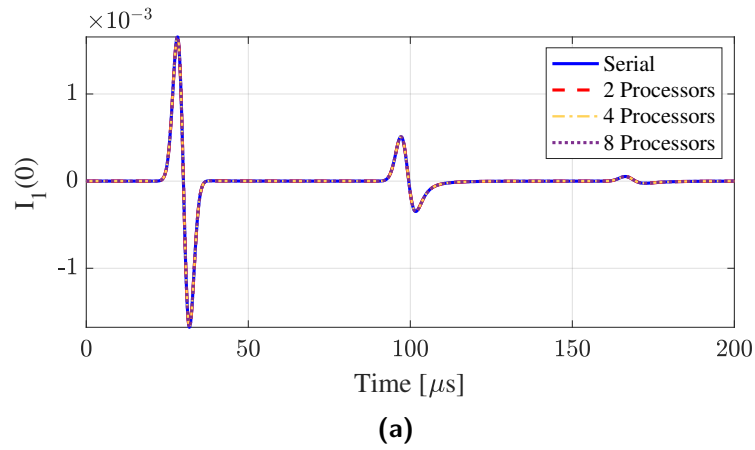


**Fig. 6.3:** Sending end currents of (a) the overhead conductor and (b) the buried conductor obtained by distributing the computations among different number of processors.

of the overhead conductor obtained using the proposed GPU based parallel algorithm with those obtained from a conventional serial program in Fig. 6.5 for two scenarios of space-steps and time-steps. Results indicate that the thread-synchronizing mechanism in the proposed parallel algorithm operates correctly. A notable fact from Table 6.2 is that for increasing number of space-segments the execution time of the GPU program has stayed constant. This happens because the number of space-segments is less than the available number of CUDA

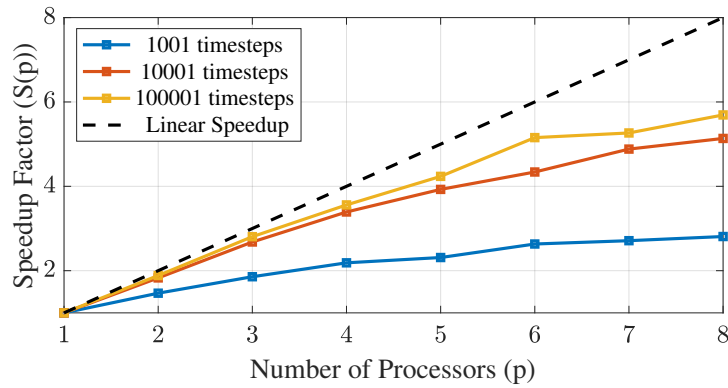
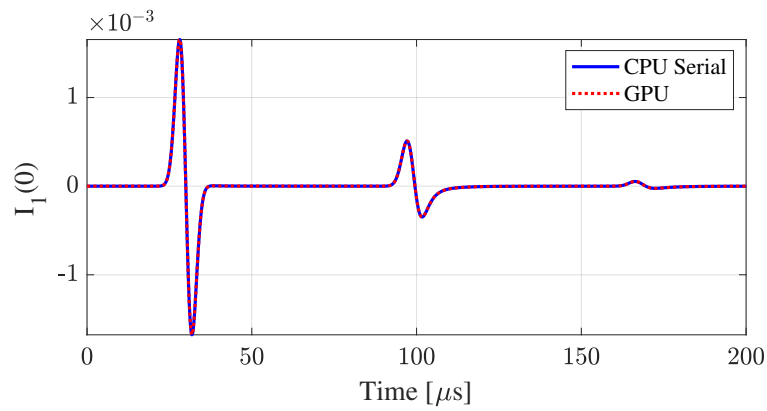


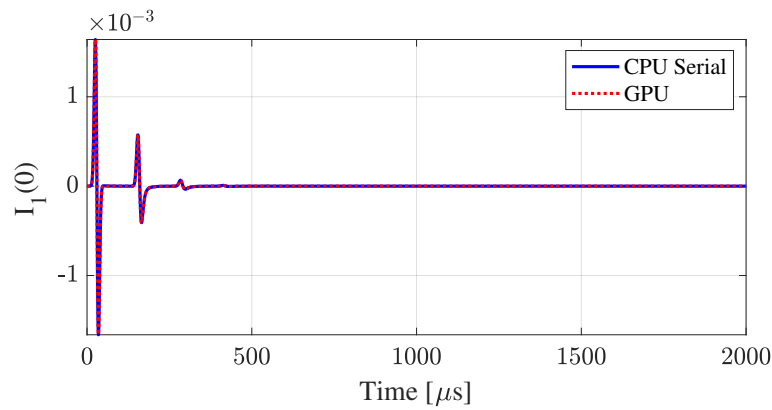
**Fig. 6.4:** Speed up factor obtained using algorithm Vs. the number of processors in CPU for varying number of time-steps.

cores. Therefore, each thread is guaranteed a dedicated core to itself. Also, the GPU parallel algorithm is seen to have lower execution times compared to the CPU parallel algorithm for the same number of space-segments.

Speed-up obtained under different number of space-segments and time-steps is shown in Fig. 6.6. It be seen that for a constant number of time-steps, the speed-up increases linearly with the number of space-segments. This is expected since the execution time of the serial program increases linearly with respect to the number of space-segments while the execution time in the GPU algorithm remains constant as discussed earlier. This is an advantage of the GPU parallel algorithm compared to the CPU parallel algorithm whose speed-up remained constant with varying space-segments as previously discussed in Section 6.3.1. The speed up of the GPU algorithm is expected to reach a peak and then drop due to the saturation of processing resources if the number of space-steps increased further. However, based on the typical number of space-segments in power line simulations, the speed up is expected to remain in the linear region shown in Fig. 6.6.



(a)



(b)

**Fig. 6.5:** Sending end currents of the overhead wire obtained using a serial program and the proposed parallel algorithm for simulations of (a) 138 space-steps and 1001 time-steps and (b) 255 space-steps and 10001 time-steps.

**Table 6.2:** Comparison of the execution time of the MFDTD algorithm using serial programming and GPU programming.

Time Steps	Number of space segments								
	138			255			1000		
	Serial (s)	GPU (s)	S(p)	Serial (s)	GPU (s)	S(p)	Serial (s)	GPU (s)	S(p)
1001	0.68	0.21	3.23	1.28	0.21	6.10	5.14	0.22	23.36
10001	6.23	0.81	7.69	11.41	0.82	13.91	45.15	0.81	55.74
100001	61.15	6.56	9.32	125.75	6.54	19.22	494.34	6.52	61.16

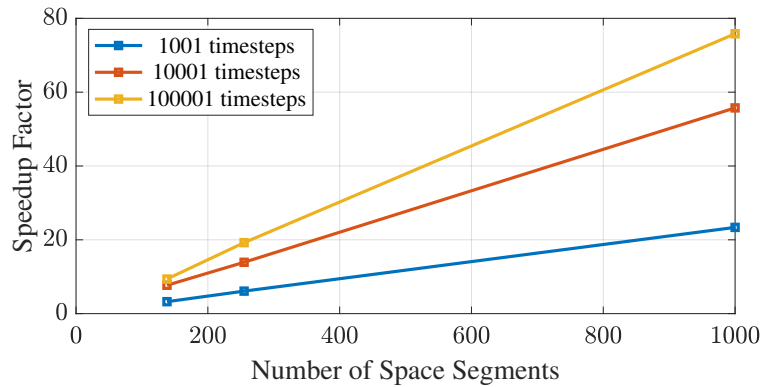


**Fig. 6.6:** Speed up factor obtained using the GPU algorithm Vs. the number of Space-segments for varying number of time-steps.

## 6.4 Summary

The disadvantage of FDTD based models are that they involve more calculations per time-step than terminal based models. This chapter proposed parallel computing techniques in order to increase the computational efficiency of the modified finite-difference time-domain (MFDTD) based multi-conductor transmission line models. Potential parallel computing algorithms were proposed for both conventional multi-core CPU and GPU architectures. Accuracy and performance of these algorithms were discussed. The proposed model is also expected to be a suitable candidate for modelling systems of overhead and buried transmission lines in massively parallel EMT simulation methods developed by other researchers.

---

# Chapter 7

## Conclusions and Future Work

### 7.1 Conclusions

With the expansion of power networks more transmission lines have to be constructed in a limited space often causing them to be placed in close proximity with each other or have discontinuities such as sharp bends along their span. Furthermore, lines with higher operating voltages are designed and constructed in-order to achieve higher power carrying capabilities. Induced interference from higher voltage lines to lower voltage lines, communication lines and buried pipelines during these close encounters has become a growing concern. Classical transmission line theory developed for uniform transmission lines is only applicable to parallel wires which typically is not fulfilled in such situations. Therefore, time-domain methods with the ability to solve non-uniform structures have to be developed.

This work proposed an approach, namely dispersive scattered field transmission line (DSFTL) model to simulate non-uniformities in dispersive transmission lines. A closed-form analytical formula was developed to determine the PUL parameter matrices of a system of

non-parallel wires above finitely-conducting ground. The resulting non-uniform transmission line equations consisting of space-dependent PUL parameters can be solved using a modified 1D-FDTD (MFDTD) algorithm. The proposed model was successfully implemented on a power system transient simulator. Results obtained for transient waveforms using the DSFTL model were compared with those from a full-wave electromagnetic solver. The comparison demonstrated that DSFTL can correctly model the transient behavior at such a non-uniformity. DSFTL was also able to regenerate power-frequency measurements of induced voltages obtained by other researchers at a real transmission line crossing. A case study on induced transients on power lines passing under faulty higher voltage lines was performed to demonstrate the capabilities of DSFTL model as a suitable candidate for a non-uniform transmission line model for power system EMT simulators.

External fields were coupled to the DSFTL model to simulate the effect of a nearby lightning strike. The developed model was used to analyze the effect of a nearby lightning strike on the transient behaviour of two crossing conductors in the presence of perfectly conducting and finitely conducting ground. Results obtained using the proposed model for conductors above PEC ground were compared to those obtained using full-wave simulations. In order to confirm the external field coupling in the presence of lossy ground is modelled accurately, the voltage induced on a uniform transmission line above lossy ground obtained using the proposed approach was compared to data available in the literature. A case study was also performed to investigate the transient behaviour of an overhead wire above lossy ground with and without the presence of a nearby nonparallel wire. Results indicated a nearby transmission line can intensify transients occurring on a overhead wire that cannot be calculated using the conventional uniform transmission line approaches.

Since buried pipelines coming into close proximity with overhead power transmission lines

and creating a nonparallel conductor structure is a common occurrence, the DSFTL model was extended to include buried conductors. Closed-form analytical expressions were derived for the PUL impedance and admittance matrices of a system of nonparallel overhead and buried conductors. The MFDTD algorithm was also modified further to include frequency-dependent admittance. Results obtained using the proposed model were compared with those calculated using a commercial full-wave electromagnetic solver under varying crossing angle, ground conductivity, buried conductor radius and burial depth. Results produced by the proposed model agreed with full-wave results.

Finite-difference time-domain (FDTD) based transmission line models require more computations per time-step compared to terminal based models that are used for uniform transmission lines. Therefore, to increase the computational efficiency of the modified FDTD (MFDTD) method which is used as the solving technique of the proposed DSFTL model, two parallel algorithms were proposed based on conventional multi-core CPU and GPU architectures. Accuracy and performance of these algorithms were discussed. It was seen that massive speedups compared to serial processing are possible by parallel implantation using GPUs. The proposed model is also expected to be a suitable candidate for modelling systems of overhead and buried transmission lines in GPU based massively parallel EMT simulation methods developed by other researchers.

## 7.2 Future Work

At its current state, the DSFTL model implemented in an EMT simulator operates considering an equal time step to that in the EMT simulation. This might in some cases cause the simulation to be less efficient with regards to execution time. Therefore the possibility to co-

simulate the DSFTL model and its corresponding EMT simulation with different time steps should be investigated. Also, nonlinear components such as lightning arresters are common in power networks and thus, in EMT simulations. Currently nonlinear components can be added to the EMT environment, outside the DSFTL model. The possibility of inclusion of nonlinear components inside the DSFTL model (*i.e.* within the nonuniform region of the transmission line) should be investigated.

In conventional models for overhead transmission lines, conductor are assumed to be horizontal and their height is assumed to be constant throughout the span of the line and equal to the tower height. However, in physical structures the conductors tend to sag due to their weight which results in a drop in height mid-span. Since the conductors are inclined to the ground rather than being horizontal, the currents flowing in them will also be inclined. Also, in mountainous areas the air-ground interface can be inclined. The approach proposed in this thesis is currently derived assuming horizontal conductors and a horizontal air-ground interface. Therefore, an extension of this formulation for inclined conductors and air-ground interface and validation using full-wave simulations is also suggested. An initial mathematical model can be written using thin-wire electromagnetic scattering equations. The possibility of arriving at a closed-form formula should be studied.

Transmission line models are used for the transient analysis of a wide range of structures from high-speed interconnects in electronic chips to power transmission lines. The methods proposed in this work for nonuniformities in power transmission lines are theoretically extendable for these structures as well. Especially, in electronic chips and printed circuits the types of nonuniformities addressed in this work (*i.e.* bends, nonparallel wires and crossings) are a common occurrence. However, before being applied to other structures a study on the applicable frequency ranges is suggested.

In circuit interconnects tunable components are added to the conventional structure in order to compensate for the dispersion of pulses. Tunable features are typically included by introducing nonlinearities such as periodic loading or distributed doping within the substrate to the transmission line geometry. Therefore, another suggested extension for this work is to incorporate such features into the formulation.

## References

- [1] A. J. Martinez-Velasco, *Power system transients : parameter determination*. Boca Raton: CRC Press/Taylor & Francis Group, 2010.
- [2] C. A. Nucci, F. Rachidi, M. V. Ianoz, and C. Mazzetti, "Lightning-induced voltages on overhead lines," *IEEE Transactions on Electromagnetic Compatibility*, vol. 35, no. 1, pp. 75–86, 1993.
- [3] M. Cervantes, I. Kocar, A. Montenegro, D. Goldsworthy, T. Tobin, J. Mahseredjian, R. Ramos, J. Marti, T. Noda, A. Ametani, and C. Martin, "Simulation of switching overvoltages and validation with field tests," *IEEE Transactions on Power Delivery*, vol. 33, no. 6, pp. 2884–2893, 2018.
- [4] T. J. Hammons, V. F. Lescale, K. Uecker, M. Haeusler, D. Retzmann, K. Staschus, and S. Lepy, "State of the art in ultrahigh-voltage transmission," *Proceedings of the IEEE*, vol. 100, no. 2, pp. 360–390, 2012.
- [5] D. Huang, Y. Shu, J. Ruan, and Y. Hu, "Ultra high voltage transmission in china: Developments, current status and future prospects," *Proceedings of the IEEE*, vol. 97, no. 3, pp. 555–583, 2009.
- [6] M. H. Shwehdi, M. A. Alaqil, and S. R. Mohamed, "Emf analysis for a 380kv transmission ohl in the vicinity of buried pipelines," *IEEE Access*, vol. 8, pp. 3710–3717, 2020.
- [7] C. Wang, X. Liang, and F. Freschi, "Investigation of factors affecting induced voltages on underground pipelines due to inductive coupling with nearby transmission lines," *IEEE Transactions on Industry Applications*, vol. 56, no. 2, pp. 1266–1274, 2020.
- [8] I. Cotton, K. Kopsidas, and Y. Zhang, "Comparison of transient and power frequency-induced voltages on a pipeline parallel to an overhead transmission line," *IEEE Transactions on Power Delivery*, vol. 22, no. 3, pp. 1706–1714, 2007.

- 
- [9] J. Tang, R. Zeng, H. Ma, J. He, J. Zhao, X. Li, and Q. Wang, "Analysis of electromagnetic interference on dc line from parallel ac line in close proximity," *IEEE Transactions on Power Delivery*, vol. 22, no. 4, pp. 2401–2408, Oct 2007.
- [10] J. Ma, R. D. Southey, and F. P. Dawalibi, "Measurement and computation of induced noise levels in telephone lines due to harmonics in nearby power lines," in *The 2006 4th Asia-Pacific Conference on Environmental Electromagnetics*, Aug 2006, pp. 577–581.
- [11] K. Kopsidas and I. Cotton, "Induced voltages on long aerial and buried pipelines due to transmission line transients," *IEEE Transactions on Power Delivery*, vol. 23, no. 3, pp. 1535–1543, 2008.
- [12] L. Yuze, K. Xiaofeng, and Z. Bo, "Calculation of induced voltage and current on a crossing transmission line under uhv ac transmission lines," in *2019 IEEE Asia Power and Energy Engineering Conference (APEEC)*, 2019, pp. 132–136.
- [13] F. Huo, W. Lu, Z. Qiu, D. Huang, and C. Huang, "Study on electric field distribution characteristics of the maintenance area when uhv ac transmission line crossing 220 kv tower," *The Journal of Engineering*, vol. 2019, no. 16, pp. 2986–2990, 2019.
- [14] M. H. Shwehdi, M. A. Alaqil, and S. R. Mohamed, "Emf analysis for a 380kv transmission ohl in the vicinity of buried pipelines," *IEEE Access*, vol. 8, pp. 3710–3717, 2020.
- [15] C. Wang, X. Liang, and R. Radons, "Minimum separation distance between transmission lines and underground pipelines for inductive interference mitigation," *IEEE Transactions on Power Delivery*, vol. 35, no. 3, pp. 1299–1309, 2020.
- [16] C. R. Paul, *Analysis of Multiconductor Transmission Lines, 2nd Edition*. Wiley-IEEE Press, 2007.
- [17] *EMTDC – Transient Analysis for PSCAD Power System Simulations: User’s Guide*. Manitoba HVDC Research Centre, 2005.
- [18] H. W. Dommel, *EMTP Theory Book*. Bonneville Power Administration, Protland, OR, 1986.
- [19] J. R. Carson, "Wave propagation in overhead wires with ground return," *Bell System Technical Journal*, vol. 5, no. 4, pp. 539–554, 1926.
- [20] T. Theodoulidis, "Exact solution of pollaczek’s integral for evaluation of earth-return impedance for underground conductors," *IEEE Transactions on Electromagnetic Compatibility*, vol. 54, no. 4, pp. 806–814, 2012.
-

- 
- [21] U. R. Patel, B. Gustavsen, and P. Triverio, "An equivalent surface current approach for the computation of the series impedance of power cables with inclusion of skin and proximity effects," *IEEE Transactions on Power Delivery*, vol. 28, no. 4, pp. 2474–2482, 2013.
- [22] U. R. Patel and P. Triverio, "Mom-so: A complete method for computing the impedance of cable systems including skin, proximity, and ground return effects," *IEEE Transactions on Power Delivery*, vol. 30, no. 5, pp. 2110–2118, 2015.
- [23] —, "Accurate impedance calculation for underground and submarine power cables using mom-so and a multilayer ground model," *IEEE Transactions on Power Delivery*, vol. 31, no. 3, pp. 1233–1241, 2016.
- [24] A. Ametani, "Electromagnetic transients program: History and future," *IEEE Transactions on Electrical and Electronic Engineering*, vol. 16, no. 9, pp. 1150–1158, 2021.
- [25] CIGRE, "Brochure 543: Guideline for numerical electromagnetic analysis method and its application to surge phenomena, wg c4.501," *CIGRE*, June, 2013.
- [26] T. Asada, A. Ametani, Y. Baba, and N. Nagaoka, "A study of transient responses on nonuniform conductors by fdtd simulations," *IEEE Transactions on Electrical and Electronic Engineering*, vol. 11, no. 4, pp. 435–441, 2016.
- [27] B. Kordi, J. LoVetri, and G. E. Bridges, "Finite-difference analysis of dispersive transmission lines within a circuit simulator," *IEEE Transactions on Power Delivery*, vol. 21, no. 1, pp. 234–242, Jan 2006.
- [28] N. Theethayi, R. Thottappillil, M. Paolone, C. A. Nucci, and F. Rachidi, "External impedance and admittance of buried horizontal wires for transient studies using transmission line analysis," *IEEE Transactions on Dielectrics and Electrical Insulation*, vol. 14, no. 3, pp. 751–761, 2007.
- [29] M. Gunawardana and B. Kordi, "Time-domain modeling of transmission line crossing using electromagnetic scattering theory," *IEEE Transactions on Power Delivery*, vol. 35, no. 2, pp. 1020–1027, 2020.
- [30] A. Morched, B. Gustavsen, and M. Tartibi, "A universal model for accurate calculation of electromagnetic transients on overhead lines and underground cables," *IEEE Transactions on Power Delivery*, vol. 14, no. 3, pp. 1032–1038, 1999.
- [31] N. Watson and J. Arrillaga, *Power Systems Electromagnetic Transients Simulation (2nd Edition)*. Institution of Engineering and Technology, 2019.

- 
- [32] B. Gustavsen and A. Semlyen, "Rational approximation of frequency domain responses by vector fitting," *IEEE Transactions on Power Delivery*, vol. 14, no. 3, pp. 1052–1061, 1999.
- [33] A. Ametani and M. Aoki, "Line parameters and transients of a non-parallel conductors systems," *IEEE Transactions on Power Delivery*, vol. 4, no. 2, pp. 1117–1126, April 1989.
- [34] S. Südekum and M. Leone, "Improved per-unit-length parameter definition for non-uniform and lossy multiconductor transmission lines," in *2018 International Symposium on Electromagnetic Compatibility (EMC EUROPE)*, Aug 2018, pp. 1–6.
- [35] K. Budnik and W. Machczyński, "Mutual impedance of non-parallel conductors with earth return," *European transactions on electrical power*, vol. 20, no. 3, pp. 354–366, 2010.
- [36] J. C. Maxwell, *A dynamical theory of the electromagnetic field*. The Royal Society, 1865.
- [37] F. de Paulis, M. Cracraft, C. Olivieri, S. Connor, A. Orlandi, and B. Archambeault, "Ebg-based common-mode stripline filters: Experimental investigation on interlayer crosstalk," *IEEE Transactions on Electromagnetic Compatibility*, vol. 57, no. 6, pp. 1416–1424, 2015.
- [38] H. A. Diawuo and Y. Jung, "Waveguide-to-stripline transition design in millimeter-wave band for 5g mobile communication," *IEEE Transactions on Antennas and Propagation*, vol. 66, no. 10, pp. 5586–5589, 2018.
- [39] "High-frequency electromagnetic coupling to transmission lines: electrodynamic correction to the tl approximation," in *Electromagnetic Field Interaction with Transmission Lines: From Classical Theory to HF Radiation Effects*, S. V. T. Farhad Rachidi, Ed. WITpress, 2008, p. 128.
- [40] S. Tkatchenko, F. Rachidi, and M. Ianoz, "Electromagnetic field coupling to a line of finite length: Theory and fast iterative solutions in frequency and time domains," *IEEE Transactions on Electromagnetic Compatibility*, vol. 37, no. 4, pp. 509–518, 1995.
- [41] S. Tkachenko, F. Rachidi, and J. Nitsch, "Analytical characterization of a line bend," *7th International Conference on Computational and Experimental Methods in Electrical Engineering and Electromagnetics*, vol. 39, no. 1, pp. 599–608, 2004.
- [42] Ashley Ng, M. Gunawardana, and B. Kordi, "Simulation of transmission line bend using a non-uniform transmission line model based on scattering theory," in *IEEE PES General Meeting*, 2020.
-

- 
- [43] L. Wedepohl and D. Wilcox, "Transient analysis of underground power-transmission systems. system-model and wave-propagation characteristics," *Proceedings of the Institution of Electrical Engineers*, vol. 120, no. 2, pp. 253–, 1973.
- [44] A. Deri, G. Tevan, A. Semlyen, and A. Castanheira, "The complex ground return plane a simplified model for homogeneous and multi-layer earth return," *IEEE Transactions on Power Apparatus and Systems*, vol. PAS-100, no. 8, pp. 3686–3693, 1981.
- [45] X. Shi, A. Ametani, A. Gole, and J. D. Silva, "Influence of finite-length overhead conductors on wave propagation characteristics and transients," in *2020 IEEE Power Energy Society General Meeting (PESGM)*, 2020, pp. 1–5.
- [46] A. Ametani and T. Kawamura, "A method of a lightning surge analysis recommended in japan using emtp," *IEEE Transactions on Power Delivery*, vol. 20, no. 2, pp. 867–875, April 2005.
- [47] A. Ametani and A. Ishihara, "Investigation of impedance and line parameters of a finite length multiconductor system," *Electrical Engineering in Japan*, vol. 114, no. 4, pp. 83–92, 1993.
- [48] V. Arnautovski-Toseva and L. Grcev, "On the image model of a buried horizontal wire," *IEEE Transactions on Electromagnetic Compatibility*, vol. 58, no. 1, pp. 278–286, 2016.
- [49] D. Poljak, K. El Khamlichi Drissi, K. Kerroum, and S. Sesnic, "Comparison of analytical and boundary element modeling of electromagnetic field coupling to overhead and buried wires," *Engineering Analysis with Boundary Elements*, vol. 35, no. 3, pp. 555–563, 2011.
- [50] D. Poljak, V. Doric, F. Rachidi, K. E. K. Drissi, K. Kerroum, S. V. Tkachenko, and S. Sesnic, "Generalized form of telegrapher's equations for the electromagnetic field coupling to buried wires of finite length," *IEEE Transactions on Electromagnetic Compatibility*, vol. 51, no. 2, pp. 331–337, 2009.
- [51] P. R. Bannister, "Applications of complex image theory," *Radio science*, vol. 21, no. 4, pp. 605–616, 1986.
- [52] X. Zhang, J. Luo, and Z. Zhao, "The iterative solution for electromagnetic field coupling to buried wires," *Mathematical problems in engineering*, vol. 2011, pp. 1–8, 2011.
- [53] F. A. Uribe, "Calculating mutual ground impedances between overhead and buried cables," *IEEE Transactions on Electromagnetic Compatibility*, vol. 50, no. 1, pp. 198–203, 2008.

- 
- [54] G. Lucca, "Mutual impedance between an overhead and a buried line with earth return," in *Ninth International Conference on Electromagnetic Compatibility, 1994. (Conf. Publ. No. 396)*, 1994, pp. 80–86.
- [55] A. Ametani, T. Yoneda, Y. Baba, and N. Nagaoka, "An investigation of earth-return impedance between overhead and underground conductors and its approximation," *IEEE Transactions on Electromagnetic Compatibility*, vol. 51, no. 3, pp. 860–867, 2009.
- [56] E. D. Sunde, *Earth conduction effects in transmission systems*. Dover Publications, 1968.
- [57] K. Budnik and W. Machczyński, "Mutual impedance of non-parallel conductors with earth return," *European transactions on electrical power*, vol. 20, no. 3, pp. 354–366, 2010.
- [58] I. Jurić-Grgić, R. Lucić, and A. Bernadić, "Transient analysis of coupled non-uniform transmission line using finite element method," *International Journal of Circuit Theory and Applications*, vol. 43, no. 9, pp. 1167–1174, 2015.
- [59] P. Manfredi, D. De Zutter, and D. V. Ginste, "Analysis of nonuniform transmission lines with an iterative and adaptive perturbation technique," *IEEE Transactions on Electromagnetic Compatibility*, vol. 58, no. 3, pp. 859–867, 2016.
- [60] Q. Liu, Y. Zhao, W. Yan, C. Huang, A. Mueed, and Z. Meng, "A novel crosstalk estimation method for twist non-uniformity in twisted-wire pairs," *IEEE Access*, vol. 8, pp. 38 318–38 326, 2020.
- [61] K. Afrooz and A. Abdipour, "Efficient method for time-domain analysis of lossy nonuniform multiconductor transmission line driven by a modulated signal using fdtd technique," *IEEE Transactions on Electromagnetic Compatibility*, vol. 54, no. 2, pp. 482–494, 2012.
- [62] J. Jeong and R. Nevels, "Time-domain analysis of a lossy nonuniform transmission line," *IEEE transactions on circuits and systems. II, Express briefs*, vol. 56, no. 2, pp. 157–161, 2009.
- [63] S. I. Abouzeid, G. Shabib, and A. Z. E. D. Mohamed, "Induced voltages on overhead transmission lines because of nearby included lightning channel," *IET Generation, Transmission & Distribution*, vol. 9, no. 13, pp. 1672–1680, 2015.
- [64] Y. Xie, C. Li, Y. Lv, and C. Yu, "Predicting lightning outages of transmission lines using generalized regression neural network," *Applied Soft Computing*, vol. 78, pp. 438–446, 2019.

- 
- [65] J. C. Salari, "A methodology for computing transmission-line short circuits caused by direct and nearby ground lightning incidence—part i: Methodological aspects," *IEEE Transactions on Power Delivery*, vol. 29, no. 4, pp. 1578–1585, 2014.
- [66] A. Soares, M. A. O. Schroeder, and S. Visacro, "Transient voltages in transmission lines caused by direct lightning strikes," *IEEE Transactions on Power Delivery*, vol. 20, no. 2, pp. 1447–1452, 2005.
- [67] T. H. Thang, Y. Baba, N. Nagaoka, A. Ametani, N. Itamoto, and V. A. Rakov, "FDTD simulation of direct lightning strike to a phase conductor: Influence of corona on transient voltages at the tower," *Electric Power Systems Research*, vol. 123, pp. 128–136, 2015.
- [68] F. Rachidi, "A review of field-to-transmission line coupling models with special emphasis to lightning-induced voltages on overhead lines," *IEEE Transactions on Electromagnetic Compatibility*, vol. 54, no. 4, pp. 898–911, 2012.
- [69] M. Rubinstein and M. A. Uman, "Transient electric and magnetic fields associated with establishing a finite electrostatic dipole, revisited," *IEEE Transactions on Electromagnetic Compatibility*, vol. 33, no. 4, pp. 312–320, 1991.
- [70] V. Cooray, "Some considerations on the "cooray-rubinstein" formulation used in deriving the horizontal electric field of lightning return strokes over finitely conducting ground," *IEEE Transactions on Electromagnetic Compatibility*, vol. 44, no. 4, pp. 560–566, 2002.
- [71] A. Mosaddeghi, A. Shoory, F. Rachidi, M. Rubinstein, G. Diendorfer, H. Pichler, and D. Pavanello, "Lightning return strokes to tall towers: Ability of engineering and electromagnetic models to reproduce nearby electromagnetic fields," *IEEE Transactions on Electromagnetic Compatibility*, vol. 54, no. 4, pp. 889–897, 2012.
- [72] V. Cooray, "Unification of engineering return stroke models," *Electric Power Systems Research*, vol. 195, p. 107118, 2021.
- [73] F. Heidler, J. M. Cvetic, and B. V. Stanic, "Calculation of lightning current parameters," *IEEE Transactions on Power Delivery*, vol. 14, no. 2, pp. 399–404, 1999.
- [74] D. Lovrić, S. Vujević, and T. Modrić, "On the estimation of heidler function parameters for reproduction of various standardized and recorded lightning current waveshapes," *International Transactions on Electrical Energy Systems*, vol. 23, no. 2, pp. 290–300, 2011.
-

- 
- [75] C. Taylor, R. Satterwhite, and C. Harrison, "The response of a terminated two-wire transmission line excited by a nonuniform electromagnetic field," *IEEE Transactions on Antennas and Propagation*, vol. 13, no. 6, pp. 987–989, November 1965.
- [76] K. Agarwal, D. Sylvester, and D. Blaauw, "Modeling and analysis of crosstalk noise in coupled rlc interconnects," *IEEE Transactions on Computer-Aided Design of Integrated Circuits and Systems*, vol. 25, no. 5, pp. 892–901, May 2006.
- [77] F. Rachidi, "Formulation of the field-to-transmission line coupling equations in terms of magnetic excitation field," *IEEE Transactions on Electromagnetic Compatibility*, vol. 35, no. 5, pp. 404–407, 1993.
- [78] M. Štumpf and G. Antonini, "Lightning-induced voltages on transmission lines over a lossy ground—an analytical coupling model based on the cooray–rubinstein formula," *IEEE Transactions on Electromagnetic Compatibility*, vol. 62, no. 1, pp. 155–162, 2020.
- [79] Y. Zhang, C. Liao, Y. Shang, X. Zhong, and W. Cao, "Fast evaluation of lightning-induced voltages on the transmission lines above a lossy ground," *IEEE Transactions on Electromagnetic Compatibility*, pp. 1–8, 2021.
- [80] A. De Conti and O. E. S. Leal, "Time-domain procedures for lightning-induced voltage calculation in electromagnetic transient simulators," *IEEE Transactions on Power Delivery*, vol. 36, no. 1, pp. 397–405, 2021.
- [81] M. Rubinstein, "An approximate formula for the calculation of the horizontal electric field from lightning at close, intermediate, and long range," *IEEE Transactions on Electromagnetic Compatibility*, vol. 38, no. 3, pp. 531–535, 1996.
- [82] V. W. Lee, C. Kim, J. Chhugani, M. Deisher, D. Kim, A. D. Nguyen, N. Satish, M. Smelyanskiy, S. Chennupati, P. Hammarlund, R. Singhal, and P. Dubey, "Debunking the 100x gpu vs. cpu myth: An evaluation of throughput computing on cpu and gpu," *SIGARCH Comput. Archit. News*, vol. 38, no. 3, p. 451–460, Jun. 2010.
- [83] J. Zhong and B. He, "Kernelet: High-throughput gpu kernel executions with dynamic slicing and scheduling," *IEEE Transactions on Parallel and Distributed Systems*, vol. 25, no. 6, pp. 1522–1532, 2014.
- [84] C.-T. Yang, C.-L. Huang, and C.-F. Lin, "Hybrid cuda, openmp, and mpi parallel programming on multicore gpu clusters," *Computer Physics Communications*, vol. 182, no. 1, pp. 266–269, 2011, computer Physics Communications Special Edition for Conference on Computational Physics Kaohsiung, Taiwan, Dec 15-19, 2009.

- 
- [85] M. Hafeez, S. Asghar, U. A. Malik, A. u. Rehman, and N. Riaz, "Survey of mpi implementations," in *Digital Information and Communication Technology and Its Applications*, H. Cherifi, J. M. Zain, and E. El-Qawasmeh, Eds. Berlin, Heidelberg: Springer Berlin Heidelberg, 2011, pp. 206–220.
- [86] J. Luo, Z. Ye, and C. Liao, "A mpi-based parallel fdtd-tl method for the emi analysis of transmission lines in cavity excited by ambient wave," *IEEE Transactions on Electromagnetic Compatibility*, vol. 62, no. 1, pp. 212–217, 2020.
- [87] P. Liu, J. Li, and V. Dinavahi, "Matrix-free nonlinear finite-element solver using transmission-line modeling on gpu," *IEEE Transactions on Magnetics*, vol. 55, no. 7, pp. 1–5, 2019.
- [88] S. Mohammadi, H. Karami, M. Azadifar, M. Rubinstein, and F. Rachidi, "Assessing the efficacy of a gpu-based mw-fdtd method for calculating lightning electromagnetic fields over large-scale terrains," *IEEE Letters on Electromagnetic Compatibility Practice and Applications*, vol. 2, no. 4, pp. 106–110, 2020.
- [89] Z. Zhou and V. Dinavahi, "Parallel massive-thread electromagnetic transient simulation on gpu," *IEEE Transactions on Power Delivery*, vol. 29, no. 3, pp. 1045–1053, 2014.
- [90] X.-H. Sun and Y. Chen, "Reevaluating amdahl's law in the multicore era," *Journal of Parallel and Distributed Computing*, vol. 70, no. 2, pp. 183–188, 2010.
- [91] G. Burke, A. Poggio, J. Logan, and J. Rockway, "NEC - numerical electromagnetics code for antennas and scattering," in *1979 Antennas and Propagation Society International Symposium*, vol. 17, June 1979, pp. 147–150.
- [92] J. Chan, *EPRI AC Transmission Line Reference Book — 200kV and Above, 2012 Edition*. EPRI, Palo Alto, CA, USA, 2012.
- [93] *World Atlas of Ground Conductivities*. Recommendation ITU-R 832-4, International Telecommunication Union, Geneva, Switzerland, July 2015.
- [94] *National Electrical Code (NEC), 2020 Ed.* NFPA 70, National Fire Protection Association, Quincy, Massachusetts, USA, June 2020.
- [95] S. Okabe, G. Ueta, T. Tsuboi, and J. Takami, "Study on switching impulse test waveform for uhv-class electric power equipment," *IEEE Transactions on Dielectrics and Electrical Insulation*, vol. 19, no. 3, pp. 793–802, 2012.
- [96] *IEEE Guide for Maintenance, Operation, and Safety of Industrial and Commercial Power Systems (Yellow Book)*. IEEE Std 902-1998, December 1998.
-

- 
- [97] S. Kalaga and P. Yenumula, *Design of Electrical Transmission Lines : Structures and Foundations*. CRC Press, 2016.
- [98] M. Brignone, D. Mestriner, R. Procopio, A. Piantini, and F. Rachidi, “On the stability of fdtd-based numerical codes to evaluate lightning-induced overvoltages in overhead transmission lines,” *IEEE Transactions on Electromagnetic Compatibility*, vol. 62, no. 1, pp. 108–115, 2020.
- [99] V. A. Rakov and M. A. Uman, “Review and evaluation of lightning return stroke models including some aspects of their application,” *IEEE Transactions on Electromagnetic Compatibility*, vol. 40, no. 4, pp. 403–426, 1998.
- [100] M. Gunawardana, A. Ng, and B. Kordi, “Time-domain coupling model for nonparallel frequency-dependent overhead multiconductor transmission lines above lossy ground,” *IEEE Transactions on Power Delivery*, pp. 1–1, 2021.
- [101] N. Theethayi, R. Thottappillil, M. Paolone, C. A. Nucci, and F. Rachidi, “External impedance and admittance of buried horizontal wires for transient studies using transmission line analysis,” *IEEE Transactions on Dielectrics and Electrical Insulation*, vol. 14, no. 3, pp. 751–761, 2007.
- [102] L. Qi, H. Yuan, L. Li, and X. Cui, “Calculation of interference voltage on the nearby underground metal pipeline due to the grounding fault on overhead transmission lines,” *IEEE Transactions on Electromagnetic Compatibility*, vol. 55, no. 5, pp. 965–974, 2013.
- [103] B. Salarieh, J. De Silva, and B. Kordi, “High frequency response of grounding electrodes: effect of soil dielectric constant,” *IET Generation, Transmission & Distribution*, vol. 14, no. 15, pp. 2915–2921, 2020.
- [104] E. Kuffel, *High voltage engineering fundamentals*, 2nd ed. Boston: Butterworth-Heinemann, 2000.
- [105] F. H. Silveira, A. De Conti, and S. Visacro, “Lightning overvoltage due to first strokes considering a realistic current representation,” *IEEE Transactions on Electromagnetic Compatibility*, vol. 52, no. 4, pp. 929–935, 2010.